REPORT DOCUMENTATION PAGE		Form Approved OMB NO. 0704-0188

1. REPORT DATE (DD-MM-YYYY) 31-12-2014	2. REPORT TYPE Final Report	3. DATES COVERED (From - To) 1-Oct-2011 - 30-Sep-2014

4. TITLE AND SUBTITLE Final Report: Topic 1.1.2, Unsteady Aerodynamics: Time-Varying Compressible Dynamic Stall Mechanisms Due to Freestream Mach Oscillations	5a. CONTRACT NUMBER W911NF-11-1-0503
	5b. GRANT NUMBER
	5c. PROGRAM ELEMENT NUMBER 611102

6. AUTHORS James W. Gregory	5d. PROJECT NUMBER
	5e. TASK NUMBER
	5f. WORK UNIT NUMBER

7. PERFORMING ORGANIZATION NAMES AND ADDRESSES Ohio State University 1960 Kenny Road Columbus, OH 43210 -1016	8. PERFORMING ORGANIZATION REPORT NUMBER

9. SPONSORING/MONITORING AGENCY NAME(S) AND ADDRESS (ES) U.S. Army Research Office P.O. Box 12211 Research Triangle Park, NC 27709-2211	10. SPONSOR/MONITOR'S ACRONYM(S) ARO
	11. SPONSOR/MONITOR'S REPORT NUMBER(S) 58835-EG-YIP.3

12. DISTRIBUTION AVAILIBILITY STATEMENT
Approved for Public Release; Distribution Unlimited

13. SUPPLEMENTARY NOTES
The views, opinions and/or findings contained in this report are those of the author(s) and should not contrued as an official Department of the Army position, policy or decision, unless so designated by other documentation.

14. ABSTRACT
The objective of this study is to investigate the effects of time-varying, compressible flow on rotorcraft dynamic stall. The problem was studied in an unsteady transonic wind tunnel and partitioned into three segments to facilitate understanding: pitch oscillations in a steady freestream, investigating unsteady effects (reduced frequency) and compressibility effects (Mach number); fixed pitch in a modulated freestream, studying various pre- and post-stall angles with fluctuating Mach number; and oscillations of both angle of attack and Mach number, studying the coupled effects and the importance of phasing between the two. The impact of compressibility on the traditional

15. SUBJECT TERMS
dynamic stall, pitch oscillations, freestream Mach oscillations, coupled pitch and Mach oscillations

16. SECURITY CLASSIFICATION OF:			17. LIMITATION OF ABSTRACT	15. NUMBER OF PAGES	19a. NAME OF RESPONSIBLE PERSON James Gregory
a. REPORT UU	b. ABSTRACT UU	c. THIS PAGE UU	UU		19b. TELEPHONE NUMBER 614-292-5024

Standard Form 298 (Rev 8/98)
Prescribed by ANSI Std. Z39.18

Report Title

Final Report: Topic 1.1.2, Unsteady Aerodynamics: Time-Varying Compressible Dynamic Stall Mechanisms Due to Freestream Mach Oscillations

ABSTRACT

The objective of this study is to investigate the effects of time-varying, compressible flow on rotorcraft dynamic stall. The problem was studied in an unsteady transonic wind tunnel and partitioned into three segments to facilitate understanding: pitch oscillations in a steady freestream, investigating unsteady effects (reduced frequency) and compressibility effects (Mach number); fixed pitch in a modulated freestream, studying various pre- and post-stall angles with fluctuating Mach number; and oscillations of both angle of attack and Mach number, studying the coupled effects and the importance of phasing between the two. The impact of compressibility on the traditional dynamic stall process was evaluated, with higher Mach numbers (and corresponding increased compressibility effects) changing the character of dynamic stall on the SSC-A09 from leading-edge to a trailing-edge phenomenon. Mach oscillations on a fixed-angle airfoil were found to have significant hysteresis at pre-stall angles, and substantial unsteadiness (periodic pressure fluctuations) in the post-stall regime. Coupled pitch and Mach oscillations showed that periods of flow acceleration have a stabilizing effect on the dynamic stall event.

Enter List of papers submitted or published that acknowledge ARO support from the start of the project to the date of this printing. List the papers, including journal references, in the following categories:

(a) Papers published in peer-reviewed journals (N/A for none)

Received   Paper

     TOTAL:

Number of Papers published in peer-reviewed journals:

(b) Papers published in non-peer-reviewed journals (N/A for none)

Received   Paper

     TOTAL:

Number of Papers published in non peer-reviewed journals:

(c) Presentations

Number of Presentations: 0.00

Non Peer-Reviewed Conference Proceeding publications (other than abstracts):

<u>Received</u>   <u>Paper</u>

12/31/2014 2.00 Kyle Hird, Matthew Frankhouser, James W. Gregory, Jeffrey P. Bons. Compressible Dynamic Stall of an
                       SSC-A09 Airfoil Subjected to Coupled Pitch and Freestream Mach Oscillations,
                       American Helicopter Society 70th Annual Forum. 19-MAY-14, . : ,

        TOTAL: **1**

Number of Non Peer-Reviewed Conference Proceeding publications (other than abstracts):

Peer-Reviewed Conference Proceeding publications (other than abstracts):

<u>Received</u>   <u>Paper</u>

08/31/2012 1.00 Jensen, Christopher D., Gregory, James W., Gompertz, Kyle A., Bons, Jeffrey P.. Compressible Dynamic
                       Stall Mechanisms Due to Airfoil Pitching and Freestream Mach Oscillations,
                       68th Forum, American Helicopter Society. 01-MAY-12, . : ,

        TOTAL: **1**

Number of Peer-Reviewed Conference Proceeding publications (other than abstracts):

(d) Manuscripts

<u>Received</u>   <u>Paper</u>

        TOTAL:

Number of Manuscripts:

Books

Received   Book

  TOTAL:

Received   Book Chapter

  TOTAL:

Patents Submitted

Patents Awarded

Awards

2014-15 Fulbright Award for the PI to collaborate with Prof. David Greenblatt at the Technion - Israel Institute of
Technology in Haifa, Israel on dynamic stall under time-varying freestream (the same subject as this grant).

Graduate Students

NAME	PERCENT_SUPPORTED	Discipline
Kyle Gompertz	1.00	
Kyle Hird	1.00	
FTE Equivalent:	**2.00**	
Total Number:	**2**	

Names of Post Doctorates

NAME	PERCENT_SUPPORTED
FTE Equivalent:	
Total Number:	

Names of Faculty Supported

NAME	PERCENT_SUPPORTED	National Academy Member
James W. Gregory	0.05	
FTE Equivalent:	**0.05**	
Total Number:	**1**	

Names of Under Graduate students supported

NAME	PERCENT_SUPPORTED
FTE Equivalent:	
Total Number:	

Student Metrics
This section only applies to graduating undergraduates supported by this agreement in this reporting period

The number of undergraduates funded by this agreement who graduated during this period: 0.00

The number of undergraduates funded by this agreement who graduated during this period with a degree in science, mathematics, engineering, or technology fields:...... 0.00

The number of undergraduates funded by your agreement who graduated during this period and will continue to pursue a graduate or Ph.D. degree in science, mathematics, engineering, or technology fields:...... 0.00

Number of graduating undergraduates who achieved a 3.5 GPA to 4.0 (4.0 max scale):...... 0.00

Number of graduating undergraduates funded by a DoD funded Center of Excellence grant for Education, Research and Engineering:...... 0.00

The number of undergraduates funded by your agreement who graduated during this period and intend to work for the Department of Defense 0.00

The number of undergraduates funded by your agreement who graduated during this period and will receive scholarships or fellowships for further studies in science, mathematics, engineering or technology fields:...... 0.00

Names of Personnel receiving masters degrees

NAME
Total Number:

Names of personnel receiving PHDs

NAME
Total Number:

Names of other research staff

NAME	PERCENT_SUPPORTED
FTE Equivalent:	
Total Number:	

Sub Contractors (DD882)

Inventions (DD882)

Scientific Progress

See Attachment

Technology Transfer

Final Report:
Topic 1.1.2, Unsteady Aerodynamics:
Time-Varying Compressible Dynamic Stall Mechanisms Due to Freestream Mach Oscillations

James W. Gregory
Associate Professor
Aerospace Research Center
Department of Mechanical and Aerospace Engineering
The Ohio State University

Abstract

The objective of this study is to investigate the effects of time-varying, compressible flow on rotorcraft dynamic stall. The problem was studied in an unsteady transonic wind tunnel and partitioned into three segments to facilitate understanding: pitch oscillations in a steady freestream, investigating unsteady effects (reduced frequency) and compressibility effects (Mach number); fixed pitch in a modulated freestream, studying various pre- and post-stall angles with fluctuating Mach number; and oscillations of both angle of attack and Mach number, studying the coupled effects and the importance of phasing between the two. The impact of compressibility on the traditional dynamic stall process was evaluated, with higher Mach numbers (and corresponding increased compressibility effects) changing the character of dynamic stall on the SSC-A09 from leading-edge to a trailing-edge phenomenon. Mach oscillations on a fixed-angle airfoil were found to have significant hysteresis at pre-stall angles, and substantial unsteadiness (periodic pressure fluctuations) in the post-stall regime. Coupled pitch and Mach oscillations showed that periods of flow acceleration have a stabilizing effect on the dynamic stall event.

Table of Contents

List of Figures

Nomenclature

A test section area

A^* throat area

c airfoil chord

C_L lift coefficient

C_{L_α} lift curve slope, $\partial C_L/\partial \alpha$

C_M moment coefficient

C_{M_α} moment curve slope, $\partial C_M/\partial \alpha$

C_p pressure coefficient

$C_{p,cr}$ critical pressure coefficient

f frequency, Hz

k reduced frequency, $\omega c/2U$

M Mach number

p pressure

r rotor radial location

R rotor radius

Re Reynolds number, Uc/ν

t time

T period

U velocity

x coordinate in the chordwise direction

x' choke vane coordinate

y coordinate perpendicular to the chord

y' choke vane coordinate

z coordinate in the spanwise direction

Greek

α angle of attack

α_{ss} static stall angle of attack

γ ratio of specific heats

φ phase angle

θ_{CV} angular position of the control vanes

ρ density

ω pitching frequency (1/sec)

ζ distance along the boundary layer edge

Subscripts

e edge of boundary layer

∞ freestream quantity

1. Introduction and Background

Dynamic stall (DS) is a performance-limiting phenomenon experienced by rotorcraft in forward flight, maneuver, and at high altitude. The dynamic stall event typically occurs on the retreating blade (third and fourth quadrants) when the rotor blade is rapidly pitched to high angle of attack. The lift stall and moment stall due to the shed vortex can produce significant variations in pitching moment. The transient, very high pitch link loads resulting from dynamic stall force design choices that add to the weight of the vehicle, and limit the operational envelope of the rotorcraft. Furthermore, certain dynamic stall phenomena induce significant vibratory loads that preclude operation under certain flight conditions. These physical phenomena place severe limitations on the maximum forward flight speed (advance ratio) of rotorcraft, which directly impacts Army rotorcraft operations. In many operational situations, it is very important to minimize the time required for a helicopter to transit to theater operations. The maximum forward flight speed, which is directly limited by compressible dynamic stall, must be increased in order to improve deployment response times. Thus, the dynamic stall phenomenon directly impacts Army aviation operations.

A full, detailed understanding of the aerodynamic phenomena inherent to compressible dynamic stall can enable control strategies or blade geometry optimization that may alleviate the very high pitch link loads and expand the operating envelope. Dynamic stall is a well-studied problem; however, most of the historical investigations have not accounted for the effects of compressibility. In particular, there is a lack of knowledge about the effects of *unsteady* compressibility effects on dynamic stall that is typical of rotorcraft operations in maneuver or high-speed forward flight. In order to develop a full, accurate understanding of this dynamic stall phenomenon, the problem must be investigated with advanced instrumentation in conditions that adequately model time-varying compressibility effects. The purpose of this investigation is to experimentally model the full-unsteady compressible flow situation and perform a detailed study of the complex compressibility effects on boundary layer character and DS vortex development at matched reduced frequency, Mach number, and Reynolds number.

Relevant studies of dynamic stall stretch over four decades, such that the basic phenomena of dynamic stall under incompressible, static freestream conditions are thoroughly documented (McCroskey *et al*., 1976; Lorber and Carta, 1987; Lorber, Carta, and Covino, 1992; Carr, 1988). Contemporary investigations of the intricate details of dynamic stall are also currently underway

(Geissler *et al*., 2005; Sahoo *et al*., 2008; Martin *et al*., 2008; DiOttavio *et al*., 2008). Despite the extensive, rich literature base in the field, rarely are Mach and Reynolds number varied independently to study their influence on DS, and compressibility effects are not well understood (Carr and Chandrasekhara, 1996). Due to large amplitude pitching motions, compressibility effects can be important for onset Mach numbers as low as 0.2. At higher Mach numbers, shocks can produce premature laminar separation during the pitch-up motion – thus interrupting the vortex shedding that is characteristic of deep dynamic stall (Ericsson and Reding, 1984). The state of the boundary layer and its susceptibility to separation are in turn functions of Reynolds number. Thus, the two flow parameters are strongly coupled. Typical onset Mach and Reynolds number ranges are 0.2-0.5 and 2-6 million, respectively, for retreating blade stall. Mach numbers for advancing blade stall can exceed 0.8 (with correspondingly higher *Re* values), as noted by Bousman (1998).

In order to study the effects of compressibility on dynamic stall, Carr and Chandrasekhara (1992) developed the Compressible Dynamic Stall Facility at NASA Ames Research Center. Their facility featured excellent optical access, freestream Mach numbers up to 0.5, and airfoil oscillation frequencies up to 100 Hz, allowing reduced frequencies up to 0.15 to be tested in compressible flows. Their studies have included determinations of the DS vortex convective speed in compressible flows (Chandrasekhara and Carr, 1990), development of a point diffraction interferometry system for quantitative visualization of DS vortex behavior (Carr *et al*., 1994), a detailed investigation of the mechanisms that drive compressible dynamic stall (Chandrasekhara *et al*., 1998), multi-element airfoils for DS alleviation (Carr *et al*., 2001), and heat-flux gauge investigations that captured the shock imprint near the leading edge (Chandrasekhara and Wilder, 2003). One outcome of the seminal investigations into compressibility effects on dynamic stall is the development of the dynamic drooping leading edge (Chandrasekhara *et al*., 2001; Martin *et al*., 2003; Chandrasekhara *et al*., 2004; and Chandrasekhara, 2007).

Dynamic stall induces large amplitude mechanical oscillations of the rotor accompanied by large pitch-link loads, due to the strong negative moment induced when the stall vortex travels along the blade chord from leading to trailing edge. For the retreating blade dynamic stall, the reduced frequency of the first harmonic (1/rev) blade oscillation ($k = 0.5\,\omega c/U$) ranges from 0.05 to 0.2. The majority of helicopter rotor dynamic stall studies reported in the literature have been

conducted in a constant velocity wind tunnel with either a 2D airfoil pitching (or plunging) at the appropriate reduced frequency. In reality, since the rotor stall occurs during the retreating blade motion (at advance ratios that can approach 0.3 to 0.4), the component of the vehicle advance velocity "seen" by the retreating airfoil also varies during the dynamic stall event. Thus, in a rotor-relative frame, both the approach flow angle (due to pitch/plunge) *and* magnitude are time-varying. This time-varying relative velocity has a direct influence on the severity of the local pressure gradient as shown by Ericsson (1985). Ericsson applied the Navier-Stokes equation at the boundary layer edge to obtain an expression for the streamwise pressure gradient, $\partial p_e/\partial \zeta$:

$$-\frac{1}{\rho_e}\frac{\partial p_e}{\partial \zeta} = \frac{\partial U_e}{\partial t} + U_e \frac{\partial U_e}{\partial \zeta} \qquad (1)$$

From this is it clear that the streamwise pressure gradient that is imposed on the boundary layer is a function of both spatial *and* temporal gradients in velocity. Namely, the adversity of the pressure gradient, $\partial p_e/\partial \zeta$, will be decreased by an accelerating external velocity, $\partial U_e/\partial t > 0$. Since the pressure gradient is a critical parameter influencing boundary layer separation, $\partial U_e/\partial t$ will tend to either promote or suppress separation. This led Ericsson to conclude that, "The free-flight/wind tunnel equivalence derived for unsteady inviscid flow in general, cannot be applied to dynamic stall analysis because of the unsteady viscous boundary condition at the airfoil surface, the so-called moving wall effect." (Ericsson, 1985). Thus, it is evident that *time-varying freestream velocity will have a direct impact* on the adversity of the instantaneous pressure gradient, and thus, the formation of the dynamic stall process.

Several researchers have investigated the combination of airfoil pitching and relative velocity oscillations (Pierce *et al.*, 1978; Favier *et al.*, 1988) and concluded that a strong coupling exists between the two modes of oscillation. Of note, all research of this type has been conducted at incompressible flow speeds below Mach 0.1. In contrast, the effort presented here studies the effects of unsteady Mach oscillations on the dynamic stall process, where the unsteady compressibility effects are largely unknown.

Fernie and Babinsky (2003, 2004) conducted a very interesting investigation into the effects of unsteady freestream oscillations on the dynamic shock structure on a NACA 0012 airfoil. When operated at transonic speeds and moderately high frequencies (of the order of 50 Hz), they found that there were differences in the shock strength and speed, depending on whether the freestream Mach number was increasing or decreasing. They found that a *decelerating*

freestream caused a stronger shock to move forward on the airfoil surface more rapidly than an accelerating freestream over the same change in Mach number. Fernie and Babinsky's work shows that compressibility effects should be significant, yet they stopped short of performing any dynamic stall investigations (their work was limited to a fixed airfoil).

The work presented here is unique in that it properly models the effects of time-varying Mach number on dynamic stall phenomena at suitable reduced frequencies and advance ratios typical of high-speed forward flight of rotorcraft. The objectives of this experimental research include establishing the significance of and understanding the impact of time-varying compressibility on compressible dynamic stall. There are three unsteady scenarios which are simulated experimentally. The first scenario is that of the oscillating airfoil in a steady airstream. The dynamic stall encountered in this scenario constitutes the conventional simulation of the dynamic stall process that has contributed to our understanding of the key physical phenomena. The second scenario involves evaluation of how hysteresis and stall are impacted when a fixed-pitch airfoil is subjected to a time-varying freestream Mach number condition. Finally, the airfoil model oscillations are synchronized with the freestream velocity oscillations for coupled pitch and Mach oscillations. Moreover, measurements are made while varying the phasing relationship between these synchronized oscillations. Through this progression, the impact of time-varying compressibility on the compressible dynamic stall process is elucidated.

2. Experimental Configuration

2.1 Transonic Wind Tunnel

The dynamic stall problem was investigated in the 6" × 22" transonic wind tunnel located in the Aeronautical and Astronautical Research Laboratories (AARL) at The Ohio State University. The facility has been used over the last three decades by every major aircraft manufacturer for airfoil studies (Lee et al., 1978). The tunnel has also been used for dynamic stall investigations on airfoil sections such as the NACA 0015 (Gregorek et al., 1989). A layout of the tunnel can be seen in Figure 1. Inlet flow to this open-circuit wind tunnel is delivered by 20cm (8in.) supply line from two 42.5m^3 (1500 ft^3) air storage tanks pressurized up to 17MPa (2500 psi) with in-line air dryers to maintain gas purity. The high pressure air flow is controlled by two valves. The first is a control valve which sets the total pressure and Reynolds number. The second valve is a fast acting valve used to start and stop the flow. Valving and various multifunction data acquisition

tasks are orchestrated using the 6" × 22" control computer. The maximum operating pressure of the wind tunnel is 350kPa (50psia). The settling chamber is equipped with a perforated plate, honeycomb section and then eight screens (60-mesh) to condition the flow and lower the test-section turbulence intensity to < 0.5% of the freestream velocity under steady flow conditions. A subsonic nozzle with a contraction ratio of 15:1 provides excellent flow uniformity in the 6" × 22" test section which is 1.1m long. The 56cm (22in.) high, solid sidewalls hold the airfoil. The 15cm (6in.) spanwise floor and ceiling walls are perforated with 3.2mm straight holes yielding an effective porosity of 6 percent (Petrie and Davis, 1978). These isolation cavities or plenums are open to the flow only downstream of the test section and aid in producing a high quality flow in the test section by reducing Mach wave reflections in transonic flow.
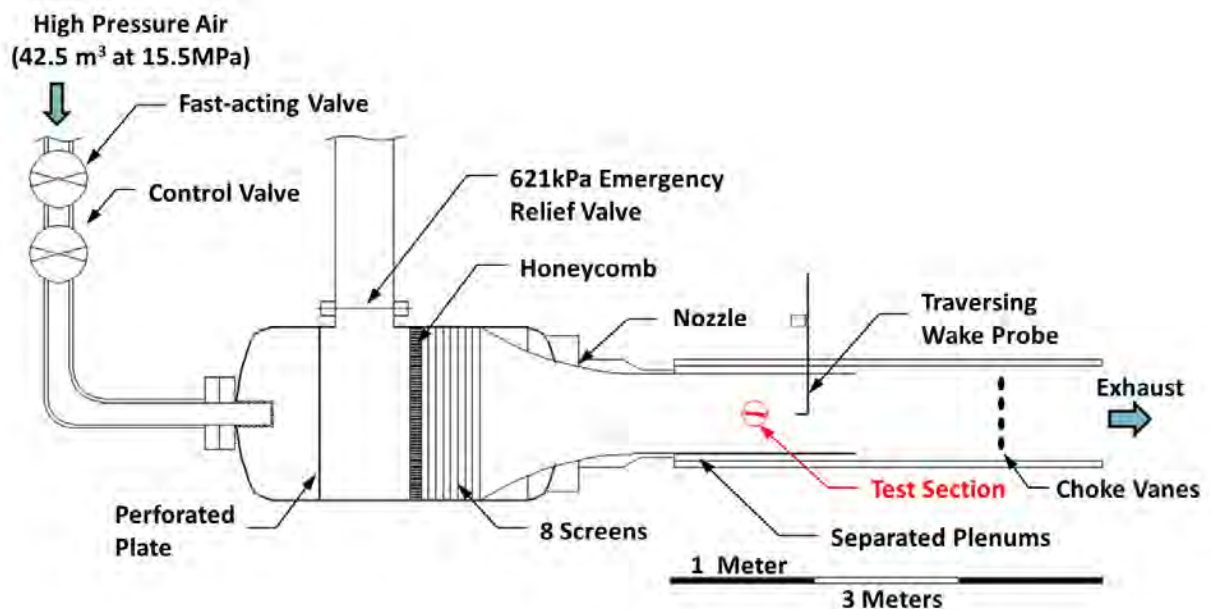
Figure 1: Schematic of the Aeronautical & Astronautical Research Lab 6" × 22" transonic wind tunnel.

Mach number is controlled independently of Reynolds number by adjusting the throat area downstream of the test section. The Mach number is uniquely set by the throat area, independent of stagnation pressure, as long as choked flow is maintained. The two parameters (*Re* and *M*) can be independently varied over a considerable range, as shown in Figure 2.
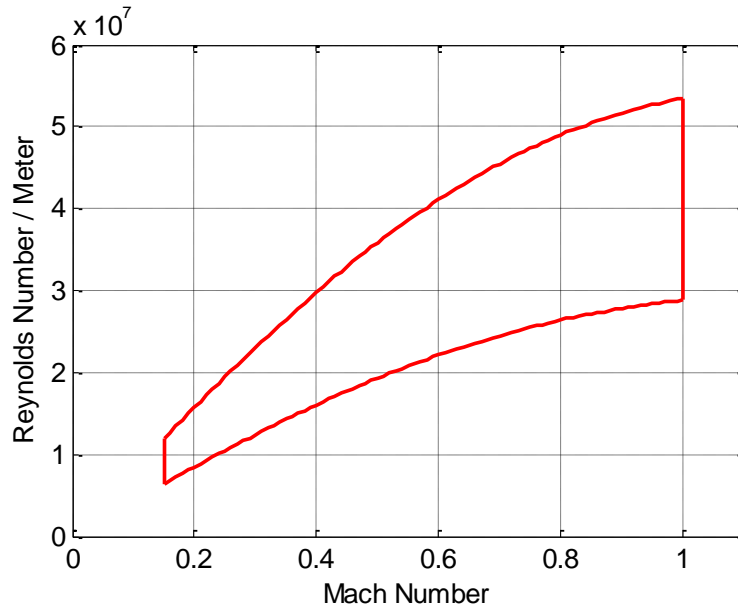
Figure 2: Range of operating conditions for the 6" × 22" transonic wind tunnel at 287K (56°F) and a max operating pressure of 345kPa (50psia).

The 6" × 22" is equipped to operate in several dynamic modes in order to simulate compressible dynamic stall. Its accessories include an airfoil oscillation mechanism which is based on a 5-hp motor that drives a face cam and mechanical link assembly, as shown in Figure 3 through Figure 5. In its current configuration, the oscillation mechanism has been reliably operated at frequencies up to 17 Hz over a wide range of oscillation amplitudes. Also, the 6" × 22" transonic wind tunnel facility was recently modified by the installation of rotating vanes at the throat, to allow for variable choke area and Mach oscillations at rates up to 17 Hz in the test section (Gompertz *et al.*, 2011). An overview of the airfoil pitch oscillation and Mach oscillation devices is presented in Figure 3 and they are discussed in more detail in subsequent sections.
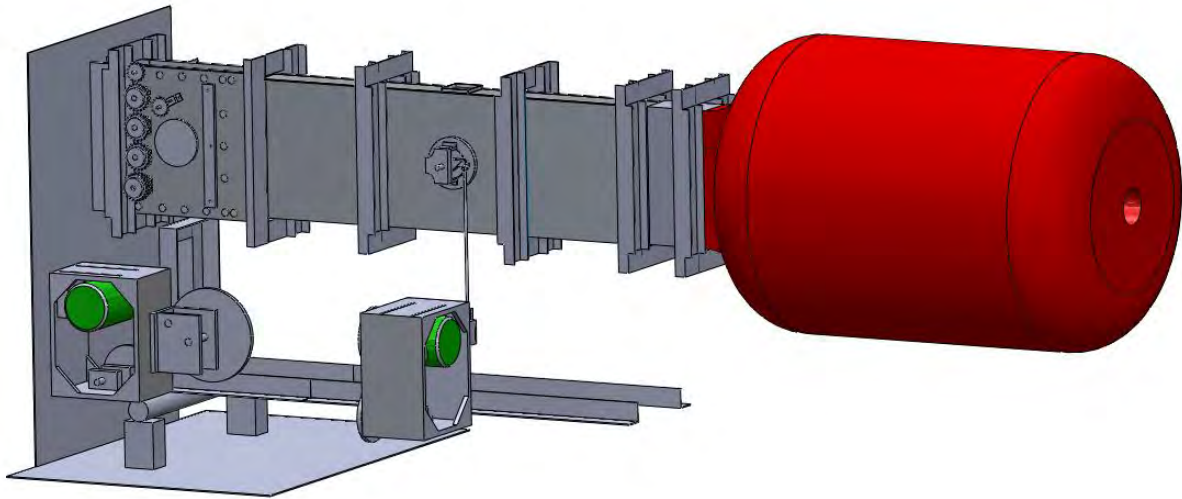
Figure 3: Overview of Mach oscillation and pitch oscillation drive mechanisms.

For an airfoil with a 152.4mm (6") chord length, the Mach number range (0.2-1.0), Reynolds number range (1-8 million), and unsteady reduced frequency capabilities of this facility are ideally suited for studying the rotor dynamic stall phenomenon for both the retreating and advancing blade.

2.2   Airfoil Pitch Oscillation Assembly

An airfoil oscillation mechanism is installed in the 6" × 22" transonic wind tunnel as seen in Figure 3 through Figure 5. The airfoil oscillates about the quarter chord position by a 5-hp variable-frequency A/C motor. The drive chain is configured such that a belt rotates an eccentric disk and a momentum fly wheel to minimize the unsteady aerodynamic loads on the transmission. A lever arm is connected to the eccentric disk by a pin, a connection bar then oscillates the airfoil which has bearings isolating it from the tunnel walls. For this experimental study, the pitch oscillation amplitude (fixed by the groove in the eccentric disk) can be set to either ±5° or ±10°. The mean angle of attack is set by the connection bar length. The angle of attack is quickly adjusted from 0° to 15° in increments of 5° using interchangeable links fastening the top of the connection bar to the airfoil axis of rotation (Figure 5(b)). The oscillating test section has a frequency range of 1-17 Hz. With this range, it is possible to achieve an unsteady reduced frequency of approximately 0.05 at Mach numbers up to 0.45. A shaft-mounted optical encoder with quadrature outputs at 2500 counts per revolution is coupled to the

shaft of the eccentric disk. This signal is sampled at 50 kHz and used to determine the angular position of the airfoil to within ±0.05°.
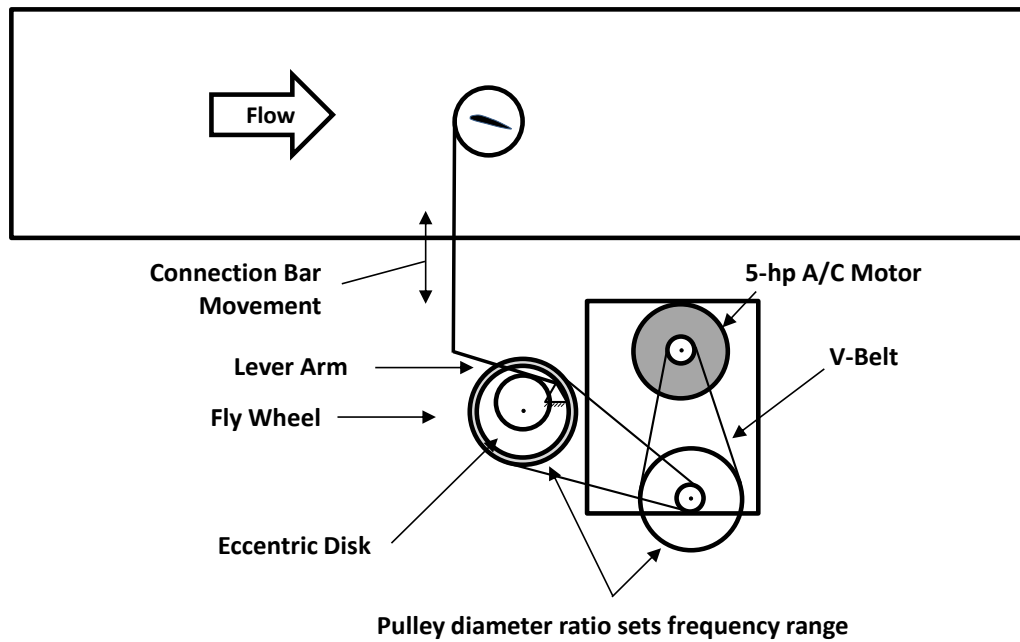
Figure 4: Schematic of the airfoil oscillation device.

(a)   (b)
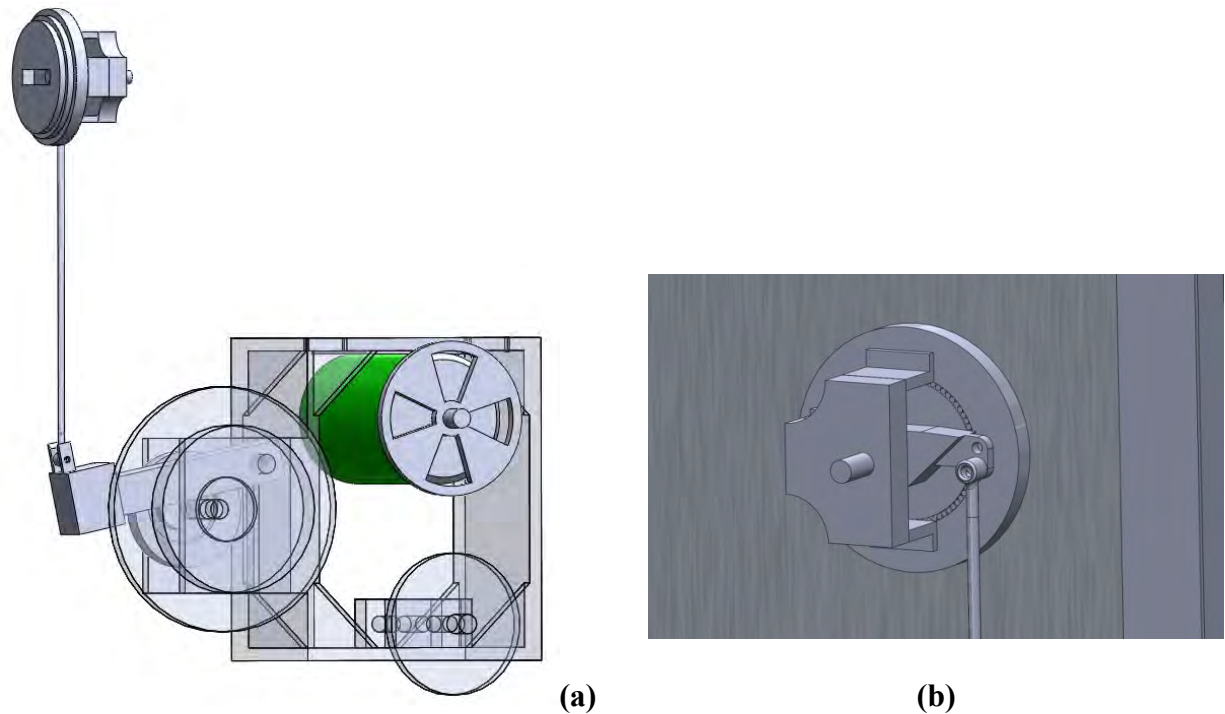
Figure 5: Detail of (a) eccentric disk and drive mechanism, and (b) thrust bearing for pitch oscillation.

2.3 Setting Test-Section Mach Number

In the conventional, time-invariant configuration, test-section Mach number is uniquely controlled independently of Reynolds number by adjusting the throat area (A^*) downstream of the test section. Since the blowdown tunnel is choked at the throat, the test section Mach number is uniquely set by the area ratio independent of the stagnation pressure according to the area-Mach number relation expressed in Eq. (2). The throat area is set by installing choke bars of varied diameter as indicated in Figure 1.

$$\frac{A}{A^*} = \frac{1}{M}\left[\left(\frac{2}{\gamma+1}\right)\left(1+\frac{\gamma-1}{2}M^2\right)\right]^{\frac{\gamma+1}{2(\gamma-1)}} \tag{2}$$

2.4 Freestream Mach Oscillation Assembly

The transonic tunnel has been modified to allow freestream velocity modulation up to 17Hz using a variable-area throat downstream of the test section (refer to Figure 3). The modification uses rotating elongated vanes to control the throat cross-sectional area as a function of time. A drive mechanism rotates four vanes of the profile displayed in Figure 6. As the vanes rotate, the open cross-sectional area is varied between maximum and minimum values, as illustrated by the time-history of A^* also included in Figure 6. The cross-sectional area of the vanes was specified such that the vane rotation produces a sinusoidal Mach number oscillation (0.4 ± 0.08) in the test section. The amplitude of Mach number oscillation is set by the dimensions of the major and minor axes of the rotating vanes, and the specific Mach waveform dictated by the geometry of the vanes.

Design of the choke vanes for a specific Mach waveform (say, $M = 0.4 + 0.08 \sin \theta$ in this case) is not straightforward because there is no deterministic mapping between a required A^* time history and a parameterized vane geometry. Thus, the necessary parameterized vane profile for a given A^* history must be determined iteratively. In order to make this iterative process tractable, a superellipse profile is used to define the vane geometry. The generic definition of a superellipse is

$$\left|\frac{x}{a}\right|^m + \left|\frac{y}{b}\right|^n = 1 , \tag{3}$$

where m and n are both greater than 0. Parametric equations for the vane geometry ($x'(\theta)$, $y'(\theta)$) in Cartesian coordinates are given by

$$x(\theta) = |\cos\theta|^{2/m} \cdot a\,\mathrm{sgn}(\cos\theta)$$
$$y(\theta) = |\sin\theta|^{2/n} \cdot b\,\mathrm{sgn}(\sin\theta)$$

(4)

the major (a) and minor (b) axes of the profile determine the maximum and minimum values of the Mach waveform. Each of the four vanes used in this work have $a = 2.07$ cm (0.82 in.) and $b = 3.25$ cm (1.28 in.). A nonlinear regression was performed while allowing the regression variables m and n to vary to determine the geometry which produces a prescribed sinusoidal test-section Mach number when rotated at constant angular velocity. The parameters which define this choke vane geometry are $m = 1.9833$ and $n = 1.5402$.

The geometrical configuration of the oscillating vanes may be adjusted between runs in a relatively short period of time by interchanging between several sets of pre-fabricated vane assemblies to produce varied Mach number waveforms. The vane assembly is driven by a 4 kW A/C servo motor, which is slaved to the pitch oscillation motor. The drive chain is configured such that adjacent vanes are counter-rotating, to minimize the unsteady aerodynamic loads on the transmission. A shaft-mount optical encoder is coupled to the shaft of the upper-most choke vane to index each full revolution (1/rev) and the angular orientation of the choke vanes (500/rev). The signal is used to determine the oscillation frequency and the instantaneous angular position (θ_{CV}).
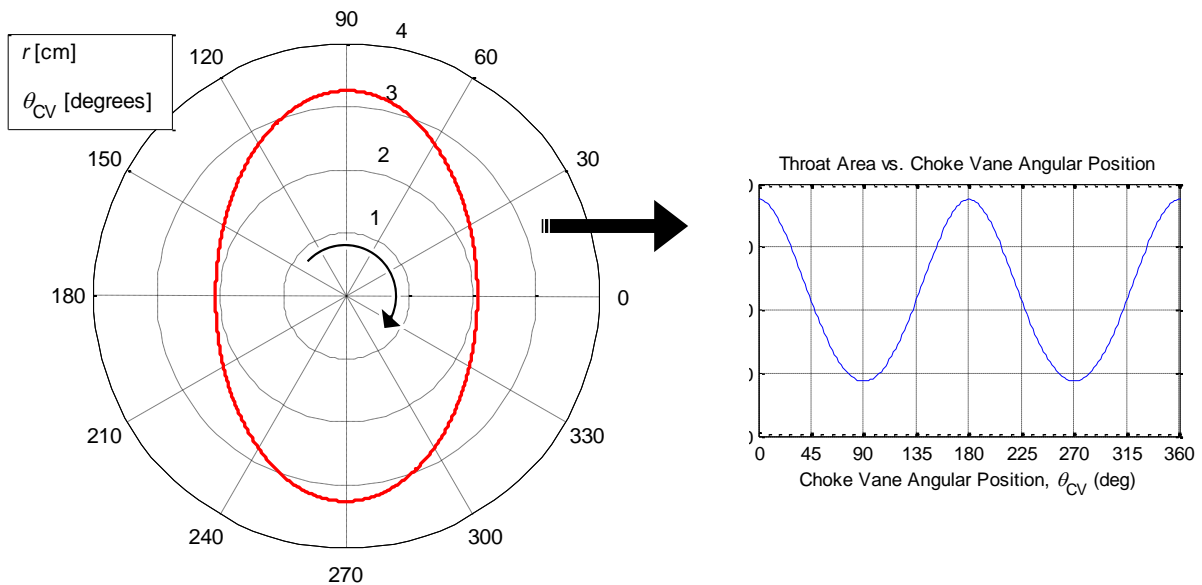
Figure 6: Choke vane geometry and resulting physical throat area variation.

2.5   Freestream Mach Number Measurement

It is well-known that modeling transonic airfoil stall in a wind tunnel can be challenging due to confinement of streamlines that would deform differently in a real freestream condition (Goethert, 2007). Goethert suggests suitable freestream velocity corrections that would be appropriate for this work. However, it is important to select a suitable measurement station for the freestream Mach number. The location should ensure that the airfoil flow is not perturbed by the presence of the probe, and the potential field distortion that results from the presence of the airfoil should be negligible. The potential field distortion is highest when the airfoil is at high angle of attack, which is the condition of interest for this type of study. Furthermore, the time-varying freestream velocity introduces another very important factor in determining the measurement station. In the time-invariant case, the freestream static pressure is measured within the perforated plenums (Figure 1) located above and below the test section. Ordinarily, these plenums serve to better simulate a freestream condition, and dampen shock waves that would otherwise reflect and possibly contaminate the test-section. However, in the case of unsteady flow, the dynamics in these plenums distort the measured freestream velocity waveform.

Two-dimensional computational simulations were performed with Fluent 12.0 to determine the extent of the upstream influence of an airfoil installed in the 6" × 22", and to aid in selecting a suitable location to place a probe for freestream Mach number measurement. These simulations covered a range of freestream Mach numbers from 0.3 to 0.65. The tunnel was modeled as a long rectangular duct with solid wall boundaries. The simulations included viscous effects to capture first order shock-boundary layer effects, and the Spalart-Allmaras turbulence model was used. The simulations were validated by comparing predicted C_p distributions with experimental data for a couple of airfoils (but not the SSC-A09 used in this study). Also sidewall static pressure distributions were compared to ensure validity of the prediction tool for this purpose. Figure 7 shows the domain and the location of data traces that are presented in Figure 8. Observing Figure 8 for a sample case where the inlet Mach number is approximately 0.3, it is evident that placing the probe 0.3 to 0.5m upstream of the airfoil, and 0.2m off of the mid-height will result in a measured Mach number with negligible distortion due to potential effects. Similar conclusions are drawn for other values of freestream Mach number and airfoil angle of attack.
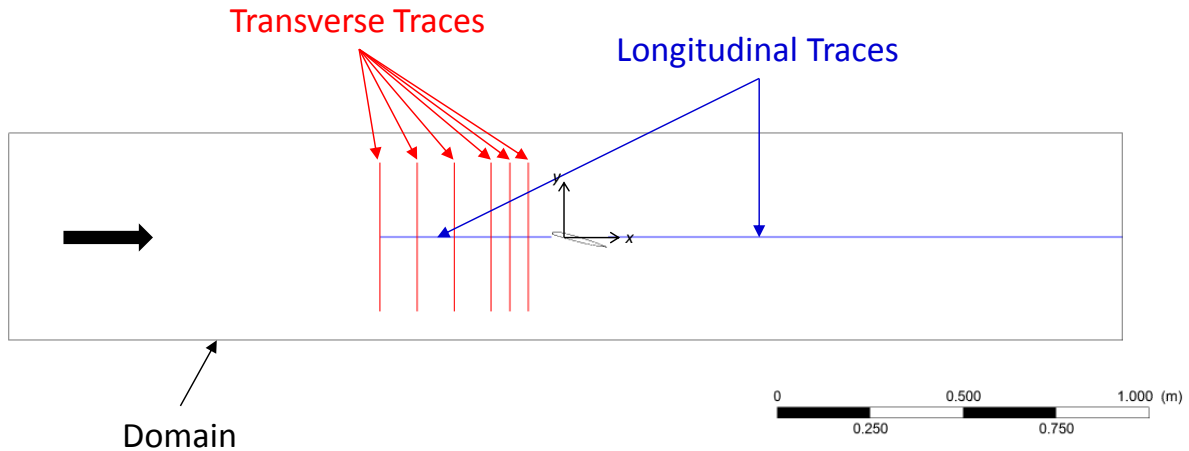
Figure 7: Fluent domain and trace locations.

A Pitot-static probe is mounted approximately 0.5m (3.3 chord lengths) upstream of the airfoil leading edge and 0.2m (1.3 chord lengths) above the airfoil. Each sensor orifice is connected to a miniature pressure transducer via a short length of plastic tubing. Pneumatic corrections are applied in the same manner outlined in a later section discussing dynamic response considerations for unsteady pressure measurements. The Pitot-static probe accurately resolves pressure fluctuations at frequencies up to 500Hz which is sufficient to resolve the expected the frequency content. The ratio of static pressure to the stagnation pressure is used to calculate the test section Mach number via the isentropic pressure relationship. The calibration uncertainty of measured Mach number is ±0.005.
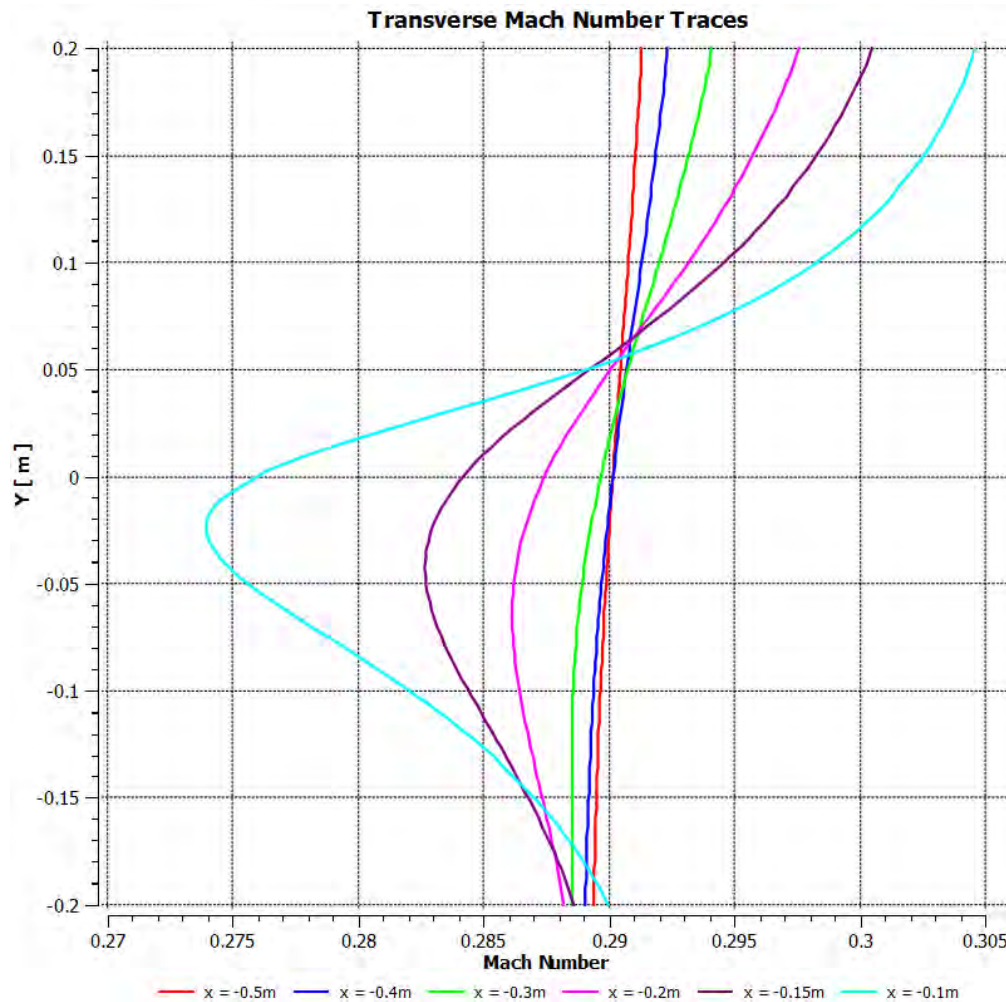
Figure 8: Transverse traces of predicted Mach number at several locations upstream of test article.

2.6 Stagnation Temperature

The flow temperature decreases at a rate of approximately 0.5K/s (1°F/s) as air is discharged from the constant-volume high pressure tanks. Consequently, the speed of sound can decrease by as much as 9 m/s during a 30-second run. A Type J thermocouple is used to measure the stagnation temperature which is recorded at a rate of 10 Hz to the 6" × 22" control computer. Static temperature in the test section is determined via the isentropic temperature relation using the freestream Mach number (measured with the Pitot-static probe).

2.7 Airfoil Surface Pressure Data

Airfoil surface pressure taps are connected to an ESP Pressure Scanner System to obtain the static pressure distribution along the airfoil surface. The pressure-coefficient (C_p) is calculated at each tap location as defined in Eqn. (5),

$$C_p = \frac{P/P_\infty - 1}{0.5\gamma M_\infty^2}.$$ (5)

The trapezoidal rule is used to integrate the C_p curve, and calculate the sectional lift (C_L) and moment (C_M) coefficients. It is noted that C_L and C_M measurements inherently omit contributions of skin friction forces.

Two ESP 32HD Pressure scanners are mounted just outside the wind tunnel and the pressure ports are connected to airfoil pressures via durable plastic tubing of 1mm-diameter (0.040in.). The ESP scanners are miniature electronic differential pressure measurement units consisting of an array of 32 silicon piezoresistive pressure sensors (±210kPa differential), one for each port. The electrical outputs of the sensors are electronically multiplexed through a single onboard instrumentation amplifier at switching rates up to 70,000Hz using binary addressing. The multiplexed amplified analog output is connected to a DTC Initium scanner interface and streamed via Ethernet to a dedicated hard disk. In order to ensure data streaming at a stable sample interval, the Initium is triggered with an external TTL pulse train which is generated by the 6" × 22" control computer. In this hardware trigger mode, the maximum scanning rate is 1,200 samples/sec per sensor. Also, triggering assures accurate temporal correlation with the various other analog voltage signals being recorded by the control computer. Aside from the high data rates, the ESP Scanner System features individual sensor thermal compensation to minimize zero and span shifts with temperature which are inherent in silicon pressure sensors.

The ESP scanners also incorporate a two-position calibration manifold actuated by momentary pulses of control pressures. When placed in the calibrate position, all sensors are connected to a common calibration pressure port. To ensure the highest accuracy, an automated five-point calibration is performed periodically by applying a sequence of accurately measured pressures through this port. The transducers are accurate to within ±0.03% or better of the full scale (FS) pressure range.

2.8 Dynamic Response Considerations

Combined with the effect of tubing diameter and length, the small ESP sensor volume (with high natural frequencies) is key to minimizing the pneumatic distortion associated with remote pressure sensing schemes. A minimal length of tubing (approximately 20cm long) was used to uniformly transmit all airfoil surface pressures to the ESP Pressure Scanners.

Attenuation of measured pressure signals due to viscous effects in the tubing-sensor system is considered before taking dynamic pressure measurements. Bergh and Tijdeman developed an analytic model which corrects for attenuation and phase lag associated with pneumatic tubing (Bergh and Tijdeman, 1965). The model characterizes the dynamic response of the tubing as a function of the geometry of the tubing (inner diameter and length) and transducer (sensor volume), along with the ambient conditions. The Bergh and Tijdeman model (referred to as B-T in Figure 9) is a transfer function that ratios the pressure measured by the transducer with the actual unsteady pressure at the surface pressure tap in the frequency domain. An acoustic excitation test bed was used to generate sinusoidal pressure oscillations over a relevant frequency range. The oscillating pressure was measured with representative tubing connecting pressure ports in the test bed to the ESP scanners. Also, the oscillating pressure was measured with a flush-mounted piezoelectric transducer. The amplitude ratio (AR = amplitude measured with ESP : amplitude measured with Kulite) is plotted vs. excitation frequency in Figure 9 along with the B-T model predictions. The empirical data and model predictions are in excellent agreement, providing a suitable scheme for attenuation and phase compensation of unsteady pressure data.
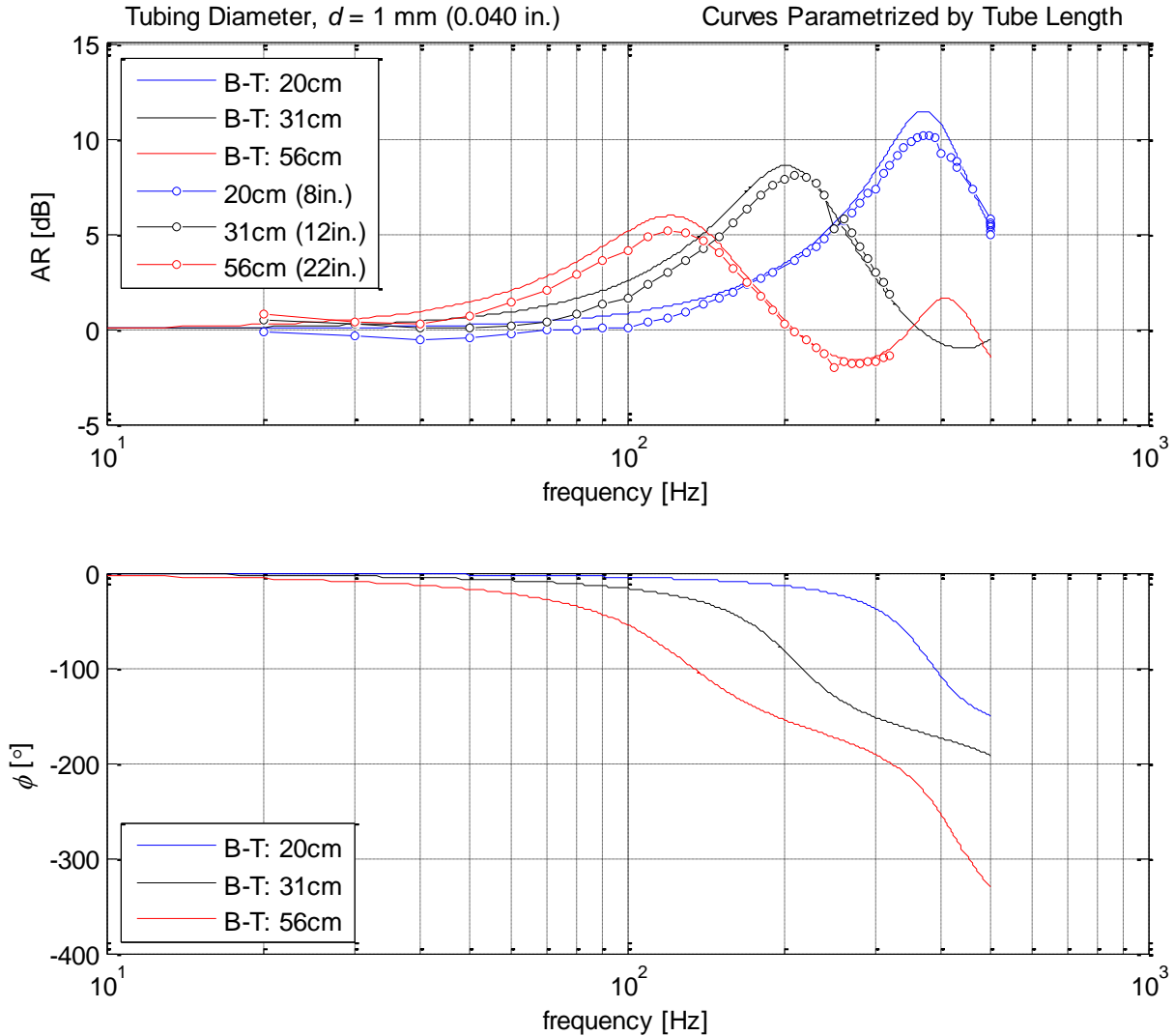
Figure 9: Comparison of measured ESP pressure sensor dynamic response and Bergh-Tijdeman model (ref. Bergh and Tijdeman, 1965) for representative lengths of pneumatic tubing (diameter = 1 mm = 0.040in.).

2.9   Test Article

The model used in this experimental campaign is an airfoil with the Sikorsky SSC-A09 profile which is shown in Figure 10. The surface coordinates and derivatives are identical to those published by (Lorber and Carta, 1987) and they are tabulated in Appendix 1. The leading edge radius is 0.7% of chord. The maximum thickness of the airfoil is 9% located near 38% chord. The thickness distribution is relatively flat between 20% and 60% chord to promote healthy performance under supercritical flow conditions.

The model is fabricated from solid aluminum using wire Electrical Discharge Machining. An isometric view of the airfoil drawing is displayed in Figure 10(a). Both the chord and the span

are 152.4mm (6 in.), yielding an aspect ratio equal to 1. One end of the model mates with a "rectangular side block" which is used to rigidly mount the airfoil in the wind tunnel test section while the other end terminates with a "tap output boss". The model has a 25.4mm-deep pocket (with a minimum wall thickness of 1.27mm) carved into the boss-side wherein all the plastic lines transmitting model surface pressures are bundled and snaked through the tap-output boss.

The model is outfitted with 53 surface pressure taps to measure aerodynamic forces and moments. Tap locations are shown in Figure 10(b) and tabulated in Appendix 2. There are 30 taps on the upper surface, and 23 on the lower surface (including the leading edge tap). The tap distribution covers the leading 82% of chord. Coverage on the trailing 20% is challenging because of the limited workspace within the pocket design and the airfoil thickness in general. In the absence of a trailing edge tap, a ghost tap is created in post-processing whereby the trailing edge pressure is estimated to be the average of the downstream-most taps on the upper and lower surfaces. Tap spacing is denser in the leading 30% of chord in order to better resolve the large pressure gradients. However, the spatial resolution of surface pressure within the leading 2.5% chord is limited by manufacturing and design constraints. The internal spanwise cavities which transmit surface pressures to the edge of the airfoil are separated by one hole diameter of material to avoid breaching between adjacent cavities during manufacturing. The hole diameter is limited by the distance the drill must plunge to reach the midspan. An assessment of the impact of tap resolution on the integrated quantities of lift and moment was given by Hird *et al*. (2014).

The taps are staggered across the middle third of the model span to prevent adjacent taps from interfering with one another. All taps are located on a plane which makes a 19° angle with the airfoil midspan plane. The stagger angle is such that the turbulent wedges which might originate from a pressure tap do not cover other taps. Taps are plunged normal to the surface with a 0.3mm-diameter (0.013in.) to a depth of 1.27mm where they intercept the 1.27mm-diameter (0.050in.) spanwise pressure lines. All internal spanwise pressure lines in this model terminate in the airfoil pocket with a stainless steel tubulation with 1.27mm inner diameter that connect via durable plastic tubing to the pressure scanners. The exit orifices can be seen on one side in Figure 10. Uniform tap geometry was used in an effort to simplify the dynamic response characterization and compensation which is discussed later. Thus, the total length of the tubing

measured from each tap to the pressure transducer is 20cm (8in.), and there are no discontinuities of tubing inner diameter (1.27mm) along that length.

(a)

(b)
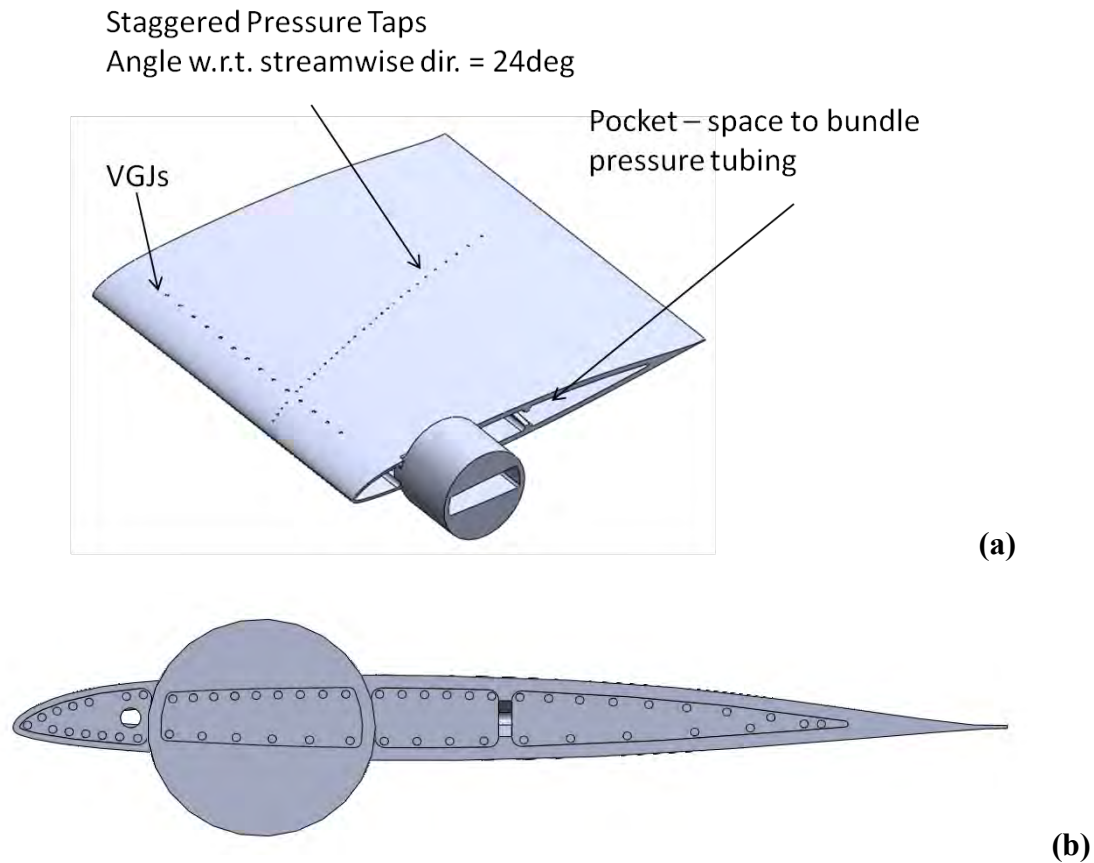
Figure 10: SSC-A09 Airfoil used in this work: (a) isometric view and (b) side view showing tap distribution.

2.10 Uncertainty Estimates

An analysis was conducted in the manner outlined by Coleman and Steele (1999) to estimate the relevant calibration uncertainties at $M = 0.3$ with the wind tunnel in steady-flow mode: Mach number, +/-0.005; Reynolds number, ±5,000, angle of attack, ±0.05°, C_P, ±0.05, C_L, ±0.05, C_M, ±0.02, C_D, ±0.001, and T_∞, ±0.05K.

3. Results

The objectives of this experimental research include establishing the significance of and understanding the impact of time-varying compressibility on compressible dynamic stall. There are three unsteady scenarios which are simulated experimentally. The first scenario is that of the oscillating airfoil in a steady airstream. The dynamic stall encountered in this scenario constitutes

the conventional simulation of the dynamic stall process that has contributed to our understanding of the key physical phenomena. The second scenario involves evaluation of how hysteresis and stall are impacted when a fixed-pitch airfoil is subjected to a time-varying freestream Mach number condition. Finally, the airfoil model oscillations are synchronized with the freestream velocity oscillations for coupled pitch and Mach oscillations. Moreover, measurements are made while varying the phasing relationship between these synchronized oscillations. Through this progression, the impact of time-varying compressibility on the compressible dynamic stall process is elucidated.

3.1   Pitch Oscillations with Fixed Mach number

The first phase of this work is focused on the conventional understanding of dynamic stall for the case of an airfoil model executing sinusoidal oscillations of pitch in a steady airstream. Comparisons are made with historical data (Lorber and Carta, 1987) for $M = 0.2$ and $\alpha \approx 10° - 10°\cos\varphi$ to validate the experimental facility and methodology. Then the impact of compressibility on dynamic stall is systematically inspected for $M = 0.2$, 0.4, and 0.6 and $\alpha \approx 10° - 10°\cos\varphi$.

3.1.1   Introductory Comments

Figure 11 is a composite figure which shows phase-averaged measurements for a typical dynamic stall test in the OSU 6" × 22" transonic wind tunnel for the case of an oscillating airfoil in a steady airstream. The particular test conditions are $M = 0.2$, $\alpha \approx 9° - 11°\cos\varphi$, and $k = 0.050$. As with all pitch oscillation data reported in the current study, maximum α is set to 20° with the pitch oscillation assembly unpowered. The figure includes curves of lift and moment coefficient on the left-hand-side. Contours of upper surface pressure coefficient are plotted in the middle with chordwise position along the abscissa and phase angle along the ordinate. The angle of attack is plotted on the right with angle along the abscissa and phase angle along the ordinate. The C_p contours show the development of suction during the upstroke terminating with the formation and convection of the leading-edge vortex (LEV). The tongue of depressed C_p contours which extends over the leading 50% of chord from $140° < \varphi < 160°$ is the LEV signature. As the LEV convects past the trailing edge of the airfoil, the C_p plateaus for $160° < \varphi < 225°$, indicative of an open separation starting from the leading edge. This persists while the airfoil begins the downstroke until $\varphi = 225°$ when reattachment begins from the leading edge and

progresses downstream toward the trailing edge until the flow is fully attached at $\varphi \approx 270°$. Integrating the phase-averaged C_p distribution in this sequence produces the hysteresis C_L and C_M loops presented on the left. While suction development is stable during the upstroke the lift-curve slope is approximately constant until $\alpha \approx 18°$. The elevated suction coinciding with the LEV formation can produce a brief dynamic lift enhancement before the vortex convects past the airfoil. Evidence of this lift enhancement is sometimes more pronounced for different cases, though not to the expected level which will be discussed later. The lift coefficient abruptly decreases from 1.5 to 0.8 for $19° < \alpha < 20°$ while the vortex passes over the airfoil surface. As the downstroke begins and the airfoil is completely stalled, C_L is at a value of approximately 0.6 until $\alpha = 8.5°$ ($\varphi = 270°$) whereafter the lift-curve slope matches the value measured during the upstroke. The moment coefficient is of special interest when analyzing the dynamic stall process because of the aeroelastic implications. The impulsive aerodynamic moment experienced by a rotor is transmitted through the structure to the pitch linkage at the rotor hub. By virtue of the coupling between the aerodynamic and structural dynamics, this cyclic forcing can cause flutter and/or high-cycle fatigue of the pitch linkage. Thus, it is important that the measurement adequately resolve the pitching moment behavior. During the upstroke, for $-2° < \alpha < 18°$, C_M does not vary suddenly although it has as slightly negative slope which will be discussed in more detail. When the LEV is initialized, and before it convects past the quarter chord, the pressure near the LE is lower, and the moment about the quarter chord is slightly negative (nose down). As the LEV convects past the quarter, the pressure distributions shifts so that the upper surface pressure near the leading is high and the pressure downstream of the quarter chord is low, causing the negative moment to suddenly decrease to a peak $C_M = -0.18$ at $\alpha \approx 19°$. After the vortex has convected past the airfoil, for $19° < \alpha < 20°$, C_M increases to -0.12. As the downstroke begins, C_M gradually increases until the upper surface flow reattaches after which the measured C_M is relatively weak and approximately constant.
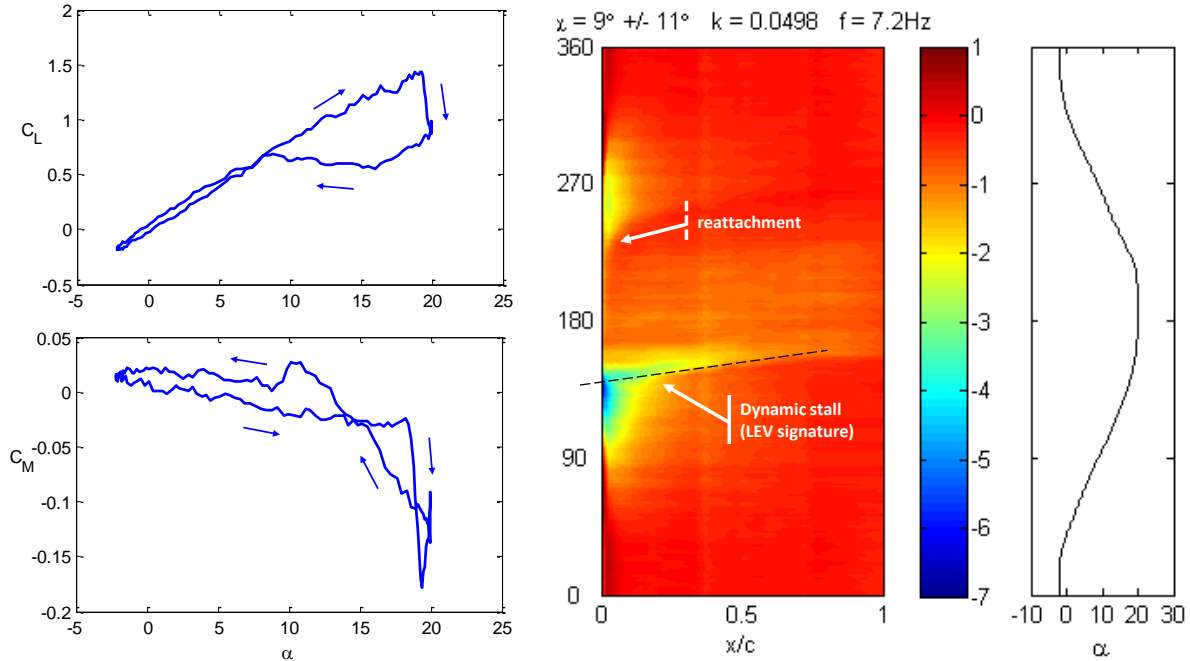
Figure 11: Phase-averaged C_L (upper left), C_M (lower left), C_p contours (middle) and angle of attack for $M = 0.2$, $\alpha = 9° - 11° \cos \varphi$, and $k = 0.050$.

3.1.2 Dynamic Response Considerations

Temporal resolution of the dynamic stall process measured via the remote pressure sensing scheme outlined in Section 2.7 is one of the ultimate concerns which needs to be addressed before further analysis of the data. Assuming that it is sufficient to resolve content at frequencies 5-6 multiples of the first harmonic of the pitch oscillations (20 Hz), a sufficient frequency response should be flat out to approximately 120 Hz. Furthermore, the pneumatic distortion associated with the remote pressure sensing scheme is a strong function of the mean pressure (Bergh and Tijdeman, 1965). Thus, the maximum distortion is expected for low freestream Mach numbers (generally high tunnel and model surface pressures). Figure 12 displays two oscillation periods of raw pressure traces recorded for the first ten taps on the upper surface (including the leading edge tap) for the case of $M = 0.2$, $\alpha = 9° - 14° \cos \varphi$, and $k = 0.135$ ($f = 19.5$ Hz). The leading tap is designated Tap #1 and tap number increases marching along the upper surface in the downstream direction. An offset equal to the product of 0.5 psi and the tap number is added to each pressure trace to spread out the traces and improve visibility. Traces are compared without (left) and with (right) pneumatic compensation. The difference between traces with and without pneumatic compensation is subtle. High frequency fluctuations are smoothed over as if they were low-pass filtered, and the peak negative pressures observed just before the onset of

stall ($t/T = 0.5$ and 1.5) are also slightly attenuated. Figure 13 compares the corresponding Fourier series coefficients for the tap indicating the most power of high-frequency pressure fluctuation (tap #2, see Appendix 2). The upper plot in this figure shows the Fourier coefficients scaled by a factor of five in order to include the compensation transfer function (amplitude ratio) on the same plot. Evidently 95% of the power in this signal is resolved within $0 < f < 200$ Hz through the first ten harmonics of the oscillation frequency. The amplitude ratio function indicates negative attenuation (resonance) with a peak amplitude ratio of 4 at approximately 300Hz. The amplitude ratio is 1.84 at 200Hz and the phase is $-19°$. This means that high frequency content is physically amplified in this tubing-transducer configuration. Whereas most remote pressure sensing schemes involve positive attenuation and a potential loss of high frequency information, the frequency response in this case is beneficial because high-frequency content is preserved. Also, the power in high frequencies is not overwhelming in the sense that it would distort lower frequency content. Thus, the pressure traces in Figure 12 appear to be filtered when compensation is applied. This analysis suggests that the dynamic response characteristics of the tubing-transducer system are adequate to resolve the unsteady dynamics in this flow scenario.
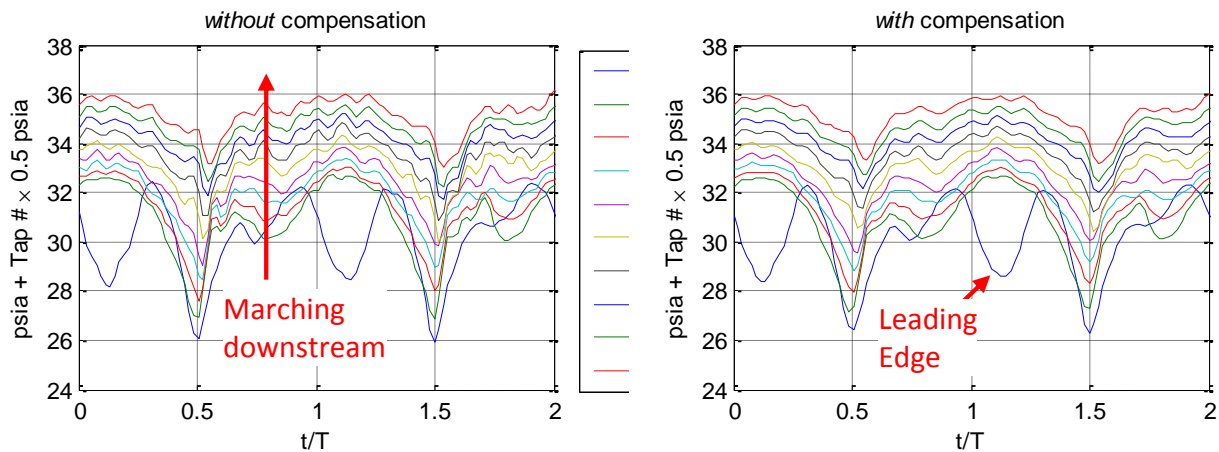
Figure 12: Comparing two periods of raw pressure traces for $M = 0.2$, $\alpha \approx 9° - 14° \cos \varphi$, and $k = 0.135$ ($f = 19.5$ Hz).
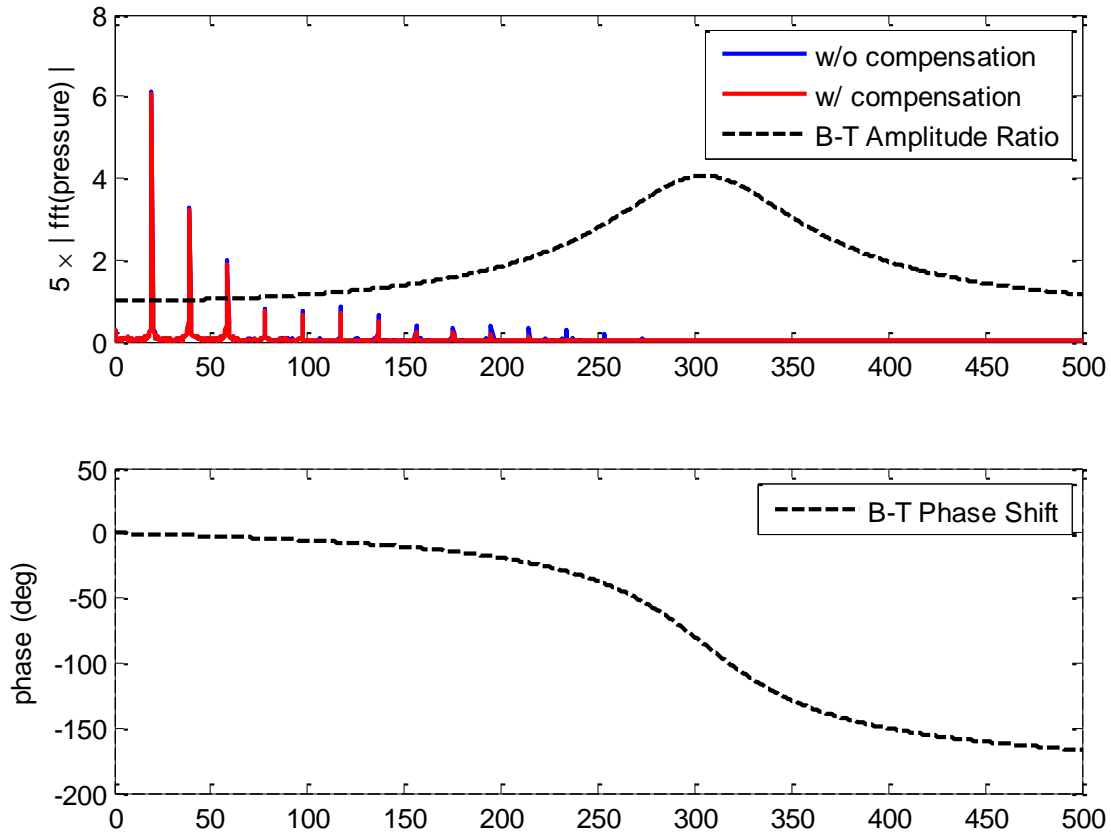
Figure 13: Spectra of pressure traces (tap #2), plotted along with pneumatic compensation transfer function. $M = 0.2$, $\alpha \approx 9° - 14° \cos \varphi$, and $k = 0.135$ ($f = 19.5$ Hz).

3.1.3   Validation with Historical Data

Figure 14 through Figure 16 are comparisons of OSU data and historical data which has been digitally extracted from graphical images in Lorber and Carta (1987), also cited in some figures as AFOSR TR 87-1202. Comparisons are made for $M = 0.2$, $\alpha \approx 10° - 10° \cos \varphi$, and reduced frequencies (k) equal to 0.025, 0.050, and 0.100. The angle of attack oscillations for $k = 0.025$ and 0.050 have similar maximum α between the OSU and Lorber and Carta's data. However, for the case of $k = 0.100$, the maximum α of the OSU oscillation is 2° higher. Although the OSU pitch oscillation is periodic, it is difficult to control the oscillation amplitude because of structural vibration of the pitch oscillation assembly. For any of the selected cases, there is a discrepancy in C_L which increases throughout the upstroke. Also, the OSU data indicates a slightly negative C_{M_α} during the upstroke whereas the Lorber and Carta data indicates a

$C_{M_\alpha} \approx 0$. These two differences are attributed to the spatial resolution of surface pressure near the leading edge of the OSU airfoil model (see Section 2.9). The onset of lift stall and moment stall is similar between both datasets for $k = 0.025$ and 0.050. Generally, the OSU data indicates stall onset during the upstroke at an $\alpha \approx 0.5°$ higher than indicated by the Lorber and Carta data. For the case of $k = 0.100$, both datasets indicate that the flow is attached throughout the entire upstroke and stall occurs at the maximum α as the airfoil begins the downstroke. Apart from the interval of LEV formation and convection, the post-stall C_L and C_M values are of similar magnitude during the downstroke, but the OSU data indicates lower moment magnitudes in all three cases prior to reattachment. During this portion of the pitch-oscillation period, the contributions to the C_L and C_M by the pressure distribution about the leading edge are diminished. Thus, the error due to the leading edge spatial resolution is less significant, and the agreement between the two datasets is improved. Reattachment trends are also similar between the two datasets. As reduced frequency increases, reattachment generally occurs later during the oscillation period. Reattachment seems to occur slightly earlier for the OSU model. The reattachment angle of attack is $2°$, $1°$, and $1°$ higher in the OSU data for $k = 0.025$, 0.050, and 0.100, respectively. The peak negative moment spike is of particular concern, and there are notable discrepancies between the two datasets. In all cases, the OSU measurements indicate lower moment spike magnitudes. The magnitude of the peak moment of the OSU data is 41%, 50%, and 32% lower than the Lorber and Carta measurement for $k = 0.025$, 0.050, and 0.100, respectively.
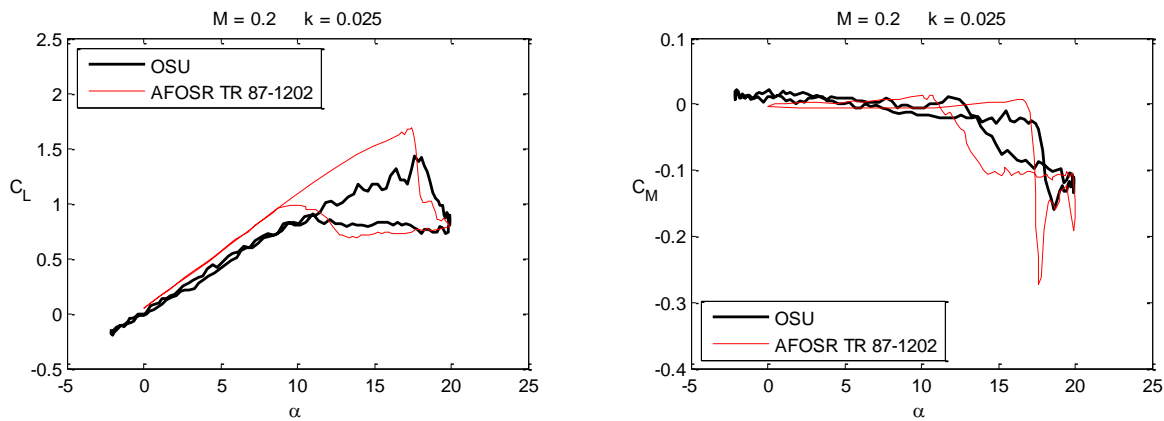
Figure 14: Comparing OSU data to historical data: lift (left) and moment (right) coefficient orbits for $M = 0.2$, $\alpha \approx 10° - 10° \cos \varphi$, and $k = 0.025$.
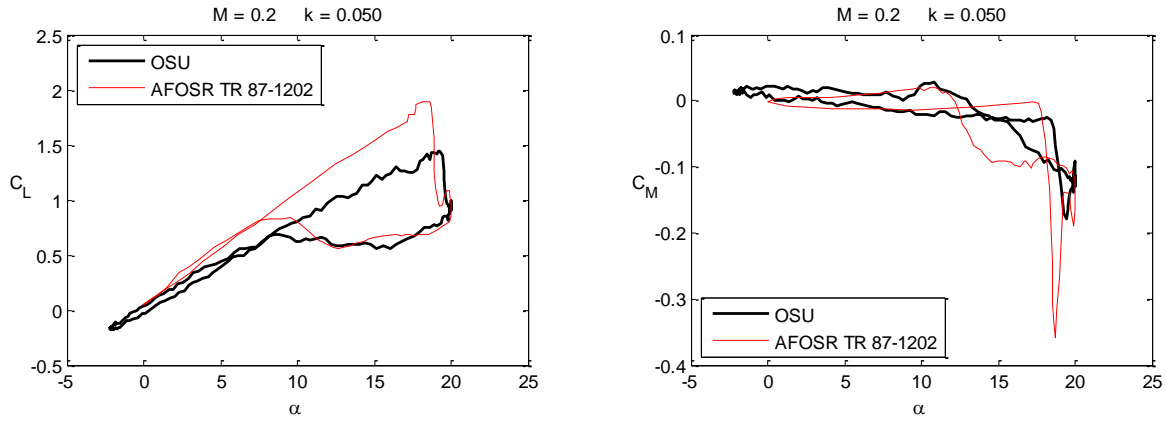
Figure 15: Comparing OSU data to historical data: lift (left) and moment (right) coefficient orbits for $M = 0.2$, $\alpha \approx 10° - 10° \cos \varphi$, and $k = 0.050$.
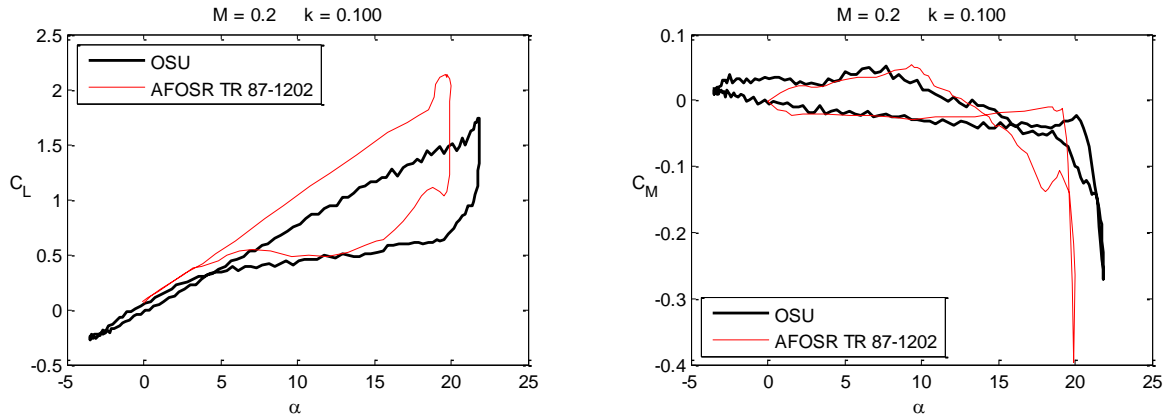
Figure 16: Comparing OSU data to historical data: lift (left) and moment (right) coefficient orbits for $M = 0.2$, $\alpha \approx 10° - 10° \cos \varphi$, and $k = 0.100$.

Figure 17 compares phase-averaged pressure traces between both datasets for the case of $M = 0.2$, $\alpha \approx 10° - 10° \cos \varphi$, and $k = 0.050$. The relative validity of this comparison is optimal because the pitch oscillation amplitude and maximum angle are a closer match than for $k = 0.100$. Traces are selected for upper surface pressure tap locations ($x/c \approx 0.025$, 0.220, 0.460) which are co-located to within 0.5% of chord between the two airfoil models. Traces are offset for visibility. The peak suction registered by each of the pressure taps during the upstroke ($0 < t/T < 0.5$) is comparable between the two datasets. However, the peaks occurring in the OSU measurements exhibit a progressive phase lag relative to the Lorber and Carta measurements. The tap at $x/c = 0.025$ shows the collapse of the suction peak near the leading edge occurring at approximately the same phase ($t/T = 0.37$), and the slope of the pressure rise with time is only slightly steeper for the Lorber and Carta data. The pressure rise signal convects past the

subsequent pressure taps of Lorber and Carta more quickly than observed in the OSU taps. This is consistent with the delayed onset of stall observed for the OSU data in Figure 15. Both models show evidence of stall for $0.45 < t/T < 0.7$, although the Lorber and Carta pressures are consistently higher during this interval. This behavior explains why Lorber and Carta's moment coefficient is slightly more negative during the beginning of the downstroke. Earlier reattachment in the OSU data is evident beginning at $t/T = 0.62$ at $x/c = 0.025$, and the reattachment starts near the leading edge and progresses downstream. The difference between the two models in attached flow pressures is negligible.

While an unsteady interference evaluation has not been performed for testing in the 6" × 22" transonic wind tunnel, it is speculated that the reason why suction levels on the OSU model are persistently higher than on Lorber and Carta's model is associated with the aspect ratio. The aspect ratio is 1 and 5.5 for the OSU and Lorber and Carta's models, respectively. The low aspect ratio can corrupt the two-dimensionality of the flow as the airfoil stalls, and can promote artificially high velocity in the midspan region as endwall boundary layers effectively constrict the midspan flow. In the context of the dynamic stall experiment, this impact of low aspect ratio may be to delay the onset of dynamic stall, promote early dynamic reattachment, and weaken the LEV vortex, thereby reducing the strength of the pitching moment spike. A suitable interference evaluation might consist of unsteady testing using congruent airfoil models of increasing aspect ratio to determine the aspect ratio above which the time-resolved C_p is constant. For lack of interference information, it is surmised that the measurement methodology is adequate to resolve the unsteady fluid dynamics, while the scale of the model may be reduced to improve the validity of future experiments.
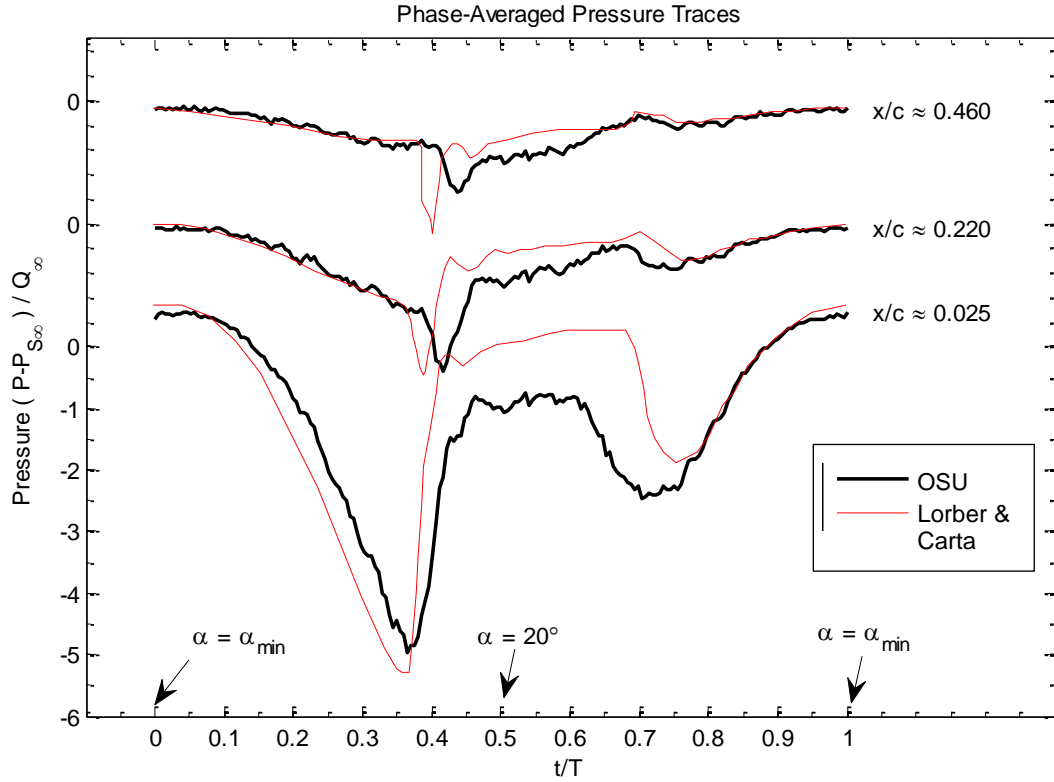
Figure 17: Phase-averaged pressure traces from OSU and historical data. Traces for three chordwise positions, offset for visibility. Test condition: $M = 0.2$, $\alpha \approx 10° - 10° \cos \varphi$, and $k = 0.050$.

3.1.4 Compressibility Effects

The results acquired for the oscillating clean airfoil in a steady airstream are presented in two ways. Lift and moment coefficient orbits are presented in Figure 18 through Figure 20 for fixed freestream Mach number to illustrate the impact of reduced frequency. Results are then presented for fixed reduced frequency (Figure 21 through Figure 23) to understand how the dynamic stall process is impacted by increasing the freestream Mach number and elevating the role of compressibility effects.

Dynamic stall experiments were performed for three values of freestream Mach number, namely 0.2, 0.4, and 0.6. In all tests the target pitch oscillation profile is $\alpha \approx 9° - 11° \cos \varphi$, with the target amplitude dictated by the geometry of the cam in the pitch oscillation assembly (see Section 2.2). As mentioned previously, the maximum angle of attack is set to 20° with the pitch oscillation unpowered. Attempts to minimize the vibration of the pitch oscillation assembly during operation were productive. However, vibrations persist which cause the measured angle of attack amplitude to increase with frequency. The difficulty in controlling the pitch amplitude

can make it challenging to parse the effects of reduced frequency. For instance, as the pitching amplitude increases, the angular acceleration and effective frequency at the onset of stall or reattachment may be slightly higher. Generally, test dynamic stall experiments were performed in increments of $k = 0.025$ up to the limit of the pitch oscillation assembly.

For $M = 0.2$ (Figure 18), data points are presented for five k values up to a maximum of $k = 0.125$. As reduced frequency increases, the onsets of both dynamic stall and dynamic reattachment are delayed. For $k \geq 0.075$, attached flow is sustained up to the maximum angle of attack during the upstroke, and dynamic stall occurs as the airfoil begins the downstroke. As expected, hysteresis effects become more exaggerated with increasing frequency. The post-stall C_L decreases indicating a stronger stall and larger fluctuations in lift force throughout a pitching cycle. The peak negative pitching moment increases with reduced frequency. For the attached flow interval of the oscillation period, the sign of the measured moment flips between upstroke (nose down) and downstroke and the magnitude increases with frequency during the downstroke.

Figure 19 presents data for three reduced frequencies up to a maximum of $k = 0.070$ for $M = 0.4$. The onsets of stall and reattachment are similarly delayed. Stall occurs before the airfoil reaches peak angle of attack in all cases presented. The portion of either the lift or moment curves during the onset of stall is referred to as the stall characteristic. For $M = 0.4$, the stall characteristic in either C_L or C_M is of similar slope for all reduced frequencies. As the timescale of the airfoil motion is reduced relative to the fluid dynamic timescales, the slope of the moment stall characteristic decreases in magnitude. Moreover, the range of peak negative moment values is only 0.035 compared to 0.07 for the same range of k at $M = 0.2$. As with $M = 0.2$, the disparity in C_M values between attached flow portions of the upstroke and downstroke increases with reduced frequency. However, unlike the $M = 0.2$ orbits, there is a notable difference in the in C_L values between attached flow portions of the upstroke and downstroke for $M = 0.4$. Generally, C_L is 0.2 higher after dynamic reattachment than during the upstroke ($\alpha < 5°$), and the dissimilarity increases slightly with reduced frequency.

Only two conditions are presented in Figure 20 for $M = 0.6$. Similar assertions can be made about the effect of increasing reduced frequency regarding the delay of dynamic stall and reattachment. As with $M = 0.4$, the C_L and C_M stall characteristics have similar slope for both reduced frequencies. Evidently, enhanced compressibility brings about a pronounced C_L hysteresis effect during the attached interval of the cycle. The C_L measured after the dynamic

reattachment is consistently higher than the values measured during the upstroke. The largest difference in C_L between upstroke and downstroke is approximately 0.3 for $k = 0.025$ ($\alpha \approx 4°$) and 0.4 for $k = 0.050$ ($\alpha \approx 0°$).

Figure 21, Figure 22, and Figure 23 are organized to show C_L and C_M hysteresis loops for varied M and fixed $k = 0.025$, 0.050, and 0.075, respectively. Orbits of $k = 0.025$ are inspected first. Increasing freestream Mach number causes stall earlier during the upstroke. The maximum C_L occurs at $\alpha = 17.5°$, 16.5°, and 14° for $M = 0.2$, 0.4, and 0.6, respectively. For α higher than the value of maximum C_L, the lift-curve slope deviates from the pre-stall value. On the other hand, the departure of C_{M_α} from pre-stall values precedes lift stall depending on Mach number. For $M = 0.2$, the departure of C_{L_α} and C_{M_α} coincide at approximately 17.5°. For $M = 0.4$, the departure of C_{M_α} occurs approximately 1° before that of C_{L_α}. For $M = 0.6$, C_{M_α} changes approximately 1.5° before C_{L_α}. The slope of both C_L and C_M stall characteristics decrease in magnitude as M increases. The steep characteristic of the $M = 0.2$ case is indicative of leading edge stall behavior which is typically experienced by an airfoil executing sinusoidal or ramping motion through the stall boundary in an incompressible flow. In this flow scenario, wall bound vorticity coalesces at the leading edge into a strong spanwise vortex (the LEV). The collapse of the suction peak near the leading edge coincides with the downstream convection of the LEV, which leaves behind an open separation emanating from the leading edge. As compressibility effects become more important, flow around the leading edge becomes supercritical. If the flow expansion dictated by the geometry and pressure gradient is sufficiently strong a normal shock will form on the upper surface to facilitate the pressure rise. Furthermore, if the flow speeds developed around the leading edge are sufficiently high (local $M > 1.2$), the shock wave / boundary layer interaction can induce stall. In the scenario involving an oscillating airfoil, the point of incipient stall does not begin at the leading edge, though it does gradually migrate upstream as α continues to increase. The shock is strongest (largest pressure rise across) and furthest downstream when streamline curvature around the leading edge is maximum. When the boundary layer thickens, the effective geometry seen by oncoming flow is altered such that the streamline curvature decreases as does the shock strength. The shock also moves upstream. Thus, as the stall develops and grows in size, the shock moves upstream and disappears. The stall behavior is termed a trailing edge type since it does not emanate from the leading edge and it

produces stall characteristics which are less abrupt. The stall process transformation from leading-edge to trailing-edge type can inhibit the formation and strength of the LEV and result in lower peak negative moment magnitude as evident in Figure 21. The post-stall C_L and C_M values are remarkably similar. Post-stall C_L and C_M values collapse for all three Mach numbers to approximately $C_L = 0.8$ during the downstroke ($20° > \alpha > 10°$) and $C_M = -0.12$ at $\alpha = 20°$. The reattachment behavior indicated in C_M are more similar from $M = 0.4$ and 0.6, with pitching moment returning to attached flow values at $\alpha \approx 10°$. Meanwhile C_M returns to attached flow values closer to $\alpha \approx 12°$ for $M = 0.2$. Perhaps more striking is that dynamic reattachment is evident in C_L at $\alpha \approx 9°$ for all three Mach numbers. The effect of compressibility on the hysteresis behavior of the attached flow C_L is also very clear even at the lowest reduced frequency.

Comparisons are also made in Figure 22 across all three Mach numbers for increased $k = 0.050$. As with $k = 0.025$, the stall characteristics exhibit the same morphology with increasing Mach number. For $M = 0.2$, stall begins just before the maximum angle of attack at $\alpha = 19.5°$. As M increases, stall occurs earlier in phase, and the stall characteristic flattens out to resemble the trailing edge stall behavior. The lift and moment stall angle is again considered to be the angle during the upstroke at which the slope of the respective curves changes from the pre-stall to post-stall value. Moment stall precedes lift stall by 0.5° for $M = 0.2$, 1° for $M = 0.4$, and 2° for $M = 0.6$ which is a trend similar to that of $k = 0.025$. Post-stall C_L during the downstroke collapse to approximately 0.65, and peak negative moments are all approximately $C_M = -0.17$ for $k = 0.050$. The reattachment behavior is the same as for $k = 0.025$ as well. The C_L data indicates attached flow C_L beginning at $\alpha = 8°$ for $M = 0.2$, and perhaps slightly later (lower α) for $M = 0.4$ and 0.6. The dynamic reattachment of the higher Mach number cases is more difficult to pinpoint in the C_L behavior because of the attached flow hysteresis. This figure most clearly shows how the C_L disparity between upstroke and downstroke during the attached flow interval is a strong function of freestream Mach number.

Figure 23 shows the hysteresis loops with $k = 0.075$ for $M = 0.2$ and 0.4 only since the maximum attainable reduced frequency is $k = 0.050$ at $M = 0.6$. This is the highest reduced frequency ($k = 0.075$) for which valid comparisons can be made with respect to the effect of freestream Mach number. This figure continues to validate observed trends described for $k = 0.025$ and 0.050. All generic assertions regarding the delayed onset of stall, precedence of

moment stall, modified stall characteristic, post-stall C_L and C_M, and dynamic reattachment are consistent at this reduced frequency.

Figure 24 through Figure 29 present phase-averaged contours of upper surface pressure coefficient for each Mach number (0.2, 0.4, and 0.6) at $k = 0.025$ and 0.050 to illustrate how the pressure development is modified with enhanced compressibility. These figures are formatted in the same way as Figure 11 with chordwise position along the abscissa and phase angle along the ordinate. The contour intervals and colorbars are uniform for ease of comparison. Also, when applicable, a single dark black contour line is plotted demarcating the critical pressure coefficient for a given freestream Mach number (Figure 26 – Figure 29). The critical pressure coefficient corresponds with a local flow speed equal to the speed of sound ($M = 1$). The critical pressure coefficients for $M = 0.2$, 0.4, and 0.6 are $C_{p,cr} = -16.3$, -3.7, and -1.4, respectively. When the local pressure is lower than the critical pressure, the local Mach number over a chordwise extent bounded by this contour is supercritical.

Figure 24 and Figure 25 show C_p contours for $M = 0.2$, $k = 0.025$ and 0.050. In both of these cases, suction develops in the leading edge region attaining a peak $C_p \approx -7$ at $x/c = 0$ while $16° < \alpha < 17°$ during the upstroke just prior to LEV formation. As α continues to increase, the peak suction starts to diminish, the LEV forms, detaches from the leading edge and convects downstream leaving a low pressure trace between $140° < \varphi < 165°$. The trace starts to fade as the vortex convects past $x/c = 0.6$. The LEV passage is immediately succeeded by a plateau of uniform $C_p \approx -1$ until the reattachment process begins. For $k = 0.025$ (Figure 24) pressure starts to decrease first at the leading edge at $\varphi = 250°$ ($\alpha = 14.5°$) and progresses toward the trailing edge until $\varphi = 255°$ ($\alpha = 11°$) when the flow is completely attached. The reattachment process is similar, although delayed for $k = 0.050$.

Figure 26 and Figure 27 show C_p contours for $M = 0.4$, $k = 0.025$ and 0.050. Both cases have a brief instance of supercritical flow. In both cases, the peak $C_p \approx -4$ at $x/c = 0.023$ while $14° < \alpha < 16°$. The depressed C_p signal of the LEV is evident, although like the peak suction, it is weakened relative to the $M = 0.2$ cases.

Figure 28 and Figure 29 show C_p contours for $M = 0.6$, $k = 0.025$ and 0.050. Both reduced frequencies for this Mach number feature significant intervals of supercritical flow extending over the leading 25% of chord. For $k = 0.025$, the peak $C_p \approx -2.5$, and for $k = 0.050$, the peak $C_p \approx -2$. In both cases, before the loss of lift which occurs during the upstroke, peak suction occurs

at x/c = 0.074. Actually, the attached flow pressure distribution near the leading edge is approximated by a plateau with $C_p \approx -2$ increasing slightly from x/c = 0.023 to a maximum at x/c = 0.074. Figure 29 shows supplemental upper surface C_p distributions contrasting two representative phases of supercritical flow for k = 0.050. One of the phases occurs during the upstroke (α = 13°, φ = 113°) and the other occurs during the downstroke (α = 5.5°, φ = 281°). It is surmised that during both the upstroke and downstroke, the supercritical flow is terminated by a normal shock situated on the airfoil surface between $0.07 < x/c < 0.20$ where the adverse pressure gradient is strong. During the upstroke, the shock gradient appears to be less than that which occurs during the downstroke and this is evident by comparing the chordwise extent of the supercritical region in the C_p contour plots for either k = 0.025 or 0.050. In the case of both reduced frequencies suction diminishes along with the size of the supercritical region beginning at $\varphi \approx 130°$ between $15° < \alpha < 17°$. However, this process is much more gradual than the lower Mach number cases and there is no trace of a LEV at any phase. Figure 28 and Figure 29 also clearly show the attached flow hysteresis. For instance, in either case (k = 0.025 or 0.050) α = 8° for φ = 90° and φ = 270°. At φ = 90° the peak C_p is between $-1.6 < C_p < -1.1$, and at φ = 90° the peak C_p is between $-2.3 < C_p < -2$.

3.1.5   A Note Regarding Attached Flow Hysteresis

The attached flow hysteresis is considered regarding whether the attached flow hysteresis is a result of artificial post-processing error or some inadequacy of the experimental methodology. For instance, is it conceivable that the entire phase-average C_p distribution is shifted in phase because of a measurement phase lag which is a function of freestream Mach number and/or static pressure. The following explanation is offered to support the validity of the attached flow hysteresis phenomenon. The low Mach number case is consistent with patterns in historical data, and this would be the case for which maximum signal distortion would be expected. The lift curve collapses for the upstroke and downstroke during the attached flow interval. Furthermore, the lift is a strong function of the integrated pressure distribution, and a weak function of angle of attack, especially where α is as small as it is during this interval ($\alpha < 10°$). Across all three Mach numbers tested, the difference in attached flow lift as a function of α during the upstroke does not exceed 0.1 for any k value. Comparing with the dissimilarities documented above seems to substantiate the claim of attached flow hysteresis that is a strong function of compressibility.

(a)

(b)

Figure 18: *M* = 0.2, *α* ≈ 10° − 10° cos *φ*.
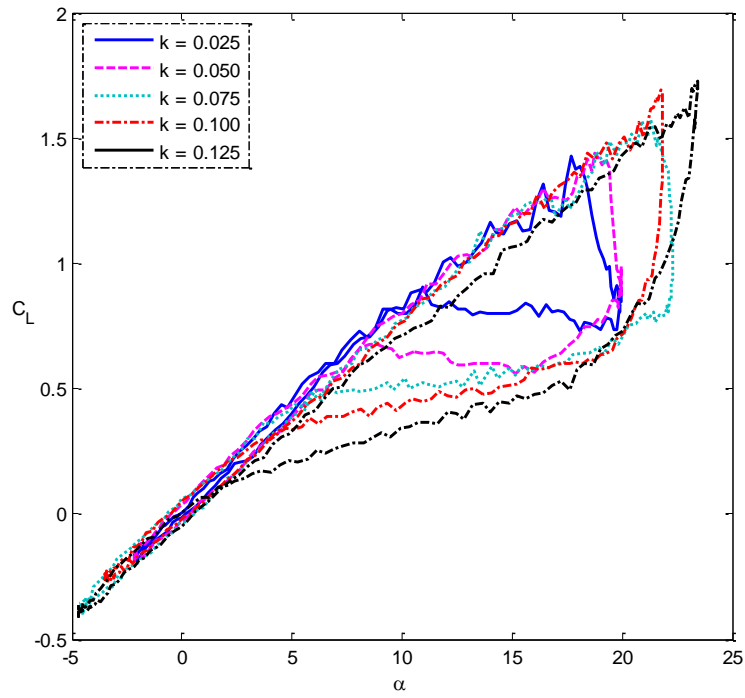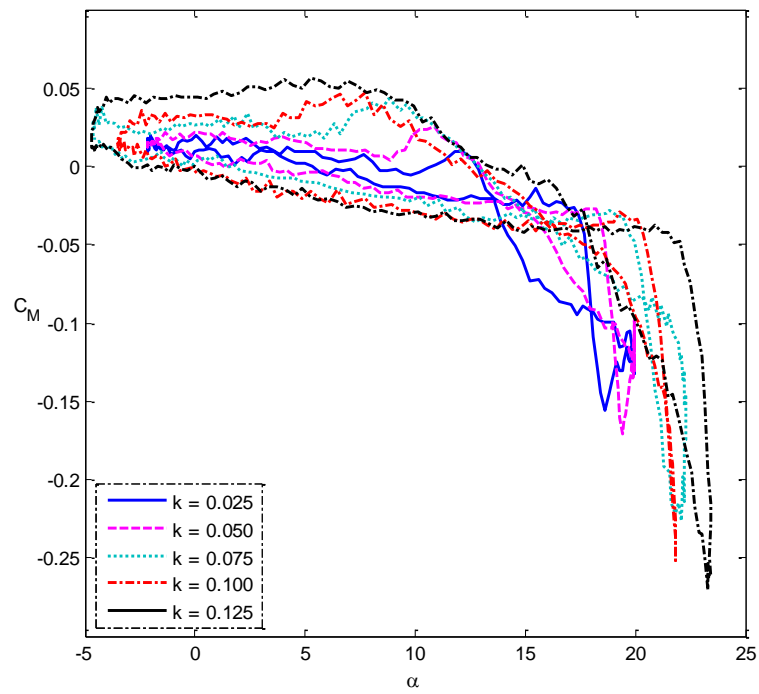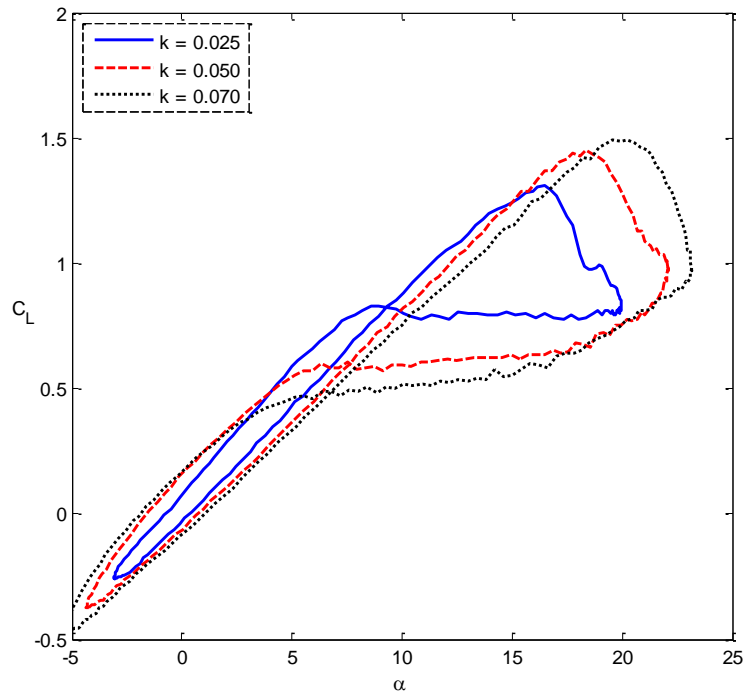
(a)
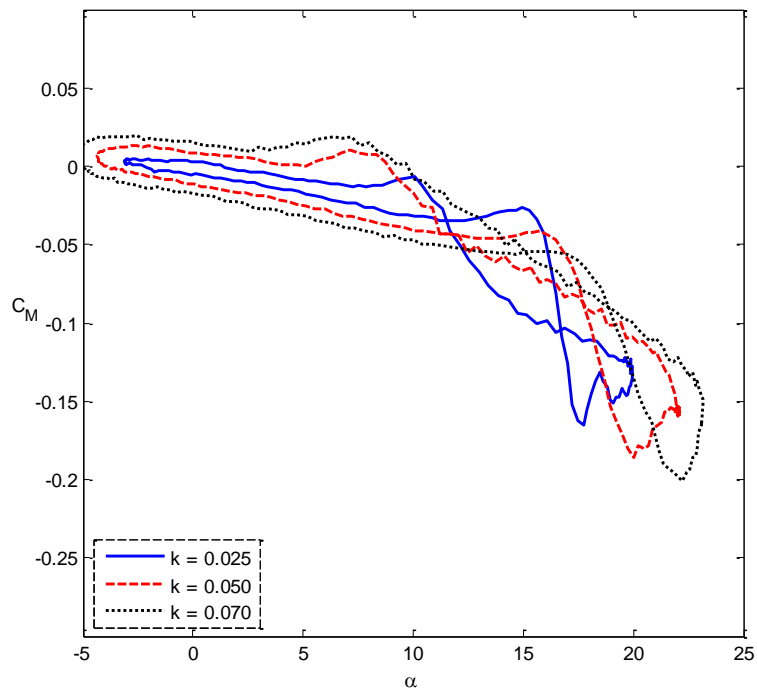
(b)

Figure 19: $M = 0.4$, $\alpha \approx 10° - 10° \cos \varphi$.
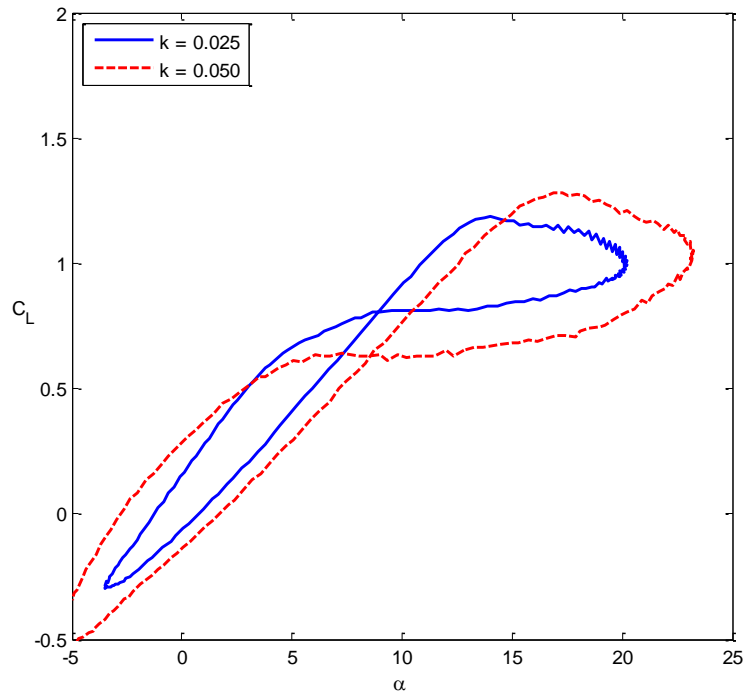
(a)
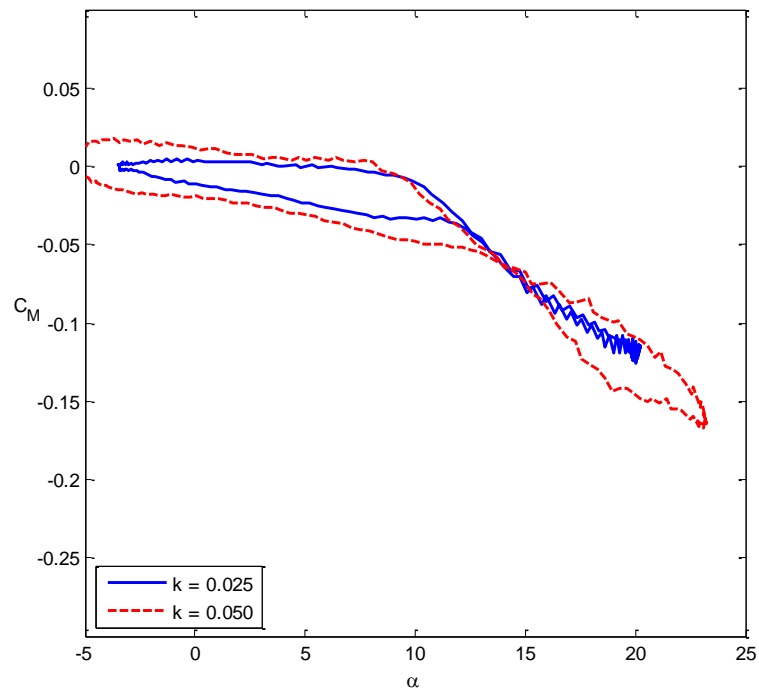
(b)

Figure 20: $M = 0.6$, $\alpha \approx 10° - 10° \cos \varphi$.
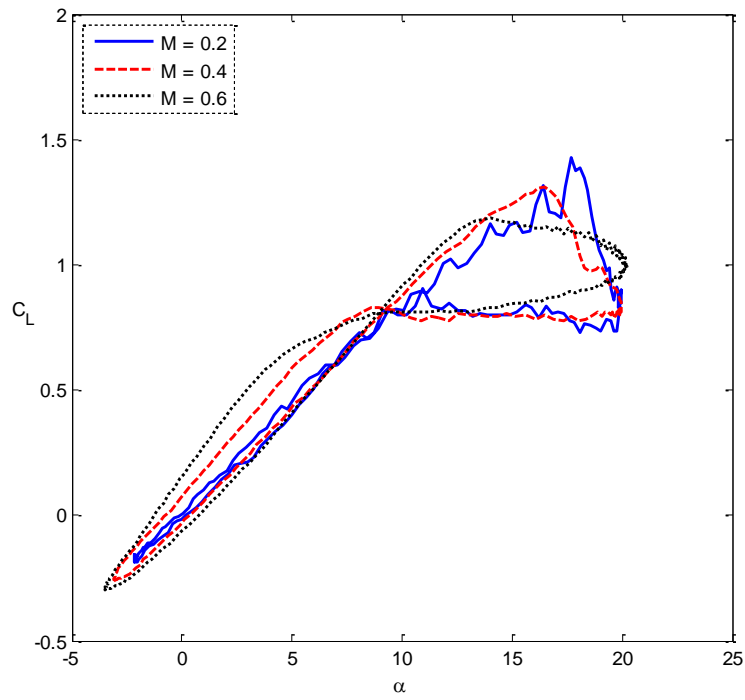
(a)
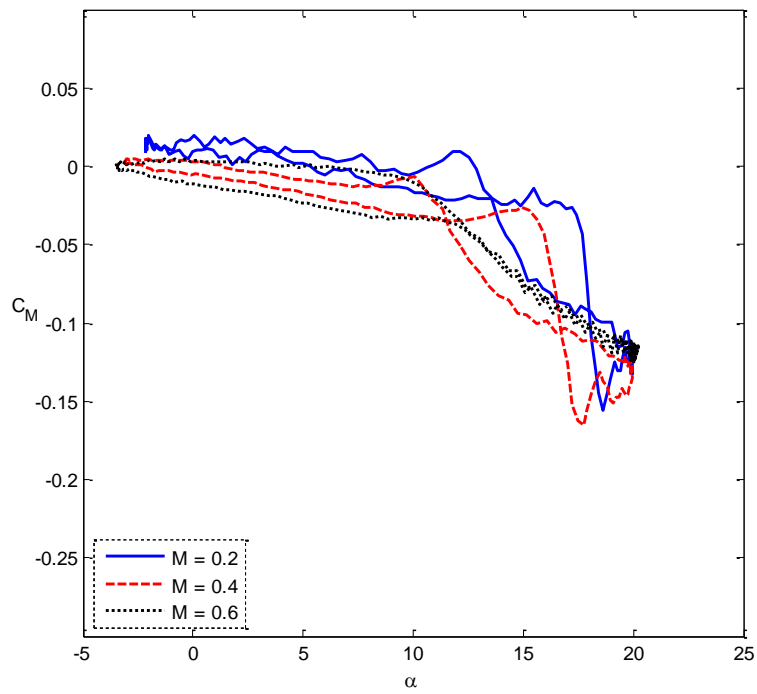
(b)

Figure 21: $\alpha \approx 10° - 10° \cos \varphi$, and $k = 0.025$.
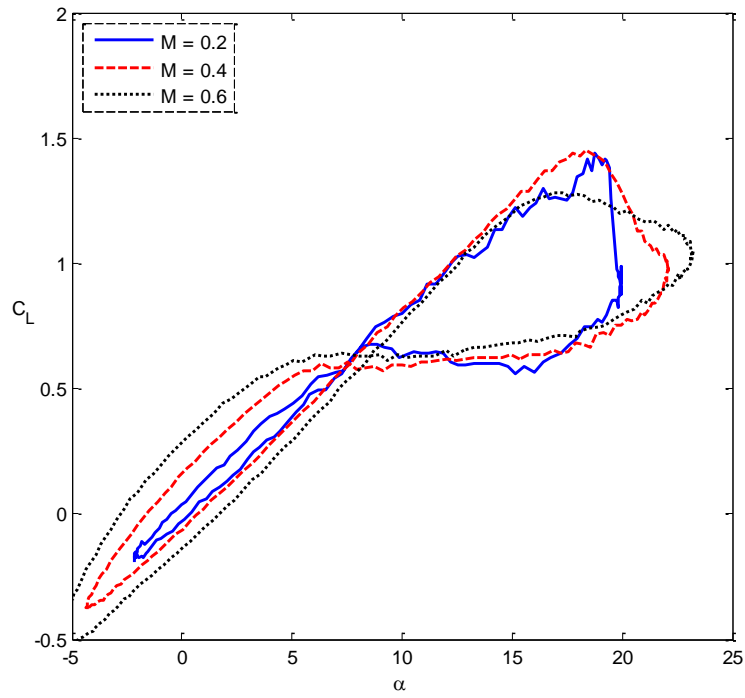
(a)
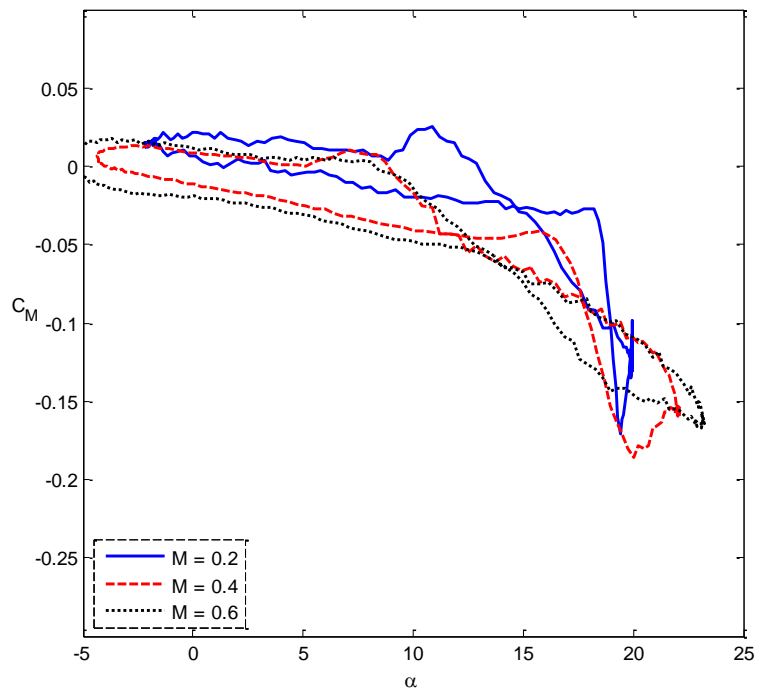
(b)

Figure 22: $\alpha \approx 10° - 10° \cos \varphi$, and $k = 0.050$.
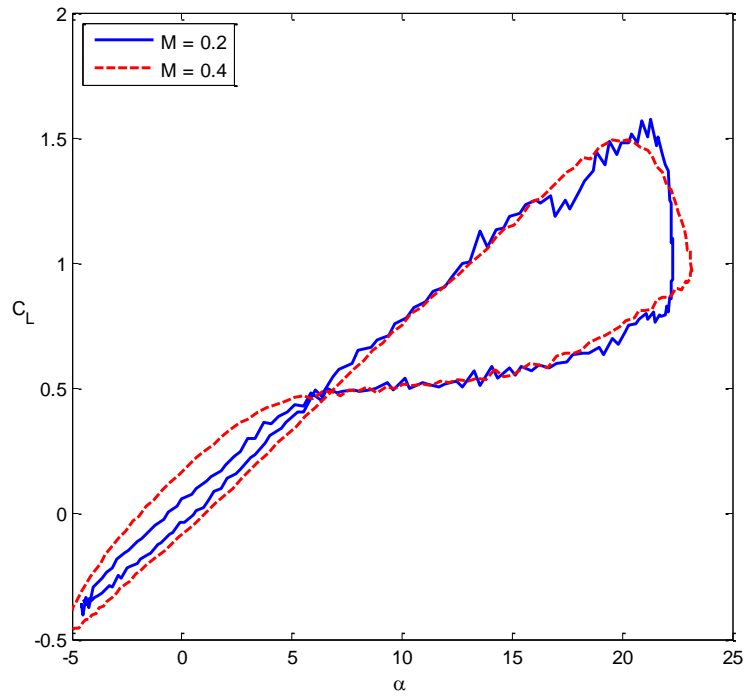
(a)
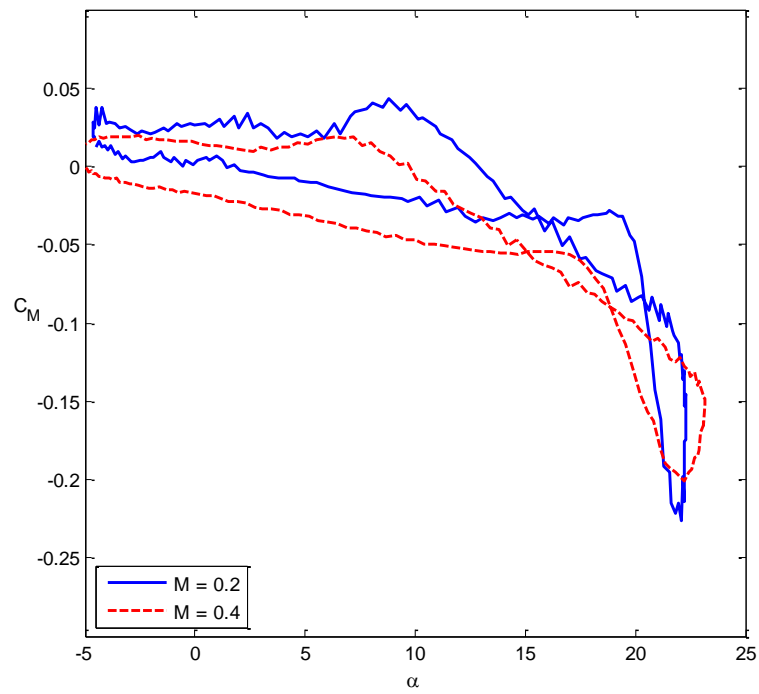
(b)

Figure 23: $\alpha \approx 10° - 10° \cos \varphi$, and $k = 0.075$.
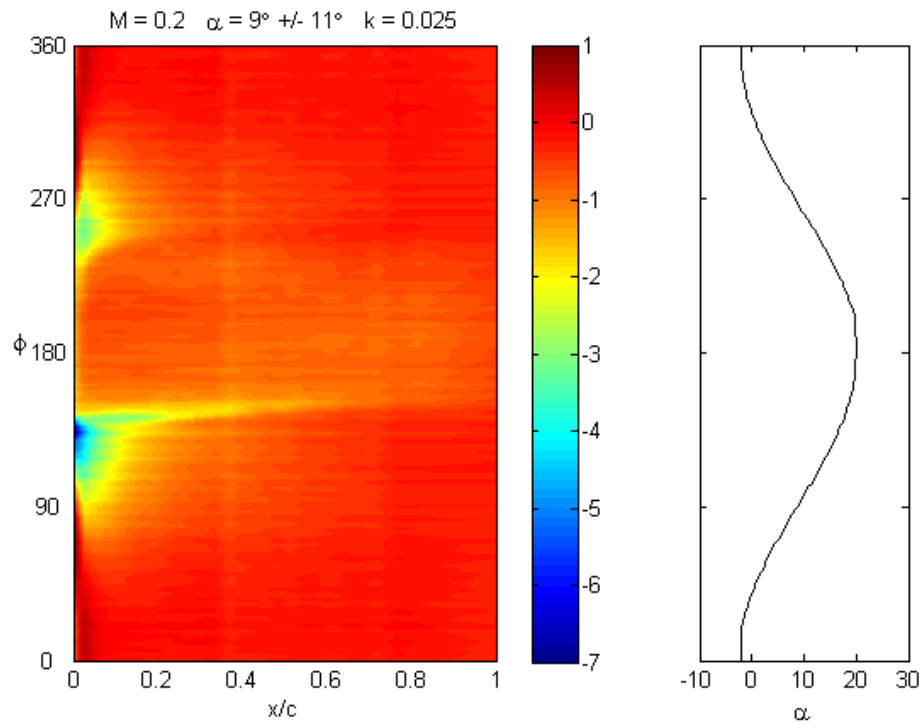
Figure 24: *M* = 0.2, *α* = 9° − 11° cos *φ*, and *k* = 0.025.
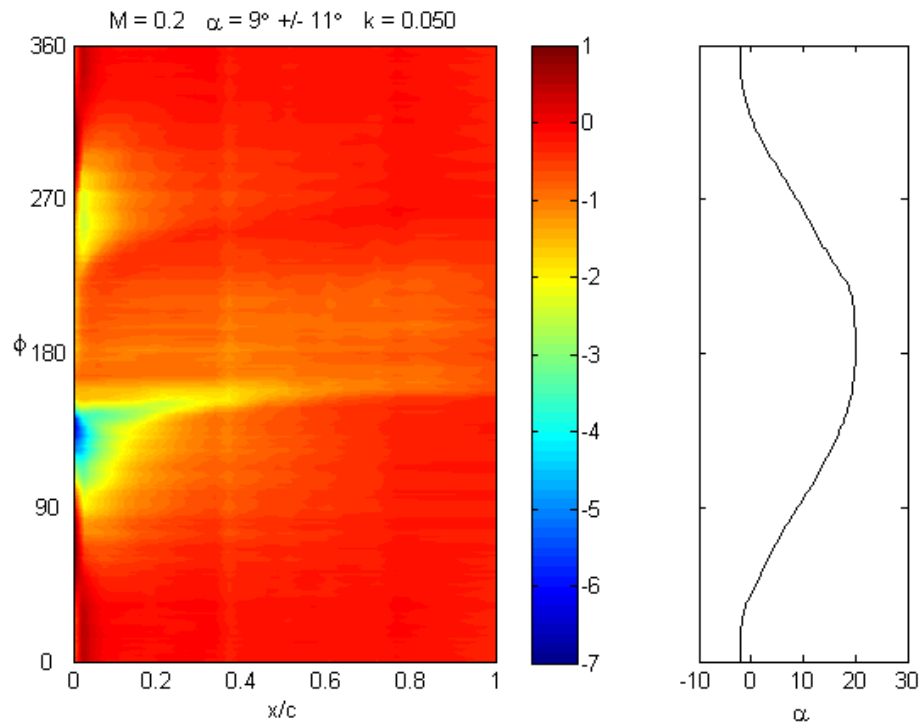
Figure 25: *M* = 0.2, *α* = 9° − 11° cos *φ*, and *k* = 0.050.
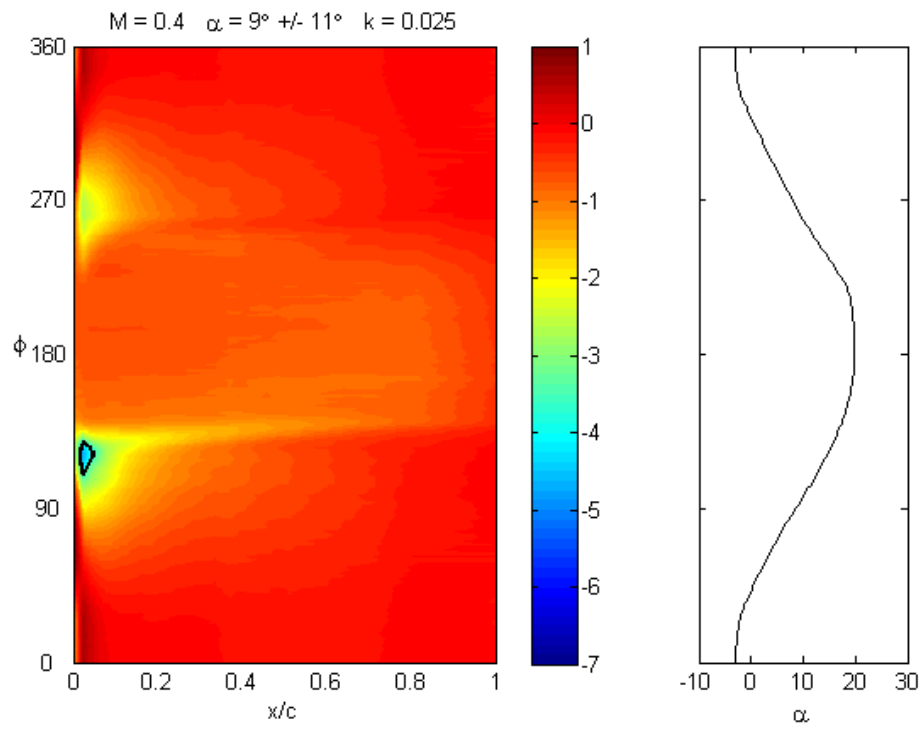
Figure 26: *M* = 0.4, *α* = 9° − 11° cos *φ*, and *k* = 0.025.
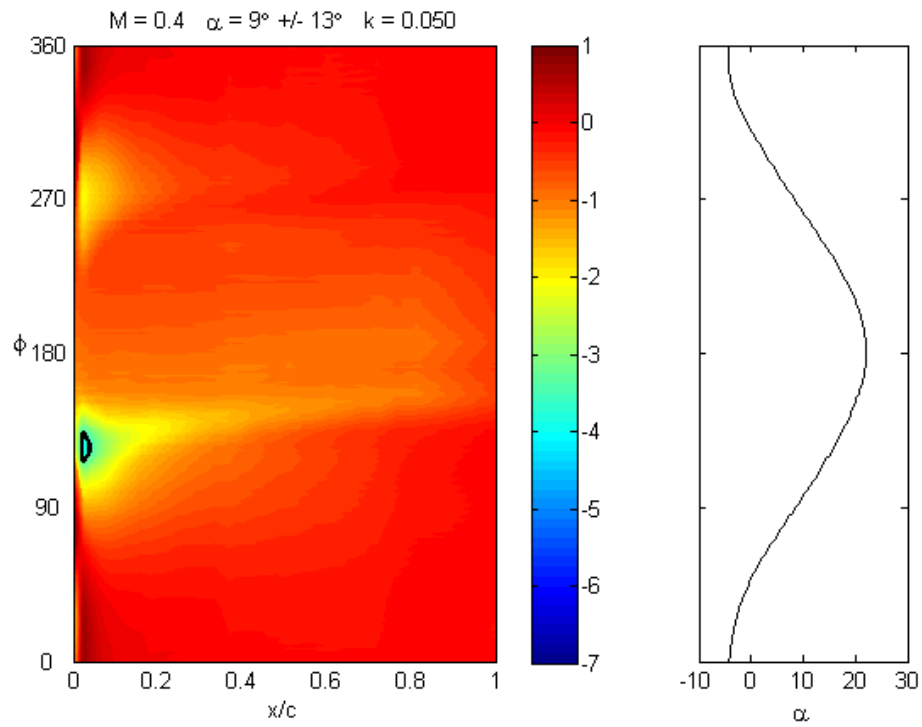
Figure 27: *M* = 0.4, *α* = 9° − 13° cos *φ*, and *k* = 0.050.
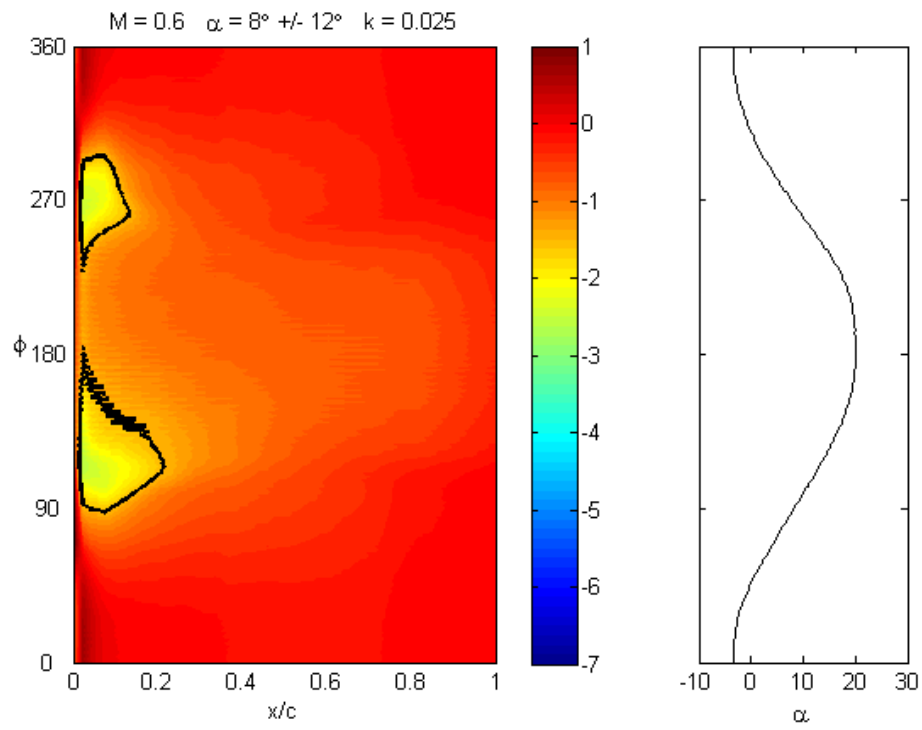
Figure 28: $M = 0.6$, $\alpha = 8° − 12° \cos \varphi$, and $k = 0.025$.
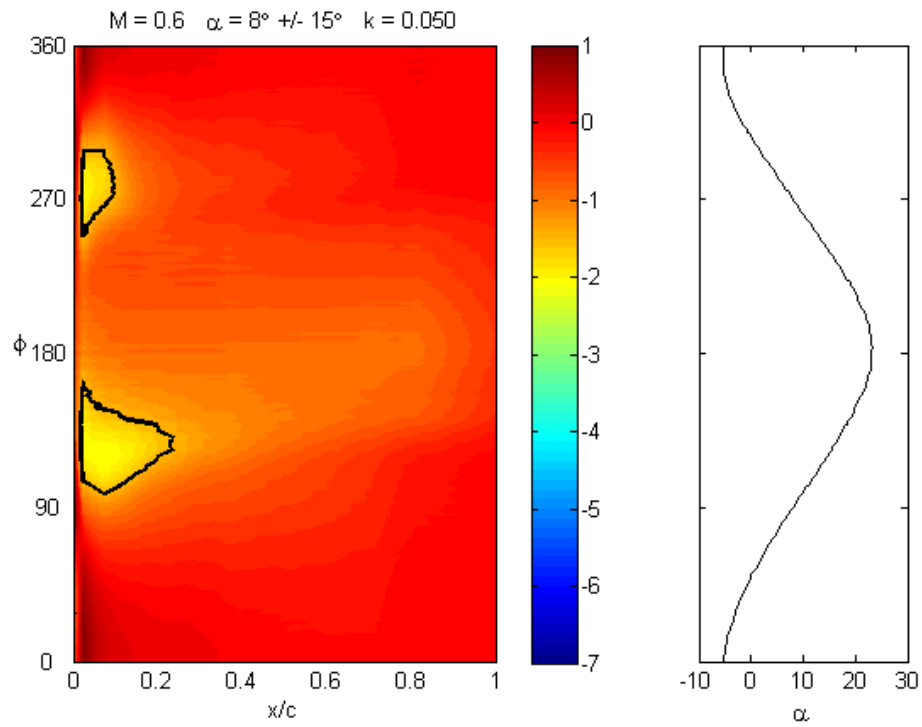
Figure 29: $M = 0.6$, $\alpha = 8° − 15° \cos \varphi$, and $k = 0.050$.

3.2   Mach Oscillations with fixed Angle of Attack

The conventional model for understanding compressible dynamic stall involves studying the coupled fluid and structural dynamics of an airfoil executing a prescribed sinusoidal oscillation of angle of attack in a steady airstream. Elucidating the impact of time-varying compressibility on compressible dynamic stall ultimately requires modeling a sinusoidal airfoil motion which is synchronized with a sinusoidal freestream Mach number oscillation. Understanding the complexity of coupled airfoil and freestream unsteadiness is aided by isolating the effects of each aspect. Therefore, before presenting results with synchronized airfoil pitching motion and freestream Mach number oscillation, this section focuses on a fixed-pitch airfoil subjected to the time-varying airstream condition. The data will show that an important angle of attack is the static stall angle for the time-mean Mach number. For a steady flow Mach number of 0.4, the static stall angle of attack is measured to be $14° < \alpha_{ss} < 15°$ using the clean SSC-A09 model in the 6" × 22" transonic wind tunnel. Oscillating airstream data were acquired for fixed airfoil incidence angles ranging from pre-static-stall α to post-static-stall α to identify the effects of the time-varying freestream with respect to the static stall angle for the mean Mach number of 0.4. The set of angles tested includes $\alpha = 10°$, 13°, 14°, 15°, 16°, and 18°. Given the maximum Mach number oscillation frequency of 17 Hz, unsteady testing was performed for reduced frequencies of $k = 0.0125$, 0.0250, and 0.0500. Phase-averaged lift and moment coefficient measurements are presented along with selected C_p contour plots in order to illustrate the impact of freestream modulation on airfoil performance.

Figure 30 and Figure 31 combine angle of attack, oscillating Mach number, reduced frequency, and phase-averaged performance metric information to present representative cases with respect to the static stall angle for $M = 0.4$. In both figures, α is plotted along the x-axis and M is plotted along the y-axis. C_L is plotted along the z-axis in Figure 30, and C_M is plotted along the z-axis in Figure 31. The four incidence angles represented are $\alpha = 10°$, 13°, 15°, and 18°. Curves are color-coded for reduced frequency with red curves corresponding to $k = 0.025$ and black curves corresponding to $k = 0.050$. Arrows are added to the curves to show the direction of increasing phase angle. The flow is decelerating from maximum to minimum M for $0° < \varphi < 180°$ and accelerating to maximum M for $180° < \varphi < 360°$. The Mach number waveform ($M = 0.4 + 0.07 \cos \varphi$) is presented as a function of phase in subsequent figures and will be discussed in more detail later.

Both figures show that the hysteretic behavior, which depends on freestream acceleration, is transformed as α is swept through the static stall angle for $M = 0.4$. Generally, both C_L and C_M tend to oscillate about the steady flow values and both are measured to be greater while the freestream is decelerating than while accelerating. Especially for $\alpha < \alpha_{ss}$, the hysteresis is exaggerated by increasing the acceleration magnitudes which are proportional to reduced frequency. Also, unsteadiness becomes strong enough for $\alpha > \alpha_{ss}$ to be evident in the phase-averaged orbits. Looking specifically at the C_L behavior in Figure 30, hysteresis is biased toward the minimum Mach number where the C_L disparity is greatest. For $\alpha = 15°$, the performance is straddling the stall boundary. Thus the unsteadiness is elevated, and the performance toggles between pre-stall values at low M and post-stall values at high M. This will be discussed in more detail later. For $\alpha = 18°$, the performance oscillates about the post-static-stall value, and the hysteresis is still comparable to pre-stall ($\alpha = 13°$) though not as clearly a strong function of reduced frequency. The C_M behavior portrayed in Figure 31 shows that the C_M hysteresis is greatest for $\alpha = 15°$ where the performance straddles the stall boundary, and it is again biased toward the minimum Mach number. Pre-stall hysteresis is evident, but relatively weak, and post-stall hysteresis appears to be negligible.
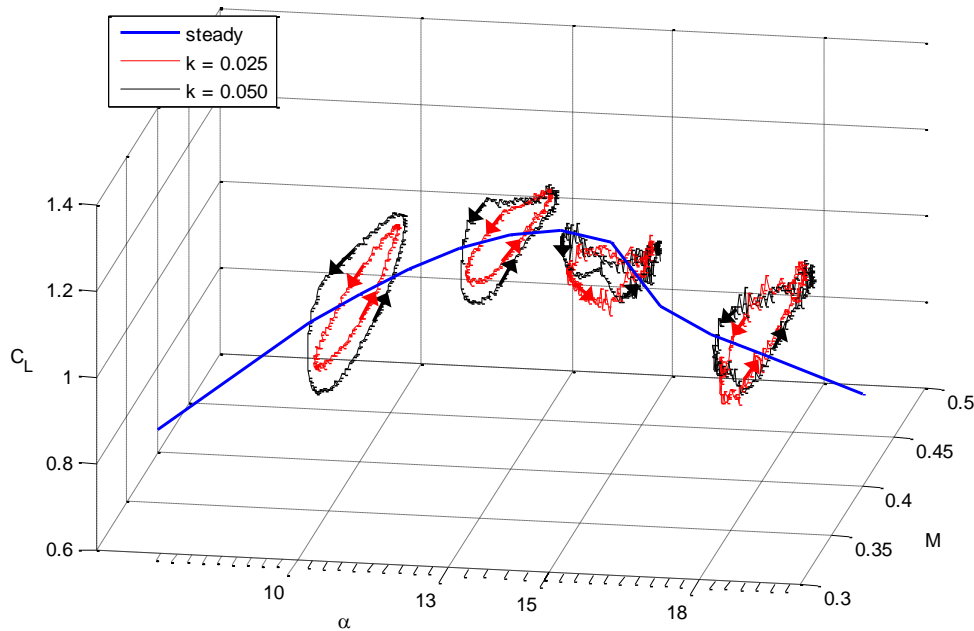
Figure 30: C_L vs. α vs. M for representative cases of fixed alpha and oscillating airstream.
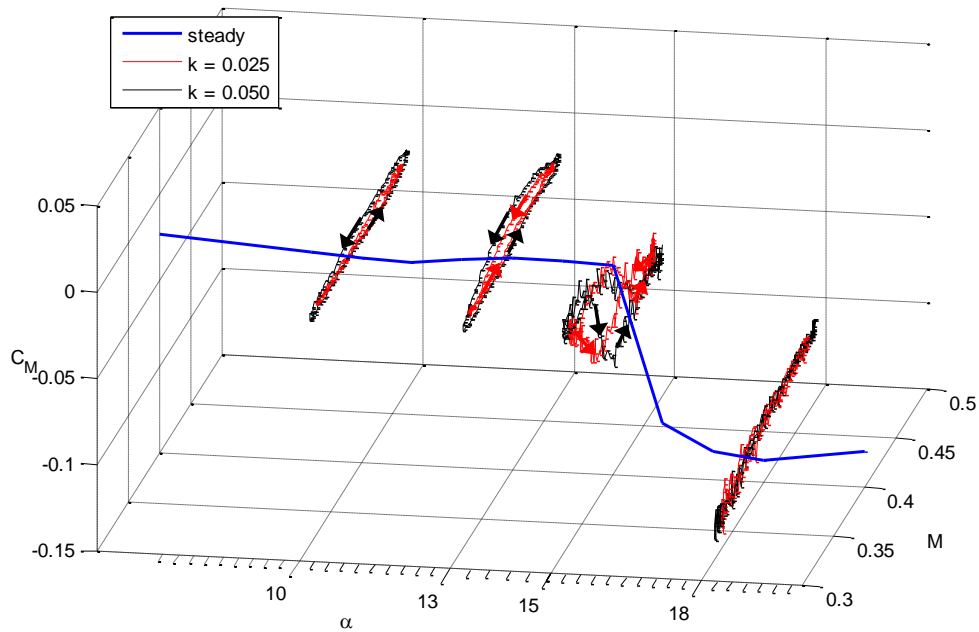
Figure 31: C_M vs. α vs. M for representative cases of fixed alpha and oscillating airstream.

Figure 32 and Figure 33 present representative phase-average contours of the upper surface C_p distribution in a format similar to plots presented in previous sections. Chordwise position is plotted along the abscissa and phase angle along the ordinate. The phase-averaged Mach number is plotted to the right with Mach number along the abscissa and phase angle along the ordinate. As mentioned earlier, the phase angle is ordered such that the freestream flow is decelerating for $0° < \varphi < 180°$ and accelerating for $180° < \varphi < 360°$. The contour levels and colorbars are consistent between these two figures for ease of comparison. Figure 32 presents results for a selected pre-stall angle of attack, $\alpha = 14°$, with $k = 0.025$. Figure 33 presents a data point for which the performance straddles the static stall boundary ($\alpha = 15°$) and $k = 0.025$. Although the surface pressures do fluctuate slightly for post-stall α, the upper surface C_p distribution plateaus across the chord at approximately $C_p \approx -1$ indicating an open separation.
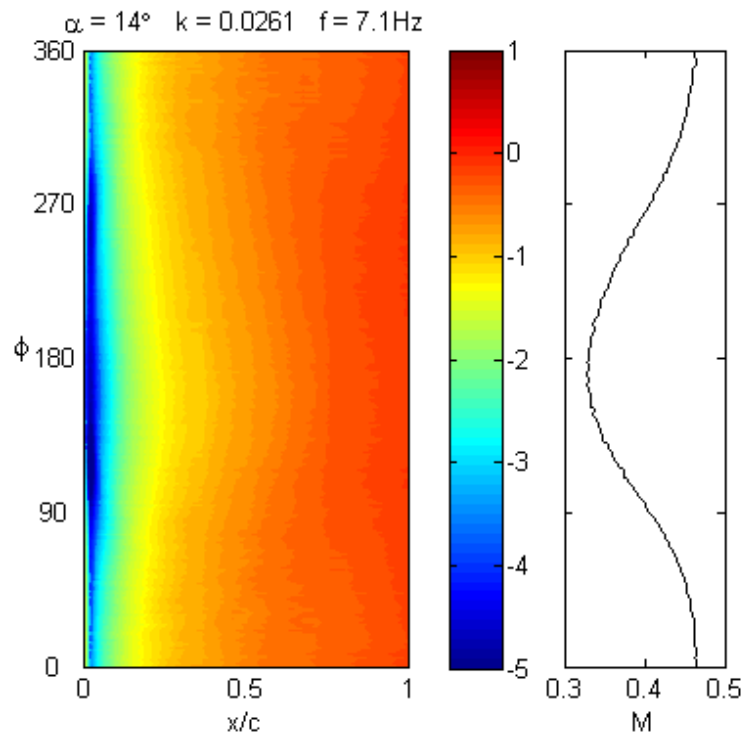
Figure 32: Contours of upper surface C_p for $\alpha = 14°$, $M = 0.4 \pm 0.07$, and $k = 0.025$.
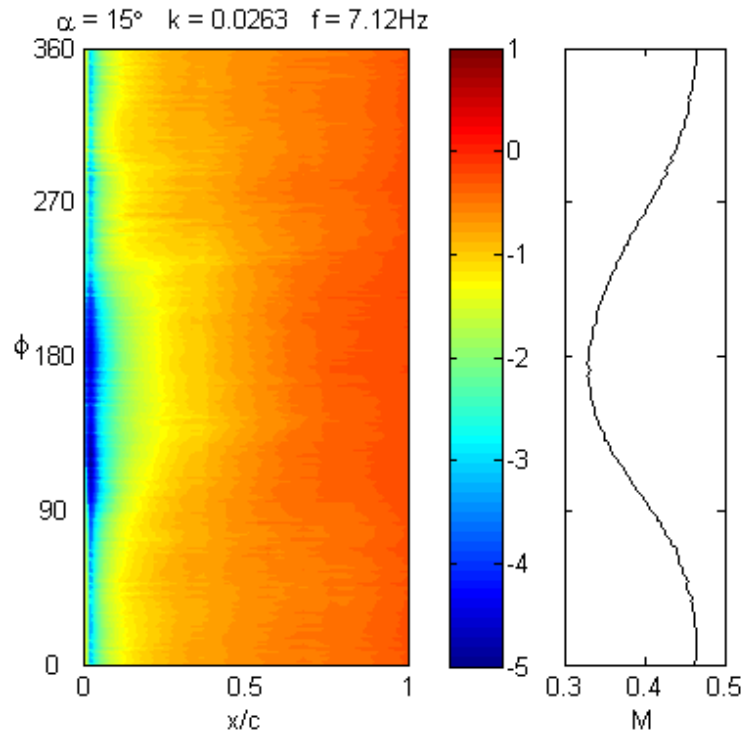
Figure 33: Contours of upper surface C_p for $\alpha = 15°$, $M = 0.4 \pm 0.07$, and $k = 0.025$.

The pattern displayed in Figure 32 for $\alpha = 14°$ is typical for pre-stall α in the sense that the greatest suction peak is measured to be approximately $C_p \approx -5.5$ at $x/c = 0.023$ during the deceleration interval between $90° < \varphi < 180°$. The maximum magnitude of freestream deceleration occurs at approximately $\varphi \approx 90°$. As the flow accelerates, peak suction decreases as do C_L and C_M. This angle of attack ($\alpha = 14°$) was also selected because it shows the signs of unsteadiness surviving the averaging process as Mach number approaches the maximum value. Specifically, when unsteadiness signals through the averaging process it produces striations in the contours which stretch along chordwise direction and fluctuate in phase.

As α increases to 15°, the unsteadiness is amplified producing the wavy contours in Figure 33. Similar to pre-stall α, maximum suction develops near the leading edge during the deceleration interval. However, unlike the gradual loss of suction observed during the acceleration interval for pre-stall α, acceleration at $\alpha = 15°$ causes the suction peak to decrease suddenly at $\varphi = 235°$, when $M \approx 0.36$ followed by fluctuating pressure distribution near the leading edge.

The airfoil response to freestream modulation for the tested range of α at $k = 0.025$ is condensed further in Figure 34. Four plots are stacked so that the phase correlation can be easily interpreted. The lowest plot is phase-averaged Mach number versus phase angle. Above Mach number, are C_M and C_L. Finally, the uppermost figure shows the phase-averaged C_p measured by the upper surface pressure tap located at $x/c = 0.074$. The C_p curves show generally lower pressures during deceleration. As α increases from 10° to 13° there is a bulk negative shift in suction and a positive shift in lift which is expected for pre-stall alpha. As α increases from 13° to 14°, suction and lift are approximately the same for $M < 0.42$, but decreased for $M > 0.42$. This trend continues for α increased to 15° as the decrease in suction and lift is even more dramatic for $M > 0.4$ ($0° < \varphi < 90°$ and $225° < \varphi < 360°$). Furthermore, the evidence of unsteadiness is pronounced while $M > 0.4$. For post-stall α, the 1/period pressure fluctuations are reduced and unsteadiness persists. The C_M behavior is readily divided into the three distinct categories of pre-stall, stall, and post-stall angles. For $\alpha < \alpha_{ss}$, C_M is approximately -0.01 with relatively small 1/period fluctuation. For $\alpha > \alpha_{ss}$, C_M is approximately equal to the post-static stall value. The moment coefficient is approximately -0.09 for $\alpha = 16°$ and $C_M \approx -0.11$ for $\alpha = 18°$. As with the pre-stall α, the 1/period fluctuations are negligible. The most dramatic 1/period

fluctuations of C_p, C_L and C_M are measured for $\alpha = 15°$ when Mach number crosses 0.4 (either accelerating or decelerating) as the airfoil performance straddles the stall boundary.
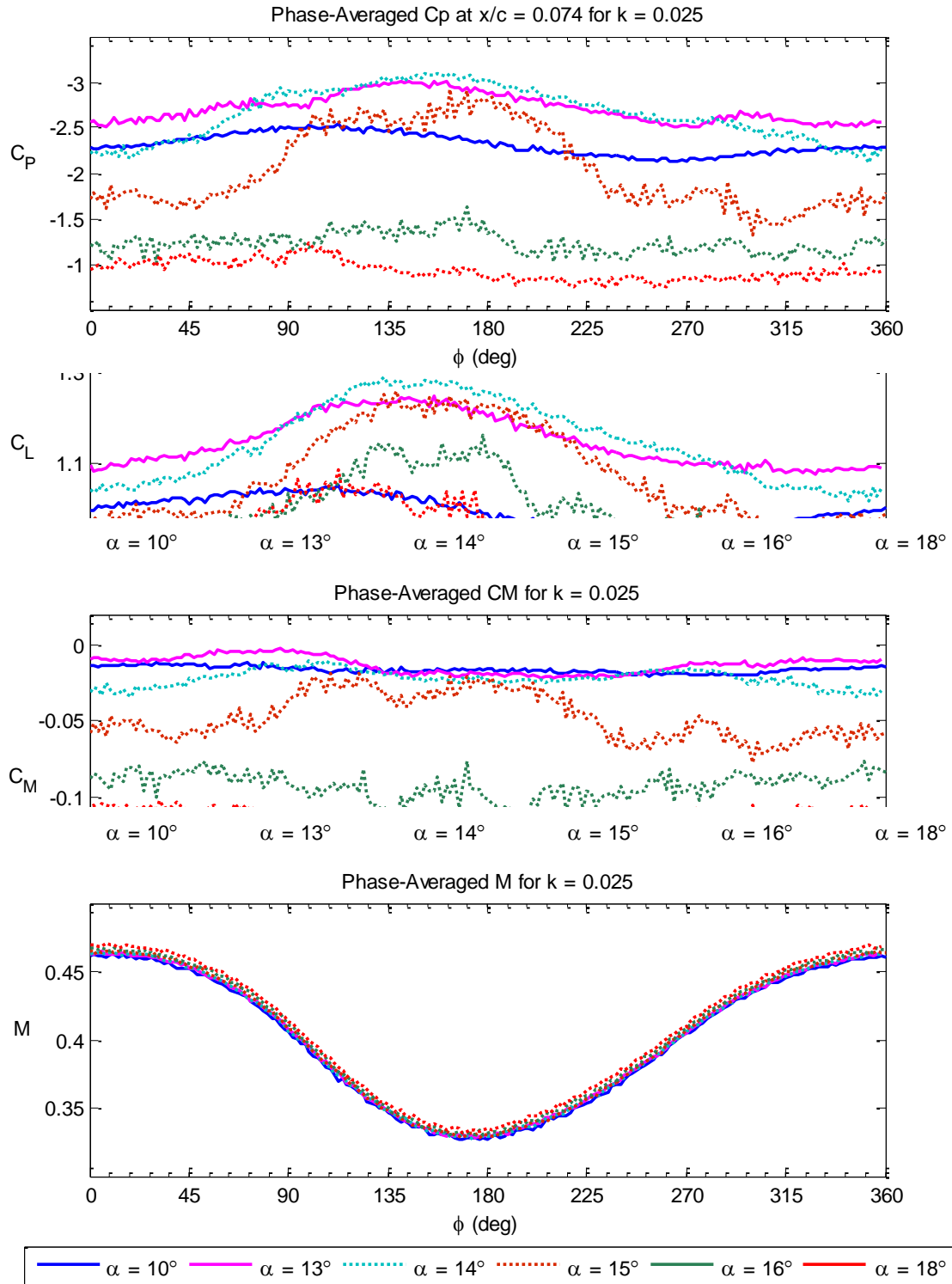
Figure 34: Phase-averaged C_p traces ($x/c = 0.074$), C_L, C_M, and M vs. phase angle for $M = 0.4 \pm 0.07$ and $k = 0.025$ and representative α.

The fluctuating performance metrics are quantified in Figure 35, where the time-averaged C_L and C_M are plotted with the steady $M = 0.4$ clean airfoil results. Error bars are used to indicate the range of measured C_L and C_M values for each reduced frequency ($k = 0.0250$ and 0.0500). For each fixed k value, the C_L range function is similar pre-stall and post-stall α. The maximum range occurs at fixed α within the stall characteristic. The range widens as reduced frequency increases, and the upper bound which is generally measured during deceleration, is modified the most. The C_M range is smallest for pre-stall α. When α straddles the static stall boundary with $\alpha = 15°$ the phase-averaged C_M range is maximum at $\Delta C_M \approx 0.05$ for $k = 0.025$ and $\Delta C_M \approx 0.072$ for $k = 0.050$. This is because the pressure distribution is toggling between conditions of attached and separated flow near the leading edge producing large variations in pitching moment at this angle.

(a)

(b)
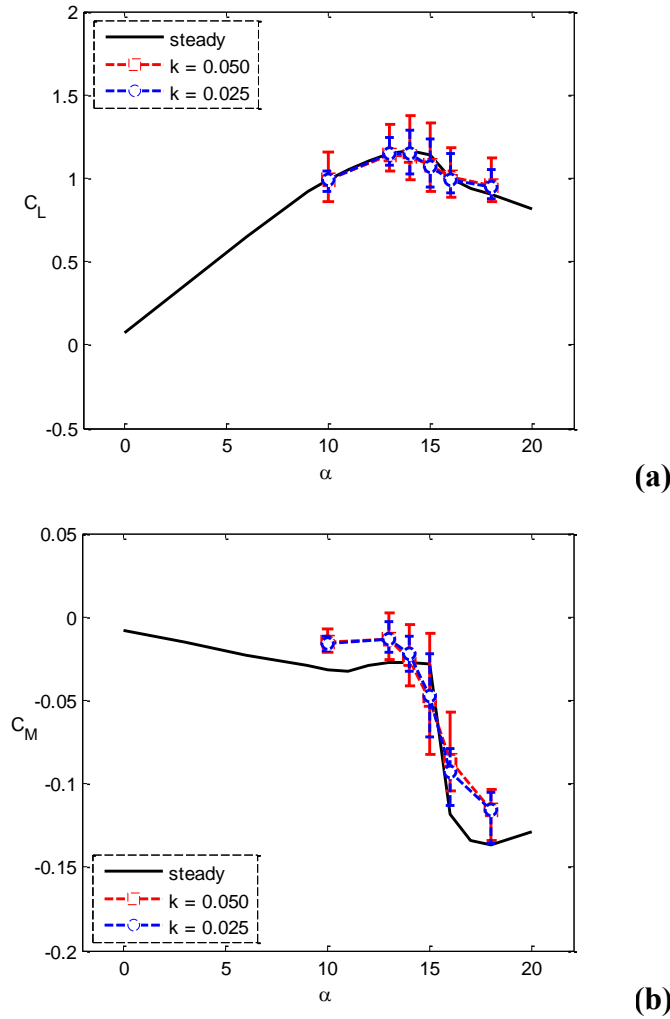
Figure 35: Comparison of range of measured (a) C_L and (b) C_M for fixed α and $M \approx 0.4 \pm 0.07$ and varied reduced frequency; steady $M = 0.4$ results also shown.

3.3   Coupled Pitch and Mach Oscillations

The final stage of experiments performed with the clean SSC-A09 model is that of airfoil pitching motion synchronized with freestream oscillation to elucidate the impact of the time-varying compressibility condition on compressible dynamic stall. All of the results presented for an oscillating airfoil in a steady airstream were intended to simulate the dynamic stall experienced by an airfoil executing a sinusoidal pitch oscillation with angle of attack approximated by $\alpha = 8.5° - 11.5° \cos \varphi$. All of the results presented for a fixed pitch airfoil were subjected to a Mach number oscillation approximated by $M = 0.4 + 0.08 \cos \varphi$. By this definition of the phase angle, φ, the maximum angle of attack and maximum Mach number are 180° out of phase. Figure 36 depicts the scenario for which this phase angle convention is defined. A rotorcraft is considered to be flying in straight forward flight, such that the relative velocity seen by an airfoil section on the advancing blade is augmented by the forward flight speed, and the relative velocity seen by the retreating blade is reduced. The azimuthal coordinate is selected so that $\varphi = 0°$ corresponds to the blade's position where the relative Mach number is maximum, and $\varphi = 180°$ corresponds the minimum relative Mach number. A phase shift ($\Delta\varphi$) between the pitch oscillation and Mach number oscillation is defined such that $\Delta\varphi = 0°$ describes the condition wherein the minimum angle of attack coincides with the maximum relative Mach number and vice versa. Generally, this was the targeted phase relationship for the coupled oscillation experiments. However, obtaining the desired phasing during testing proved challenging. As outlined in Section 2.4, the servo motor driving the Mach number oscillation assembly is enslaved to follow the spindle assembly of the pitch oscillation device. The phasing is adjusted prior to testing with both units unpowered. The phase shift between the test-section Mach number waveform and the choke vane position is known from empty-tunnel tests (see Gompertz *et al.* 2011), and this information was used to inform the pre-test phasing adjustment. Still, the target phasing was rarely achieved, and more development is required to improve the precision of this aspect of synchronization.

In addition to test points acquired while targeting $\Delta\varphi = 0°$, $\Delta\varphi$ was also deliberately set to a wider range of values to understand the sensitivity to and impact of this variable. Figure 37 illustrates how the pitch and Mach number oscillations are aligned and how the sign of the phase shift is defined. Three angle of attack profiles are shown (red curves) along with one Mach number waveform (black curve). The α curve for $\Delta\varphi = 0°$ depicts the nominal condition. The

phase shift is defined to be positive when the airfoil oscillation is leading the relative Mach number oscillation. For instance, the maximum α leads the minimum Mach number. Conversely, $\Delta\varphi < 0$ when the airfoil oscillation lags the relative Mach number oscillation. While this figure is useful when explaining how phasing is defined for the results which follow, presenting phase-averaged C_p contours in this frame of reference may not be intuitive. Instead, for the purpose of producing plots which are of consistent formation and easy to interpret a phase shift is applied to align the pitch oscillation with $\alpha = \alpha_0 - \alpha_1 \cos\varphi$. The same shift is applied to the measured Mach number oscillation, so the sign convention for $\Delta\varphi$ has the same meaning.
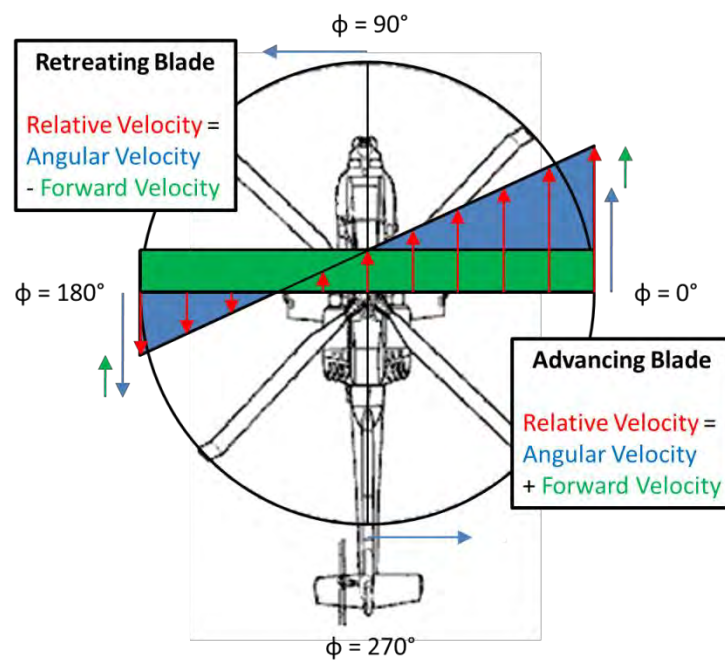
Figure 36: Diagram of rotor disc, relative velocity, and adopted phase angle convention.
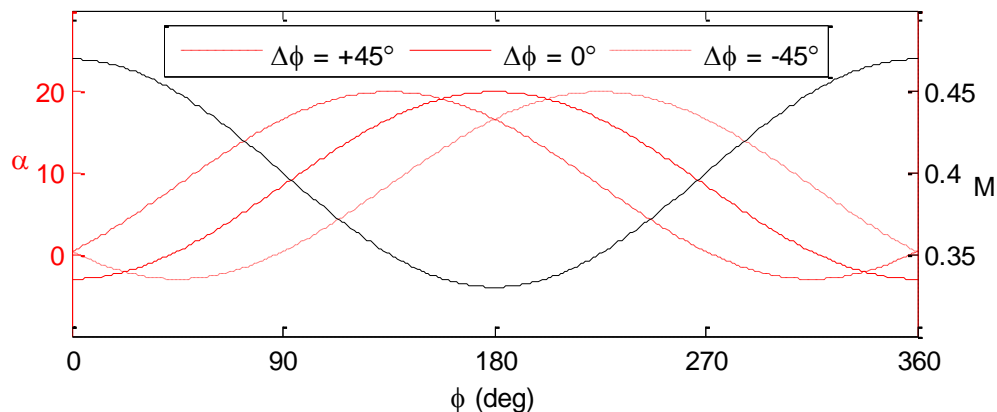
Figure 37: Example phasing of synchronous sinusoidal α (red) and M (black) oscillations.

Coupled oscillation testing was performed for a prescribed $\alpha = 8.5° \pm 11.5°$ and $M = 0.4 \pm 0.08$. Three reduced frequencies were tested including $k = 0.0125$, 0.0250, and 0.0500. Lift and moment coefficient orbits are compiled for each frequency in Figure 38, Figure 40, and Figure 43. Corresponding phase-averaged upper surface C_p contours are presented for $k = 0.0125$, 0.0250, and 0.050 in Figure 39, Figure 41, and Figure 44, respectively. Pressure coefficient contours are formatted consistently throughout this document, and all contour levels and colorbars are consistent within this section. In some cases, data are available for numerous phase relationships, and representative cases are selected for presentation to avoid clutter. On the right-hand-side of each of these figures is a double axis plot which shows the phase alignment between the pitch oscillation profile (dashed red line) and the Mach number oscillation for each of the selected cases with color-coding to match the curves in C_L and C_M plots.

Hysteresis loops are presented for the lowest frequency ($k = 0.0125$) in Figure 38. Comparable dynamic stall data for the pitching airfoil in a steady $M = 0.4$ airstream is not available for this reduced frequency. One of the three cases presented is a close match with the targeted phase relationship with the airfoil oscillation lagging the freestream oscillation by $\Delta\varphi = -7.5°$. In another case, α lags M by $\Delta\varphi = -26.5°$. In the third case, α leads M by $\Delta\varphi = +127.3°$. In the first two cases for which α lags M, the freestream deceleration occurs during the upstroke, and the freestream accelerates during the downstream. The dynamic stall and reattachment processes for these two cases are very similar with $C_{Lmax} \approx 1.4$ and stall onset at $\alpha = 16.5°$ during the upstroke, and reattachment evident at $\alpha = 10°$. Moreover, the difference in moment stall behavior is negligible. Moment stall occurs at $\alpha = 16.5°$ as well, and the peak nose down moments are equal at $C_M = -0.14$. The similarity between these two cases despite the 20° difference in phase lag speaks to the sensitivity of the dynamic stall process to the precise phase relationship between the synchronized pitch and freestream oscillations. These cases show that for $k = 0.0125$, the inability to match the targeted phase relationship does not invalidate the results. The phasing represented by the third case is not merely academic in nature. Such a phase relationship might provide insight into the physics of a maneuvering rotorcraft. In the case where maximum α occurs near the peak relative Mach number, more lift may be generated by the advancing blade causing the rotorcraft to bank left. In this third case, the freestream is accelerating during most of the upstroke, and decelerating during the downstroke. Also, α peaks when M is nearly maximum. The resulting dynamic stall is in stark contrast with the first two

lagging cases. The peak C_L is decreased by approximately 15%, the stall characteristic indicates a much more gradual loss of lift beginning at a lower α during the upstroke. The lift-curve departs from the attached flow trajectory at $\alpha = 13°$, flattens out, and lift starts to decrease at $\alpha = 15.5°$ with a shallow slope compared to the first two cases. Post-stall lift is marginally higher than the measurements for the first two cases. Moment stall occurs at $\alpha = 15.5°$, and the moment stall characteristic is parallel to those of the first two cases. In fact, all three cases exhibit equal magnitudes of maximum nose down moment. The C_p contours corresponding to these $k = 0.0125$ cases are presented in Figure 39. The first two lagging cases are virtually the same with the prominent depression signal of the leading edge vortex at $\varphi \approx 135°$. The LEV signature is less discernable in the third case ($\Delta\varphi = +127.3°$). Also, the post stall C_p plateaus at a slightly lower pressure coefficient in accord with the greater post-stall C_L observed for this case.

There are two important factors at play, and it is difficult to identify the role of each at this stage. One factor is compressibility. The fact that for $\alpha > 10°$ compressibility effects are lessened for the first two cases and greater for the third cases can explain disparate lift generation. The second factor is the impact of freestream acceleration on the hysteresis as in the manner observed for the fixed-pitch airfoil in the oscillating airstream (Section 3.2). Although the acceleration magnitudes are a relative minimum for the freestream oscillation at this reduced frequency, the evidence of lift enhancement in the first two cases is consistent with that observed for a fixed pitch airfoil subjected to a decelerating freestream. The post stall lift is slightly higher during the downstroke, and this is likely to be a freestream deceleration effect. It was shown in Section 3.1 that for all reduced frequencies, the post-stall lift coefficient collapsed for the airfoil oscillating in pitch in a steady airstream with $M = 0.2, 0.4, 0.6$. Thus, the discrepancy in post-stall lift is not attributed to the instantaneous freestream Mach number. Furthermore, results for the fixed-pitch airfoil subjected to freestream oscillation indicate that significant C_L hysteresis is observed even for post-stall conditions.
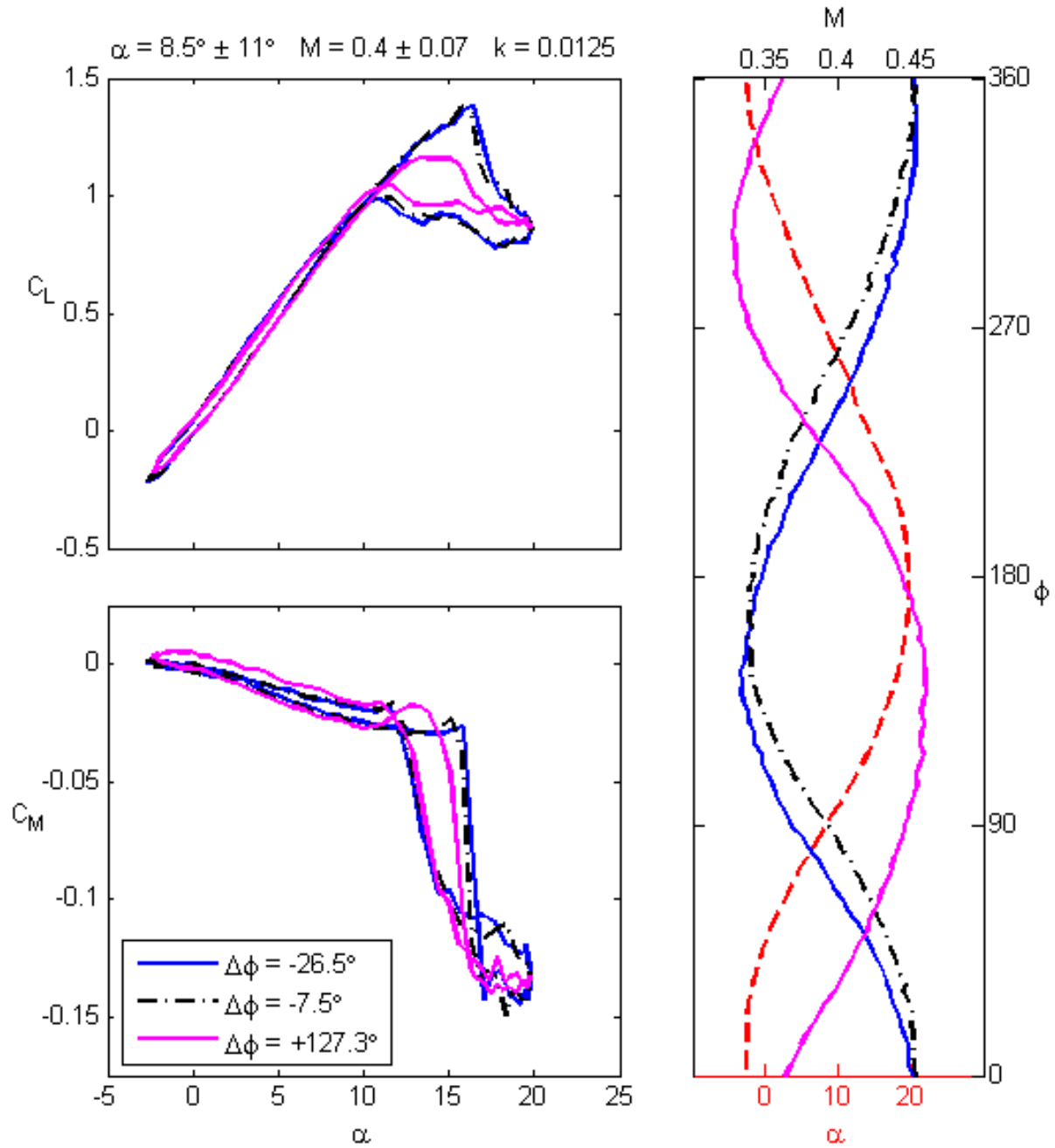
Figure 38: C_L and C_M orbits for $α = 8.5° ± 11°$, $M = 0.4 ± 0.07$, $k = 0.0125$, and representative phasing between synchronous oscillations.
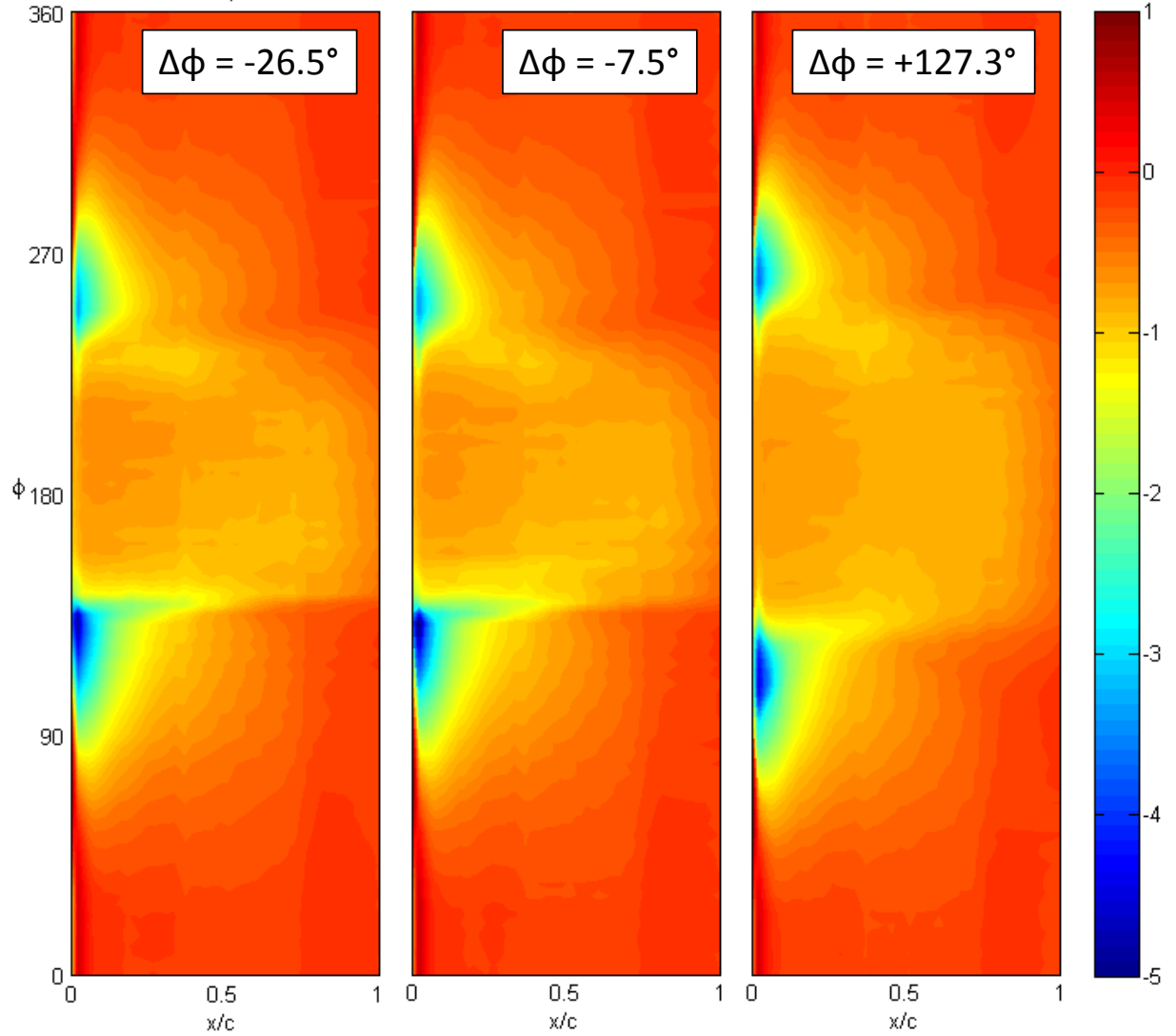
Figure 39: C_p contours for $\alpha = 8.5° \pm 11°$, $M = 0.4 \pm 0.07$, $k = 0.0125$, and representative phasing between synchronous oscillations.

Figure 40 displays the C_L and C_M orbits for test points with representative phasing and $k = 0.0250$. Each plot also includes comparable dynamic stall data for $k = 0.0250$ and the identical airfoil pitch oscillation profile in a steady $M = 0.4$ airstream (dashed red curves). The closest match with the targeted phase relationship is the first case in which the airfoil oscillation lags the oscillating Mach number by $\Delta\varphi = -28.2°$. During the upstroke, as α approaches stall onset, the measured C_L is slightly higher than the steady $M = 0.4$ value. Again, in Section 3.1 it was shown that the lift curves collapsed for $M = 0.2$, 0.4, and 0.6 during the attached flow portion of the upstroke, so this is likely a freestream deceleration effect. The peak C_L is 15% higher than the steady $M = 0.4$ C_{Lmax}, and it occurs when $\alpha = 17.25°$, 0.75° higher than steady $M = 0.4$. The lift

stall characteristic is steepened. Post-stall C_L and the reattachment during the downstroke are virtually the same as the steady $M = 0.4$ case. Moment stall is similarly delayed by $\Delta\alpha = 0.75°$ relative to the steady $M = 0.4$ case, but the rest of the cycle seems to be unaltered.

The second case presented in this figure is for α leading Mach number by $\Delta\varphi = +46.4°$. This phase shift is approximately 80° from the first coupled case discussed above, but freestream deceleration is still underway during the airfoil upstroke. Moreover, the maximum deceleration magnitude, which occurs as Mach number crosses its mean value, coincides with the onset of dynamic stall at $\alpha = 16.5°$. In the first case ($\Delta\varphi = -28.2°$), the onset of stall occurs when the Mach number is close to the minimum and the acceleration parameter is approaching zero before changing sign. Therefore, comparing these two specific cases provides insight into the roles of compressibility and acceleration with respect modifying the dynamic stall process. As α approaches stall onset during the upstroke, a slightly higher C_L is measured in both cases with respect to the steady $M = 0.4$ data. However, the higher peak C_L is observed for the first case where the minimum Mach number coincides with the onset of stall. The lift-curve slope changes sign for both cases at approximately $\alpha \approx 17°$. The slope of the lift stall characteristic for the second case is shallower for the first, and the post-stall C_L for $19° < \alpha < 20°$ at the end of the upstroke is higher by approximately 0.1. Otherwise for the remainder of the pitch oscillation, the difference in C_L between either case and the steady $M = 0.4$ case is negligible. As with $k = 0.0125$, all C_M orbits register equal peak negative moments. For $k = 0.0250$, the peak negative $C_M \approx -0.16$, and for these first two cases, the slope of the moment stall characteristic is approximately the same as the steady $M = 0.4$ case. Moment stall for the second case ($\Delta\varphi = +46.4$) occurs at the same phase and $\alpha = 16.5°$ as for the steady $M = 0.4$ case, while it is delayed by $\Delta\alpha \approx 0.75°$ for the first case ($\Delta\varphi = -28.2°$).

Phase-averaged upper surface C_p contours are presented for the $k = 0.025$ cases in Figure 41. The steady $M = 0.4$ data is presented on the far left with coupled oscillation cases in order of increasing $\Delta\varphi$ positioned from left to right. The first two coupled oscillation cases indicate enhanced suction developing near the leading edge and culminating with a stronger LEV signature relative to the steady $M = 0.4$ LEV. Suction is sustained until higher α for $\Delta\varphi = -28.2°$ thereby delaying moment stall and the strength of the LEV appears to decay more slowly as it convects downstream in this case.

The third case representing coupled oscillations at $k = 0.0250$ is for α leading oscillating Mach number by $\Delta\varphi = +145.4°$. Like the third case for $k = 0.125$ ($\Delta\varphi = +127.3$), the freestream is accelerating during the upstroke, decelerating during the downstroke so that α peaks when M is nearly maximum. The hysteresis is diminished for this phasing. The area enclosed by the C_L and C_M orbits reduced. The difference in C_{Lmax} between upstroke and downstroke decreases from upwards of 0.6 for the first two cases to 0.3 for this third case. The lift stall process initiates at $\alpha \approx 15°$ where the lift curve departs from the first two cases. The stall characteristic indicates stall which develops more gradually, and the post-stall C_L during the downstroke is higher than the first two cases and the steady $M = 0.4$ data. Moment stall occurs 0.75° before the steady $M = 0.4$ case and the slope of the moment stall characteristic is shallower. The first two cases and the steady $M = 0.4$ cases all have a spike with peak nose down $C_M = -0.17$ at $\alpha \approx 18°$. The spike occurs while the LEV convects between the quarter-chord and the trailing edge. Once the LEV convects past the trailing edge, the moment coefficient increases to $C_M = -0.15$ by the phase where $\alpha = 20°$ as the airfoil completes the upstroke. Whereas the other cases all exhibit the C_M spike, the third case ($\Delta\varphi = +145.4°$) does not. The moment coefficient decreases to $C_M = -0.14$ without the higher frequency fluctuations that accompany the LEV convection sequence. The reattachment process is similar for all four cases.

The comparison between C_p contours for $\Delta\varphi = +145.4°$ and the three other data points in Figure 41 is very similar in nature to that for $k = 0.0125$ (Figure 39). Suction development is limited near the leading edge, and the LEV signature is indiscernible. Furthermore the C_p levels are slightly lower during the stalled interval relative to the other three cases.
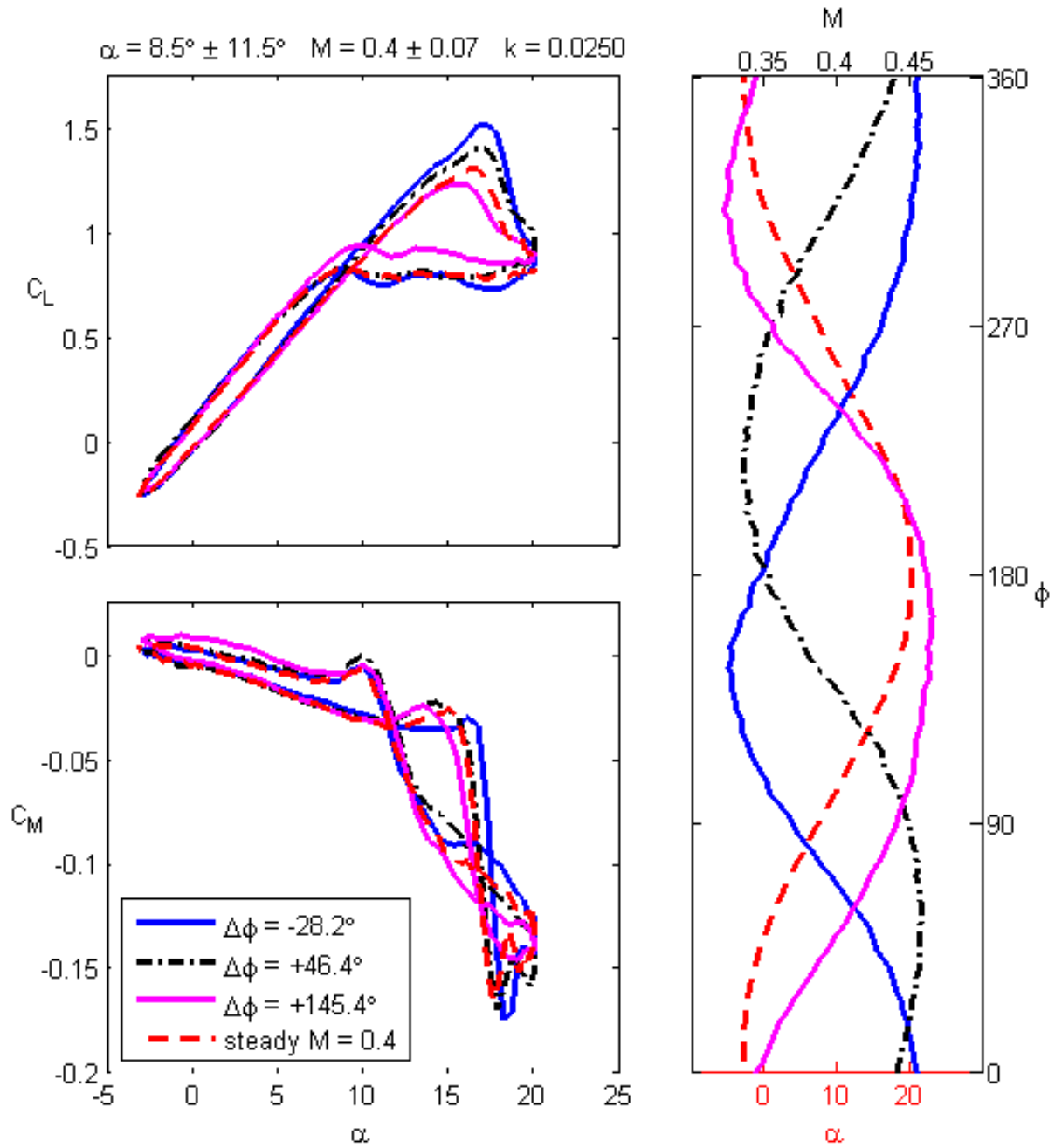
Figure 40: C_L and C_M orbits for $\alpha = 8.5° \pm 11.5°$, $M = 0.4 \pm 0.07$, $k = 0.0250$, and representative phasing between synchronous oscillations.
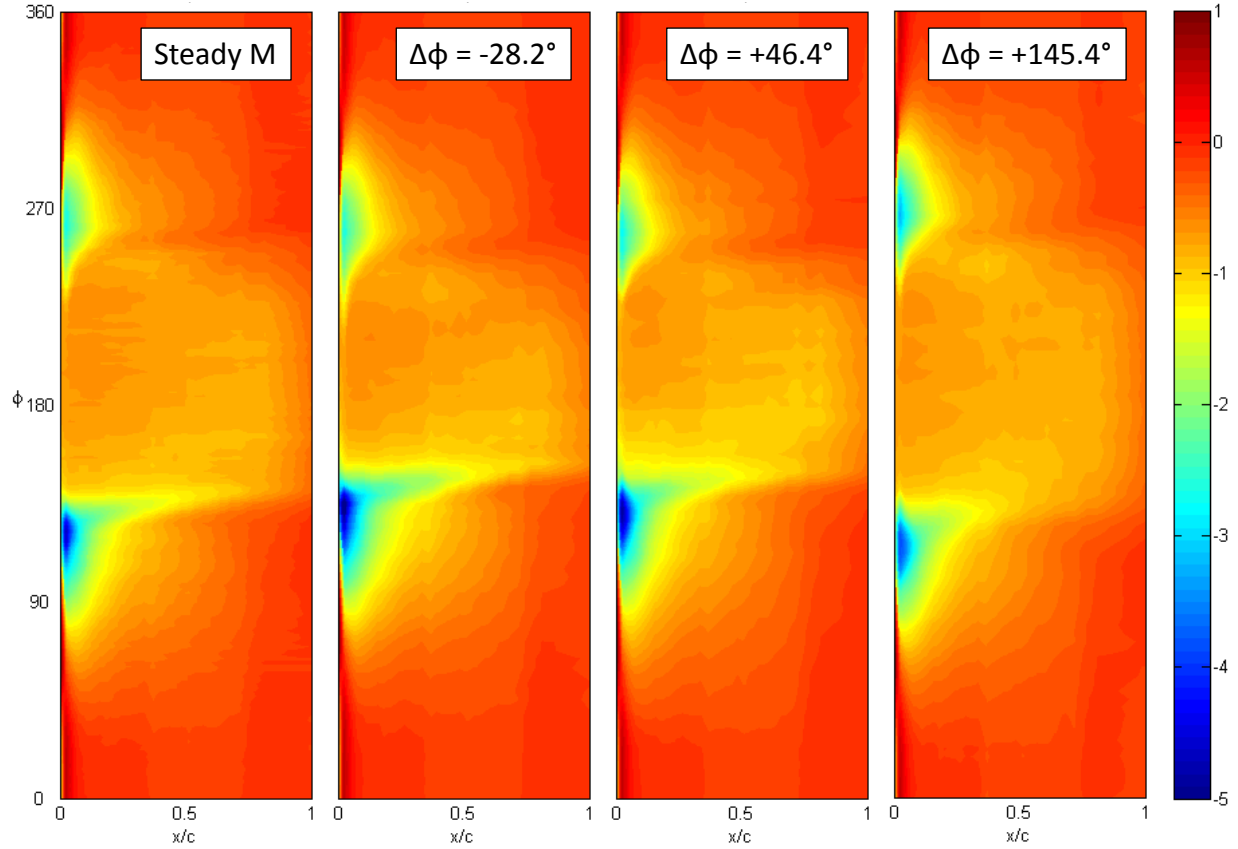
Figure 41: C_p contours for $\alpha = 8.5° \pm 11.5°$, $M = 0.4 \pm 0.07$, $k = 0.0250$, and representative phasing between synchronous oscillations.

Figure 42 represents phase-averaged upper surface C_p data recorded by 16 taps near the leading edge for chordwise positions spanning $0.023 \leq x/c \leq 0.335$. The figure consists of five plots stacked for ease of comparison. Phase angle is plotted along the abscissa. Phase-averaged Mach number is reproduced in the lowest plot for reference regarding the phasing ($\Delta\varphi$) in each case. Pressure coefficient data are presented for each of the $k = 0.0250$ cases (one $\Delta\varphi$ case in each of the upper three C_p plots) and for the steady $M = 0.4$ case (lower C_p plot). No artificial offset is used to add space between curves of consecutive taps for clarity because the levels are compared with the phase-averaged critical pressure coefficient to ascertain the extent of supercritical flow. Finally, it should be noted that the upstream-most tap always registers the lowest C_p for $90° < \varphi < 315°$, and the peak suction indicated by each tap decreases marching in the downstream direction. Attention is called to the development of suction with respect to $C_{p,cr}$ and onset of stall occurring for $45° < \varphi < 150°$. Two upper surface taps measure supercritical pressures for $108° < \varphi < 135°$ just before all of the pressures increase to $C_p = -1$ by $\varphi = 135°$ in the steady $M = 0.4$ case. For $\Delta\varphi = -28.2°$, Mach number is approaching the minimum value as α

increases. Thus, $C_{p,cr}$ simultaneously approaches the peak values for the cycle ($C_{p,cr} \approx -5.9$). A supercritical condition does not occur for this phasing. Greater suction is developed near the leading edge until $\varphi = 135°$. The pressure rise which indicates stall starts with the upstream-most tap and proceeds from the leading edge and transpires most abruptly for the $\Delta\varphi = -28.2°$ case. The phasing alignment in the second case ($\Delta\varphi = +46.4°$) is such that $C_{p,cr} = -3.55$ when stall begins. This critical pressure is approximately equal to that of the steady $M = 0.4$ case. Recall that the $\Delta\varphi = +46.4°$ and steady $M = 0.4$ data exhibited moment stall at the exact same phase in the pitch oscillation cycle. Three upper surface taps recorded supercritical pressures in the second coupled-oscillation case ($\Delta\varphi = +46.4°$) and the ensuing stall was relatively gradual. In the final coupled oscillation case, for $\Delta\varphi = +145.4°$, the chordwise extent of the supercritical region spans four taps as the freestream Mach number peaks ($C_{p,cr} = -2.7$) and the airfoil stalls. Comparing the rate of the pressure rise between all four cases it is evident that as the extent of the supercritical flow on the airfoil increases, the stall process becomes increasingly gradual in nature.

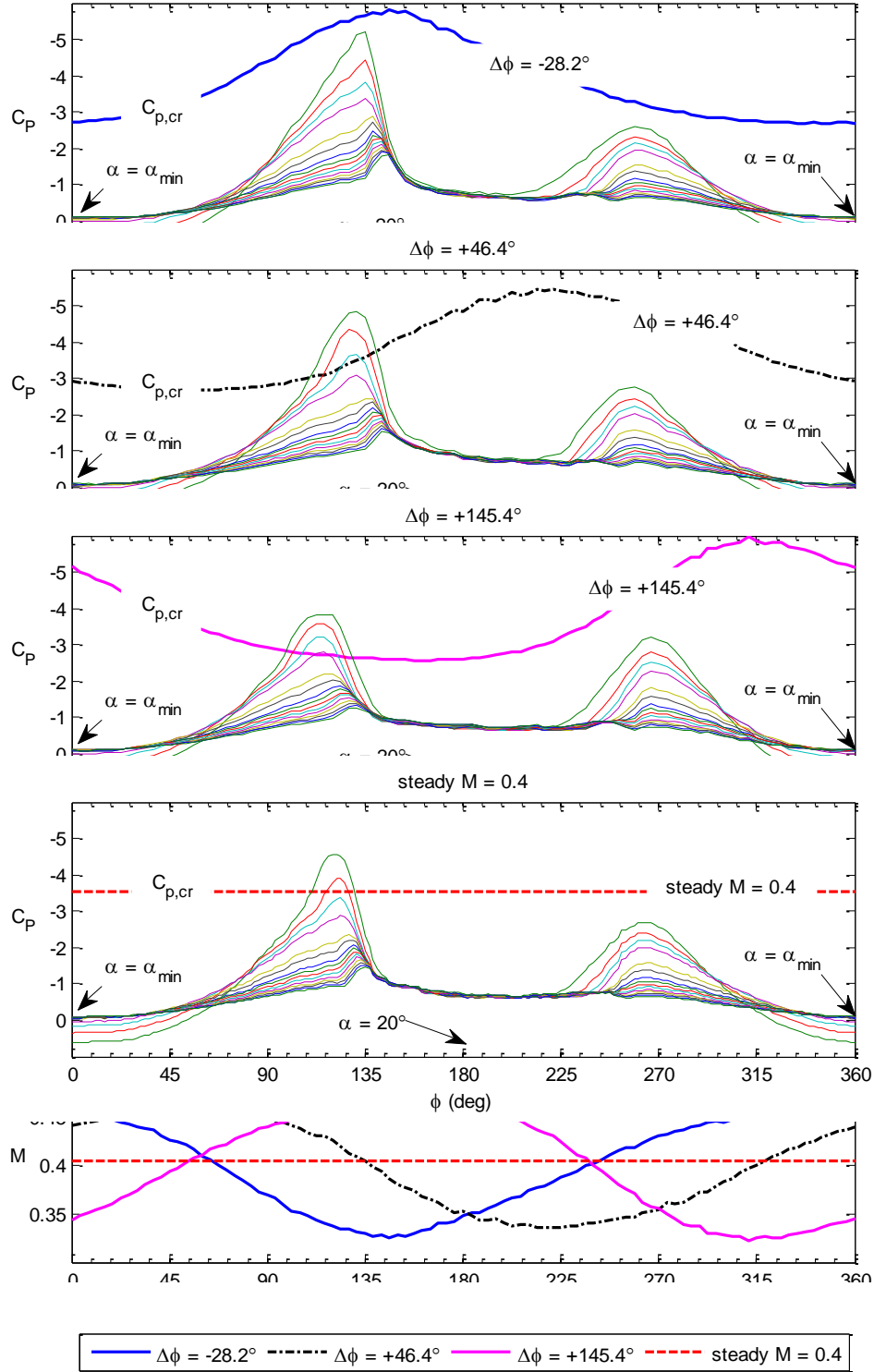**Figure 42: Comparing phase-averaged upper surface (leading edge) C_p with $C_{p,cr}$ for coupled-oscillation and steady $M = 0.4$ cases and $k = 0.0250$.**

Only two cases are presented in Figure 43 (C_L and C_M) and Figure 44 (C_p contours) for $k = 0.0500$. The phasing of the coupled-oscillation cases is a close match to the target with α leading

M by $\Delta\varphi$ = +13.3°. This case is compared with that of the airfoil executing an identical pitch oscillation profile in a steady *M* = 0.4 airstream. Apart from the interval for 90° < φ < 180°, the impact of time-varying compressibility on C_L and C_M hysteresis is marginal. The post-stall and reattachment process during the downstroke are unaltered even for this highest reduced frequency. For 90° < φ < 180°, α is increasing from 7.5° to 22°. The lift coefficient and lift curve slope are higher in the coupled-oscillation case throughout this interval. The difference in C_L between the two cases (ΔC_L) increases until both cases reach C_{Lmax} at α = 18.5° with a maximum ΔC_L = 0.3. The slope of the lift stall characteristic is approximately equal in both cases indicating that the stall type is unchanged. Based on the C_L hysteresis behavior, the manner in which the dynamic stall process is modified by time-varying compressibility is similar for all three reduced frequencies for which the phasing is similar to that presented in Figure 37. However, for *k* = 0.0125 and 0.0250, coupled-oscillations with this type of phasing ($\Delta\varphi \approx 0°$) did not produce a marked differences in the C_M hysteresis. The peak negative C_M increases by 20% for the *k* = 0.0500 cases with respect to the steady *M* = 0.4 result.

Figure 44 juxtaposes the upper surface C_p contours for the two *k* = 0.0500 cases. Suction development preceding the LEV formation is enhanced for the coupled-oscillation case. The peak is C_p = –5.15 at φ = 139° and α = 17° for the coupled oscillation case, while the peak is C_p = –4 at φ = 128° and α = 15° for the steady *M* = 0.4 case. As with cases of similar phasing for *k* = 0.0125 and 0.0250, the magnitude of the C_p depression created by the LEV signature is amplified. Observing how the LEV signature is modified for cases of similar $\Delta\varphi$, it seems that the LEV amplification relative to the steady *M* = 0.4 cases is proportional to the reduced frequency. Along with the exaggerated low pressure signal, the chordwise extent of the LEV signature relative to the steady *M* = 0.4 data indicates a stronger LEV as it convects along the upper surface. These plots do not necessarily speak to the rate at which the LEV strength decays, but the LEV is certainly stronger as it travels downstream past the quarter chord, thereby exacerbating the peak negative pitching moment as shown in Figure 43.
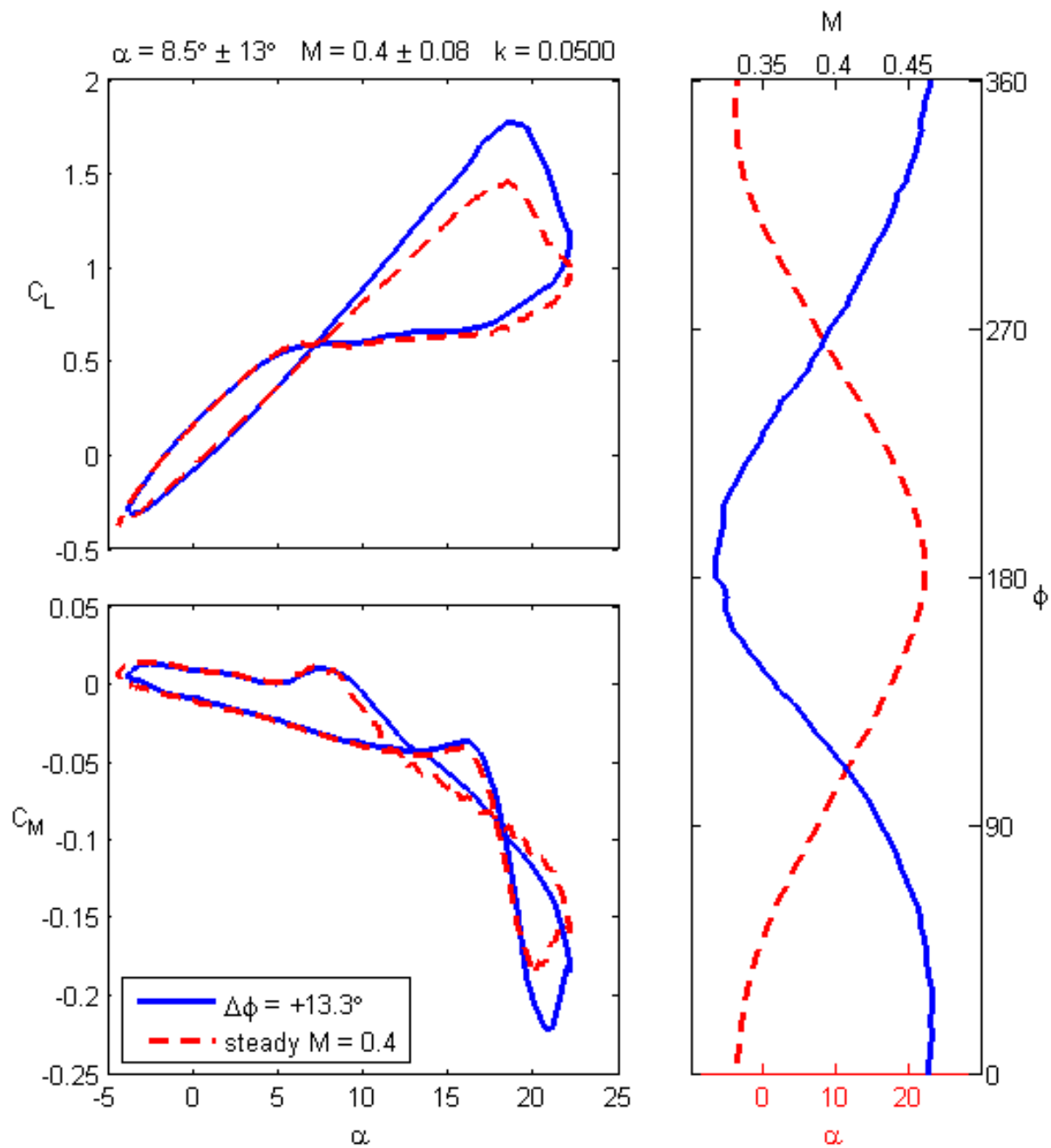
Figure 43: C_L and C_M orbits for $\alpha = 8.5° \pm 13°$, $M = 0.4 \pm 0.08$, $k = 0.0500$, and representative phasing between synchronous oscillations.
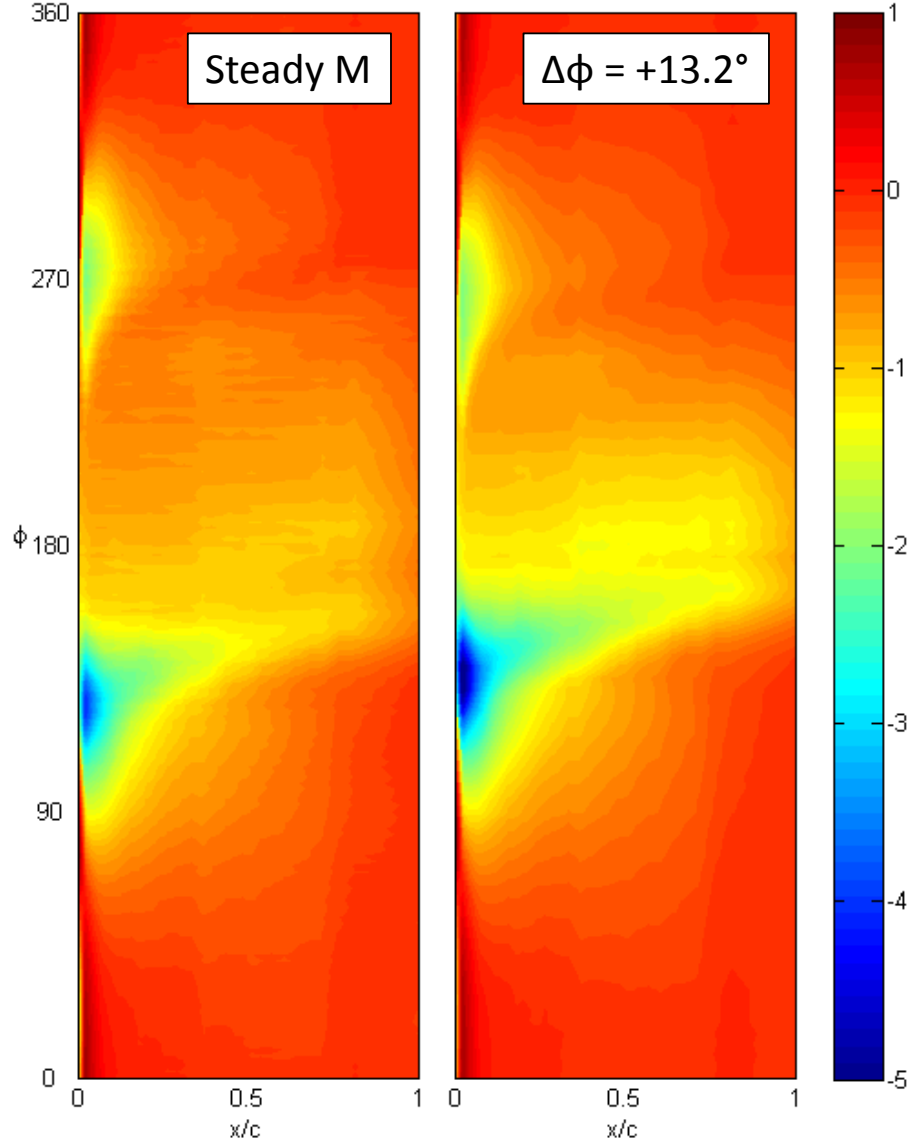
Figure 44: C_p **contours for** $\alpha = 8.5° \pm 13°$**,** $M = 0.4 \pm 0.08$**,** $k = 0.0500$**, and representative phasing between synchronous oscillations.**

The results presented for these three reduced frequencies suggests that compressibility has a first-order effect on the peak C_L and the onset of dynamic stall, while the acceleration parameter plays a secondary role which can produce lift enhancement especially during the deceleration interval. When freestream deceleration coincides with the upstroke and the onset of dynamic stall, it precipitates a stronger dynamic stall process wherein greater suction develops on the upper surface, C_{Lmax} is greater, and the LEV strength is amplified along with the pitching moment spike. The hysteresis effects are exaggerated as reduced frequency increases.

4. Conclusion

An advanced dynamic stall wind tunnel experiment was conducted in which the free stream velocity was made to oscillate at the same frequency as the airfoil pitch. Pressure contours, along with integrated lift and moment data, were presented for an airfoil subjected to various compressible dynamic stall conditions. The dynamic stall problem was segmented into three parts to facilitate understanding: pitch oscillations in a fixed compressible freestream, Mach oscillations with fixed angle of attack, and coupled pitch and Mach oscillations.

As is commonly observed with steady compressibility effects, the max C_L in dynamic stall is lowered with increased freestream M. The C_M is less negative, but the dimensional moment magnitudes are obviously still much higher, and fluctuations are very significant. One critical aspect of compressibility effects is a change from leading-edge dominated dynamic stall, where the inception of the LEV coincides with the collapse of the suction peak, to trailing-edge dominated. Suction levels near the leading edge are sustained as the freestream Mach number increases whereas the suction peak completely collapses in the case of low freestream Mach number. The transformation in the stall process from leading-edge to trailing-edge type can inhibit the formation and strength of the LEV and result in lower peak negative moment magnitude.

For fixed alpha, oscillating Mach work, the steady-state stall angle of attack for the mean Mach number of the oscillations is a critical parameter. Both lift and moment tend to oscillate about their steady-state flow values and both are greater than steady-state while the freestream is decelerating and smaller while accelerating. Reduced frequency exacerbates this hysteresis. Higher-frequency periodic fluctuations appear when the static stall angle is reached (after abrupt loss of leading-edge suction peak).

The phase relationship between the freestream velocity and the airfoil angle of attack was varied and found to have significant effects on the aerodynamic loads. In particular:

1) In-phase oscillation of the airfoil pitch and the free stream velocity was found to cause increased lift curve slope and increased stall angle compared to an airfoil with oscillating pitch in steady flow. The increased stall angle is associated with a more sudden loss of lift.

2) Out-of-phase oscillation had the opposite effect, decreasing both the lift curve slope and the stall angle. This was associated with a more gradual stall event and loss of lift.

3) The magnitude of peak negative moment coefficient was found to be stronger for in-phase motion than for out-of-phase motion, as the leading edge vortex convects further along the upper surface of the model.

4) The time history of the moment coefficient differs mainly quantitatively between phase angles, but retains the same qualitative shape; this contrasts with visible qualitative changes to moment orbits at different static Mach numbers.

Compressibility has a first-order effect on the peak C_L and the onset of dynamic stall, while the acceleration parameter plays a secondary role which can produce lift enhancement especially during the deceleration interval. When freestream deceleration coincides with the upstroke and the onset of dynamic stall, it precipitates a stronger dynamic stall process wherein greater suction develops on the upper surface, C_{Lmax} is greater, and the LEV strength is amplified along with the pitching moment spike. The hysteresis effects are exaggerated as reduced frequency increases.

Oscillation of freestream velocity is a fundamental aspect of the operating environment of the lifting surfaces of a rotorcraft, and its absence in wind tunnel studies was shown to result in changes in the measured performance of the test article. Accurately simulating oscillations of pitch and freestream velocity in the airfoil environment is necessary to fully reproduce the aerodynamic loads experienced by a rotor in forward flight.

5. Acknowledgements

6. References

Babinsky, H. and Fernie, R. M., (2002) "NACA0012 Aerofoil in an oscillating freestream," AIAA 2002-0115, 40th AIAA Aerospace Sciences Meeting and Exhibit, American Institute of Aeronautics and Astronautics, Reno, NV.

Bergh, H., and Tijdeman, H., 1965, "Theoretical and Experimental Results for the Dynamic Resoponse of Pressure Measuring Systems," Tech. rep., Tech. Rep. TR F.238, Amsterdam

Nationaal Luchtvaarlaboratorium (National Aeronautical and Astronautical Research Institute), Jan. 1965.

Bousman, W. G., (1998) "A Qualitative Examination of Dynamic Stall from Flight Test Data," *Journal of the American Helicopter Society*, Vol. 43, No. 4, pp. 279-295.

Bruce, P. J. K. and Babinsky, H., (2008) "Unsteady shock wave dynamics," *Journal of Fluid Mechanics*, v. 603, pp. 463-473.

Carr, L. W., (1988) "Progress in Analysis and Prediction of Dynamic Stall," *Journal of Aircraft*, Vol. 25, No. 1, pp. 6-17.

Carr, L. W. and Chandrasekhara, M. S., (1992) "Design and Development of a Compressible Dynamic Stall Facility," *Journal of Aircraft*, Vol. 29, No. 3, pp. 314-318.

Carr, L. W. and Chandrasekhara, M. S., (1996) "Compressibility Effects on Dynamic Stall," *Progress in Aerospace Sciences*, Vol. 32, pp. 523-573.

Carr, L. W., Chandrasekhara, M. S., and Brock, N. J., (1994) "Quantitative Study of Unsteady Compressible Flow on an Oscillating Airfoil," *Journal of Aircraft*, Vol. 31, No. 4, pp. 892-898.

Carr, L. W., Chandrasekhara, M. S., Wilder, M. C., and Noonan, K. W., (2001) "Effect of Compressibility on Suppression of Dynamic Stall Using a Slotted Airfoil," *Journal of Aircraft*, Vol. 38, No. 2, pp. 296-309.

Chandrasekhara, M. S., (2007) "Compressible dynamic stall vorticity flux control using a dynamic camber airfoil," *Sādhanā*, Vol. 32, No. 1-2, February–April 2007, pp. 93–102.

Chandrasekhara, M. S. and Carr, L. W., (1990) "Flow Visualization Studies of the Mach Number Effects on Dynamic Stall of an Oscillating Airfoil," *Journal of Aircraft*, Vol. 27, No. 6, pp. 516-522.

Chandrasekhara, M. S. and Wilder, M. C., (2003) "Heat-Flux Gauge Studies of Compressible Dynamic Stall," *AIAA Journal*, Vol. 41, No. 5, pp. 757-762.

Chandrasekhara, M. S., Wilder, M. C., and Carr, L. W., (1998) "Competing Mechanisms of Compressible Dynamic Stall," *AIAA Journal*, Vol. 36, No. 3, pp. 387-393.

Chandrasekhara, M. S., Wilder, M. C., and Carr, L. W., (2001) "Compressible Dynamic Stall Control Using Dynamic Shape Adaptation," *AIAA Journal*, Vol. 39, No. 10, pp. 2021–2024.

Chandrasekhara, M. S., Martin, P. B., and Tung, C., (2004) "Compressible Dynamic Stall Control Using a Variable Droop Leading Edge Airfoil," *AIAA Journal*, Vol. 41, No. 4, pp. 862-869.

Coleman, H.W., and Steele, W.G., 1999, *Experimentation and Uncertainty Analysis for Engineers*, 2nd ed., Wiley-Interscience, New York.

DiOttavio, J., Watson, K., Cormey, J., and Komerath, N., (2008) "Discrete Structures in the Radial Flow Over a Rotor Blade in Dynamic Stall," AIAA 2008-7344, 26th AIAA Applied Aerodynamics Conference, American Institute of Aeronautics and Astronautics, Honolulu, HI.

Ericsson, L. E., (1985) "Is Any Free Flight/Wind Tunnel Equivalence Concept Valid for Unsteady Viscous Flow?," *Journal of Aircraft*, Vol. 22, No. 10, pp. 915-919.

Ericsson, L. E., (1994) "Problem of Dynamic Stall Simulation Revisited," *Journal of Aircraft*, Vol. 31, No. 4, pp. 782-786.

Ericsson, L. E. and Reding, J. P., (1971) "Dynamic Stall Simulation Problems," *Journal of Aircraft*, Vol. 8, No. 7, pp. 579-583.

Ericsson, L. E. and Reding, J. P., (1984) "Shock-Induced Dynamic Stall," *Journal of Aircraft*, Vol. 21, No. 5, pp. 316-321.

Favier, D., Agnes, A., Barbi, C., and Maresca, C., (1988) "Combined Translation/Pitch Motion: A New Airfoil Dynamic Stall Simulation," *Journal of Aircraft*, Vol. 25, No. 9, pp. 805-814.

Favier, D., Maresca, C., and Rebont, J., (1982) "Dynamic Stall Due to Fluctuations of Velocity and Incidence," *AIAA Journal*, Vol. 20, No. 7, pp. 865-871.

Favier, D., Rebont, J., and Maresca, C., (1979) "Large-Amplitude Fluctuations of Velocity and Incidence on an Oscillating Airfoil," *AIAA Journal*, Vol. 17, No. 11, pp. 1265-1267.

Fernie, R. M. (2004), *Low Frequency Shock Motion on a NACA 0012 Aerofoil*, Ph.D. Dissertation, Kings College, University of Cambridge, October 29, 2004.

Fernie, R. M. and Babinsky, H., (2003) "Unsteady Shock Behaviour on a NACA0012 Aerofoil," AIAA 2003-0226, 41st AIAA Aerospace Sciences Meeting and Exhibit, American Institute of Aeronautics and Astronautics, Reno, NV.

Fernie, R. M. and Babinsky, H., (2004) "Unsteady Shock Motion on a NACA0012 Aerofoil at Low Reduced Frequencies," AIAA 2004-0049, 42nd AIAA Aerospace Sciences Meeting and Exhibit, American Institute of Aeronautics and Astronautics, Reno, NV.

Geissler, W., Dietz, G., and Mai, H., (2005) "Dynamic stall on a supercritical airfoil," *Aerospace Science and Technology*, Vol. 9, pp. 390-399.

Goethert, B.H., 2007, *Transonic Wind Tunnel Testing*, Dover Publications.

Gompertz, K., Kumar, P., Jensen, C., Peng, D., Gregory, J., and Bons, J., 2011, "Modification of Transonic Blowdown Wind Tunnel to Produce Oscillating Freestream Mach Number," *AIAA Journal*, vol. 49, no. 11, pp. 2555-2563.

Gompertz, K., Jensen, C.D., Gregory, J.W., and Bons, J.P., 2012, "Compressible Dynamic Stall Mechanisms Due to Airfoil Pitching and Freestream Mach Oscillations," *Proceedings of the American Helicopter Society 68th Annual Forum*, Fort Worth, Texas, May 1-3, 2012.

Gregorek, G.M., Hoffman, M.J., and Berchak, M.J., 1989, "Steady State and Oscillatory Aerodynamic Characteristics of a NACA 0015 Airfoil," Data Report, Aeronautical and Astronautical Research Laboratory, Ohio State University, Columbus, Ohio.

Hird, K., Frankhouser, M., Gregory, J.W., and Bons, J.P., 2014, "Compressible Dynamic Stall of an SSC-A09 Airfoil Subjected to Coupled Pitch and Freestream Mach Oscillations," Paper No. 19, American Helicopter Society 70th Annual Forum, Montreal, Quebec, Canada, May 20-22, 2014.

Lee, J.D., Gregorek, G.M., and Korkan, K.D., 1978, "Testing Techniques and Interference Evaluation in the OSU Transonic Airfoil Facility," *Proceedings of the 11th Fluid and Plasma Dynamics Conference*, AIAA 78-1118, AIAA, Seattle, WA.

Lorber, P.F. and Carta, F.O., 1987, "Unsteady Stall Penetration Experiments at High Reynolds Number," Technical Report, AFOSR-TR-87-1202, DoD Accession Number AD-A186120.

Lorber, P.F., Carta, F.O., and Covino, Jr., A.F., 1992, "An Oscillating Three-Dimensional Wing Experiment: Compressibility, Sweep, Rate, Waveform, and Geometry Effects on Unsteady Separation and Dynamic Stall," UTRC Report R92-958325-6, DoD Accession Number AD-A260530.

Maresca, C., Favier, D., and Rebont, J., (1981) "Unsteady Aerodynamics of An Aerofoil At High Angle Of Incidence Performing Various Linear Oscillations In A Uniform Stream," *Journal of the American Helicopter Society*, Vol. 26, No. 2, pp. 40-45.

Martin, P. B., McAlister, K. W., Chandrasekhara, M. S., and Geissler, W., (2003) "Dynamic Stall Measurements and Computations for a VR-12 Airfoil with a Variable Droop Leading Edge," *Proceedings of the American Helicopter Society 59th Annual Forum*, Phoenix, Arizona, May 6 – 8, 2003.

McCroskey, W. J., Carr, L. W., and McAlister, K. W., (1976) "Dynamic Stall Experiments on Oscillating Airfoils," *AIAA Journal*, Vol. 14, No. 1, pp. 57-63.

McCroskey, W. J., (1987) "A Critical Assessment of Wind Tunnel Results for the NACA 0012 Airfoil," NASA Technical Memorandum 100019, USAAVSCOM Technical Report 87-A-5, October 1987.

Petrie, S.L. and Davis, J.A., 1978, "Unsteady Transonic Aerodynamics," Symposium on Airfoils and Aviation, Proceedings of the Annual Conference for Engineers.

Pierce, G. A., Kunz, D. L., and Malone, J. B., (1978) "The Effect of Varying Freestream Velocity on Airfoil Dynamic Stall Characteristics," *Journal of the American Helicopter Society*, Vol. 23, No. 2, pp. 27-33.

Piziali, R. A., (1994) "2-D and 3-D Oscillating Wing Aerodynamics for a Range of Angles of Attack Including Stall," National Aeronautics and Space Administration, Ames Research Center, NASA TM-4632 / USAATCOM Technical Report 94-A-011, Moffett Field, CA.

Retelle, J. P., Jr., McMichael, J. M., and Kennedy, D. A., (1981) "Harmonic Optimization of a Periodic Flow Wind Tunnel," *Journal of Aircraft*, Vol. 18, No. 8, pp. 618-623.

Sahoo, D., Bowersox, R. D. W., and Goss, L., (2008) "Experimental Investigation of the Leading-Edge Flow of a Dynamically Pitching Airfoil," AIAA 2008-0651, 46th Aerospace Sciences Meeting and Exhibit, American Institute of Aeronautics and Astronautics, Reno, NV.

Selerowicz, W. C. and Szumowski, A. P., (2002) "Airfoil flow instabilities induced by background flow oscillations," *Experiments in Fluids*, v. 32, pp. 441-446, DOI: 10.1007/s00348-001-0377-4.

Szumowski, A. P. and Meier, G. E. A., (1996) "Forced oscillations of airfoil flows," *Experiments in Fluids*, v. 21, pp. 457-464.

Appendix 1: Airfoil Coordinates

Surface Coordinates			Surface Derivatives		
	Upper	Lower		Upper	Lower
x/c	*y/c*	*y/c*	*x/c*	*dy/dx*	*dy/dx*
0.00000	0.00000	0.00000	0.00000	0.00000	0.00000
0.00020	0.00200	-0.00145	0.00010	10.05190	-7.30450
0.00080	0.00395	-0.00287	0.00050	3.24740	-2.36310
0.00199	0.00648	-0.00457	0.00140	2.12040	-1.42420
0.00299	0.00803	-0.00545	0.00249	1.55160	-0.87640
0.00449	0.00987	-0.00645	0.00374	1.23030	-0.66740
0.00698	0.01239	-0.00770	0.00573	1.01220	-0.50470
0.00997	0.01492	-0.00888	0.00848	0.84550	-0.39280
0.01595	0.01908	-0.01070	0.01296	0.69460	-0.30540
0.02193	0.02250	-0.01218	0.01894	0.57240	-0.24580
0.02792	0.02545	-0.01345	0.02493	0.49240	-0.21260
0.03390	0.02804	-0.01459	0.03091	0.43370	-0.19070
0.03988	0.03037	-0.01563	0.03689	0.38940	-0.17440
0.04586	0.03249	-0.01659	0.04287	0.35520	-0.16100
0.05185	0.03445	-0.01749	0.04885	0.32680	-0.14930
0.05783	0.03625	-0.01831	0.05484	0.30090	-0.13840
0.06780	0.03890	-0.01957	0.06281	0.26620	-0.12580
0.07777	0.04114	-0.02069	0.07278	0.22470	-0.11260
0.08774	0.04302	-0.02171	0.08275	0.18790	-0.10180
0.09771	0.04458	-0.02264	0.09272	0.15720	-0.09350
0.11266	0.04650	-0.02391	0.10519	0.12850	-0.08510
0.12762	0.04805	-0.02506	0.12014	0.10360	-0.07710
0.14257	0.04935	-0.02612	0.13510	0.08630	-0.07090
0.15753	0.05044	-0.02710	0.15005	0.07340	-0.06550
0.17249	0.05139	-0.02801	0.16501	0.06290	-0.06080
0.18744	0.05218	-0.02885	0.17996	0.05350	-0.05610
0.20240	0.05286	-0.02963	0.19492	0.04510	-0.05190
0.21735	0.05343	-0.03034	0.20987	0.03800	-0.04750
0.23231	0.05391	-0.03099	0.22483	0.03230	-0.04340
0.24726	0.05432	-0.03158	0.23978	0.02750	-0.03950
0.27717	0.05496	-0.03259	0.26222	0.02130	-0.03390
0.30708	0.05537	-0.03340	0.29213	0.01370	-0.02700
0.33699	0.05556	-0.03401	0.32204	0.00650	-0.02030
0.37687	0.05549	-0.03451	0.35693	-0.00180	-0.01250
0.41675	0.05504	-0.03464	0.39681	-0.01140	-0.00330

0.43669	0.05466	-0.03456	0.42672	-0.01890	0.00400
0.45664	0.05418	-0.03438	0.44667	-0.02410	0.00920
0.47658	0.05360	-0.03409	0.46661	-0.02940	0.01450
0.49652	0.05290	-0.03368	0.48655	-0.03490	0.02020
0.51646	0.05209	-0.03317	0.50649	-0.04040	0.02600
0.53640	0.05118	-0.03253	0.52643	-0.04600	0.03170
0.55634	0.05015	-0.03179	0.54637	-0.05150	0.03720
0.57628	0.04901	-0.03095	0.56631	-0.05720	0.04220
0.59622	0.04776	-0.03002	0.58625	-0.06290	0.04670
0.61616	0.04638	-0.02900	0.60619	-0.06890	0.05090
0.63610	0.04488	-0.02790	0.62613	-0.07550	0.05510
0.65604	0.04322	-0.02672	0.64607	-0.08300	0.05940
0.67598	0.04139	-0.02545	0.66601	-0.09170	0.06380
0.69592	0.03937	-0.02409	0.68595	-0.10150	0.06820
0.71586	0.03714	-0.02264	0.70589	-0.11170	0.07250
0.73580	0.03472	-0.02112	0.72583	-0.12140	0.07630
0.75574	0.03214	-0.01954	0.74577	-0.12940	0.07930
0.77568	0.02945	-0.01792	0.76571	-0.13510	0.08140
0.79562	0.02668	-0.01627	0.78565	-0.13860	0.08260
0.81556	0.02387	-0.01462	0.80559	-0.14090	0.08300
0.83550	0.02101	-0.01296	0.82553	-0.14340	0.08320
0.85544	0.01809	-0.01129	0.84547	-0.14660	0.08370
0.87538	0.01509	-0.00960	0.86541	-0.15020	0.08480
0.89532	0.01205	-0.00786	0.88535	-0.15250	0.08700
0.91526	0.00905	-0.00608	0.90529	-0.15070	0.08940
0.93520	0.00623	-0.00429	0.92523	-0.14130	0.08990
0.95514	0.00385	-0.00261	0.94517	-0.11930	0.08420
0.97508	0.00229	-0.00133	0.96511	-0.07830	0.06440
0.98506	0.00199	-0.00099	0.98007	-0.03020	0.03340
0.99503	0.00214	-0.00086	0.99004	0.01480	0.01300
1.00000	0.00241	-0.00080	0.99751	0.05480	0.01210

Appendix 2: Pressure Tap Locations

Tap No.	Upper Surface		
	x/c	*y/c*	*z/c*
1	0.000282	-0.00176	0.172067
2	0.022804	0.022955	0.164312
3	0.039563	0.03025	0.158541
4	0.056403	0.035838	0.152743
5	0.073554	0.040244	0.146837
6	0.109371	0.046116	0.134504
7	0.129914	0.048267	0.127431
8	0.159442	0.050573	0.117264
9	0.180233	0.051815	0.110105
10	0.201131	0.052807	0.102909
11	0.222392	0.053599	0.095588
12	0.24413	0.054243	0.088103
13	0.266187	0.054752	0.080508
14	0.288719	0.055143	0.07275
15	0.311568	0.05541	0.064882
16	0.334733	0.055562	0.056906
17	0.368783	0.055517	0.045182
18	0.391475	0.055387	0.037368
19	0.414166	0.055077	0.029555
20	0.436855	0.05466	0.021743
21	0.459541	0.054104	0.013931
22	0.482224	0.053409	0.006121
23	0.510572	0.052342	-0.00364
24	0.539698	0.051014	-0.01367
25	0.571175	0.049311	-0.02451
26	0.604995	0.047166	-0.03615
27	0.64115	0.044471	-0.0486
28	0.679622	0.041037	-0.06185
29	0.72038	0.036608	-0.07588
30	0.764967	0.030904	-0.09124
31	0.815746	0.023845	-0.10872

Tap No.	Lower Surface		
	x/c	y/c	z/c
1	0.000282	-0.00176	0.172067
32	0.037661	-0.01525	0.159196
33	0.054657	-0.01788	0.153344
34	0.071558	-0.02001	0.147524
35	0.088494	-0.02178	0.141693
36	0.10608	-0.02337	0.135637
37	0.124466	-0.02483	0.129307
38	0.156017	-0.02701	0.118443
39	0.18906	-0.02894	0.107065
40	0.223693	-0.03062	0.09514
41	0.259913	-0.03203	0.082669
42	0.297718	-0.03317	0.069651
43	0.338683	-0.03403	0.055546
44	0.373208	-0.03448	0.043658
45	0.406301	-0.03463	0.032263
46	0.439394	-0.03454	0.020868
47	0.474061	-0.03413	0.008932
48	0.514371	-0.03322	-0.00495
49	0.561622	-0.03158	-0.02122
50	0.61878	-0.02886	-0.0409
51	0.686976	-0.02471	-0.06438
52	0.743046	-0.02055	-0.08369
53	0.797305	-0.01613	-0.10237